



DETERMINATION OF BURIED CIRCULAR CYLINDER  
WITH  
GROUND PENETRATING RADAR  
USING  
AN OPTICAL FIBER SENSOR

A THESIS SUBMITTED TO  
THE GRADUATE SCHOOL OF NATURAL AND APPLIED SCIENCES  
OF  
MIDDLE EAST TECHNICAL UNIVERSITY

BY

HATİCE GONCA BULUR

IN PARTIAL FULFILLMENT OF THE REQUIREMENTS  
FOR  
THE DEGREE OF MASTER OF SCIENCE  
IN  
ELECTRICAL AND ELECTRONICS ENGINEERING

SEPTEMBER 2011

Approval of the thesis:

**DETERMINATION OF BURIED CIRCULAR CYLINDER WITH  
GROUND PENETRATING RADAR USING  
AN OPTICAL FIBER SENSOR**

submitted by **HATİCE GONCA BULUR** in partial fulfillment of the requirements  
for the degree of **Master of Science in Electrical and Electronics Engineering**  
**Department, Middle East Technical University** by,

Prof. Dr. Canan Özgen  
Dean, Graduate School of **Natural and Applied Sciences** \_\_\_\_\_

Prof. Dr. İsmet Erkmén  
Head of Department, **Electrical and Electronics Engineering** \_\_\_\_\_

Assist. Prof. Dr. Asaf Behzat Şahin  
Supervisor, **Electrical and Electronics Engineering Dept., METU** \_\_\_\_\_

**Examining Committee Members**

Prof. Dr. Yalçın Tanık  
Electrical and Electronics Engineering Dept., METU \_\_\_\_\_

Assist. Prof. Dr. Asaf Behzat Şahin  
Electrical and Electronics Engineering Dept., METU \_\_\_\_\_

Assoc. Prof. Dr. Çağatay Candan  
Electrical and Electronics Engineering Dept., METU \_\_\_\_\_

Assoc. Prof. Dr. Melek Diker Yücel  
Electrical and Electronics Engineering Dept., METU \_\_\_\_\_

Nurdan Vural Yüksel (M.Sc.)  
HC - ASELSAN \_\_\_\_\_

**Date:** **14.09.2011**

**I hereby declare that all information in this document has been obtained and presented in accordance with academic rules and ethical conduct. I also declare that, as required by these rules and conduct, I have fully cited and referenced all material and results that are not original to this work.**

Name, Last name : HATİCE GONCA BULUR

Signature :

# **ABSTRACT**

## **DETERMINATION OF BURIED CIRCULAR CYLINDER WITH GROUND PENETRATING RADAR USING AN OPTICAL FIBER SENSOR**

Bulur, Hatice Gonca

M.Sc., Department of Electrical and Electronics Engineering

Supervisor: Assist. Prof. Dr. Asaf Behzat Şahin

September 2011, 149 pages

The terms ‘ground-probing radar’, ‘ground penetrating radar (GPR)’, ‘sub-surface radar’ or ‘surface-penetrating radar (SPR)’ refer to various techniques for detecting and imaging of subsurface objects. Among those terms GPR is preferred and used more often.

In this thesis, the depth and the position of the buried circular cylinder are determined by a GPR system which comprises of an optical fiber sensor (OFS). The system is a combination of OFS, GPR and optical communication link. In order to determine the depth and the position, first of all the electric field distribution at the OFS is obtained by integrating the Green’s function over the induced current distribution. Those distributions are observed for different frequency and depth values. The voltages inside the distribution are measured by OFS. By changing the depth of the cylinder and the frequency of the system, various plots showing x axis displacement versus measured voltages are obtained. Those plots are related to interference fringe patterns. The position and the depth of the cylinder are obtained using interference fringe patterns.

All of the studies mentioned are performed in MATLAB R2007b program. The noises of the system due to OFS are extracted using OPTIWAVE OPTISYSTEM 7.0 program. By adding those noises to the measured voltage values, the operating frequency of the system is observed.

**Keywords:** Detection, Ground Penetrating Radar (GPR), Optical Fiber Sensor (OFS), Interference Fringe Pattern, Electric Field Distribution

# ÖZ

## FİBER OPTİK SENSÖR İÇEREN YERALTI RADARI İLE GÖMÜLÜ OLAN SİLİNDİRİK CİSMİN TESPİTİ

Bulur, Hatice Gonca

Yüksek Lisans, Elektrik ve Elektronik Mühendisliği Bölümü

Tez Yöneticisi: Yrd. Doç. Dr. Asaf Behzat Şahin

Eylül 2011, 149 sayfa

‘Yer yoklayan radar’, ‘yeraltı radarı (GPR)’, ‘yüzey altı radarı’ veya ‘yüzeye nüfuz eden radar’ terimleri yüzey altındaki cisimlerin belirlenmesi ve görüntülenmesi için çeşitli teknikleri ifade eder. Söz konusu terimlerden yeraltı radarları (GPR) tercih edilmekte ve daha çok kullanılmaktadır.

Bu tezde fiber optik sensör içeren GPR sistemi ile gömülü silindirik cismin konum ve derinlik tespiti yapılmıştır. Sistem GPR, fiber optik sensör ve optik haberleşme bağlantısının birleşiminden oluşmaktadır. Konum ve derinlik tespiti için ilk önce Green fonksiyonu kullanılarak sensördeki elektrik alan dağılımı bulunmuştur. Farklı frekans ve derinlik değerleri için çeşitli dağılımlar gözlemlenmiştir. Elektrik alan dağılımı içindeki voltajlar da fiber optik sensör ile ölçülmüştür. Cismin derinliği ve sistemin frekansı değiştirilerek; yatay uzaklığa bağlı ölçülen voltaj değerlerinin değişimine ait grafikler elde edilmiştir. Elde edilen bu grafiklerin her biri girişim modelleri ile ilişkilidir. Cismin derinliği ve konumu girişim modelleri kullanılarak tespit edilmiştir.

Bahsedilen çalışmalar MATLAB R2007b programı kullanılarak yapılmıştır. Sistemdeki sensörden kaynaklı gürültüler de OPTIWAVE OPTISYSTEM 7.0

programı ile çıkarılmıştır. Bu gürültüler, ölçtüğümüz voltaj değerlerine eklenerek sistemin çalışma frekansları belirlenmiştir.

Anahtar Kelimeler: Yeraltı Radarı (GPR), Fiber Optik Sensör, Girişim Modeli, Elektrik Alan Dağılımı

*To My Family*

## **ACKNOWLEDGEMENTS**

First of all, I would like to thank my supervisor, Assist. Prof. Dr. Asaf Behzat Şahin, for his guidance, advice, criticism, encouragement and insight throughout the study.

I would also like to express my deepest gratitude to my family for their support, love and encouragement throughout my life.

Thanks to the examining committee members Prof. Dr. Yalçın Tanık, Assoc. Prof. Dr. Çağatay Candan, Assoc. Prof. Dr. Melek Diker Yücel and Nurdan Vural Yüksel for evaluating my work and for their valuable comments.

# TABLE OF CONTENTS

|   |      |
|---|------|
| ABSTRACT.....   | iv   |
| ÖZ .....  | vi   |
| ACKNOWLEDGEMENTS .....  | ix   |
| TABLE OF CONTENTS.....  | x    |
| LIST OF TABLES .....  | xiii |
| LIST OF FIGURES .....   | xiv  |
| LIST OF ABBREVIATIONS .....   | xix  |
| CHAPTERS  |      |
| 1 INTRODUCTION .....  | 1    |
| 2 LITERATURE SURVEY .....   | 5    |
| 3 GENERAL REVIEW OF GROUND PENETRATING RADAR (GPR) .....                | 12   |
| 3.1 Introduction .....  | 12   |
| 3.2 Basic Principles .....  | 12   |
| 3.2.1 Operating Principle .....   | 12   |
| 3.2.2 Scattering of Electromagnetic (EM) Waves .....                    | 14   |
| 3.2.3 Electromagnetic (EM) Wave Propagation in Subsurface Material..... | 16   |
| 3.2.4 Physical Basis .....  | 16   |
| 3.2.4.1 Permittivity and Relative Permittivity .....                    | 17   |
| 3.2.4.2 Permeability and Relative Permeability .....                    | 18   |
| 3.2.4.3 Conductivity.....   | 18   |
| 3.3 Processing.....   | 20   |
| 3.3.1 Normal Processing .....   | 20   |
| 3.3.1.1 Monostatic Processing .....                                     | 20   |
| 3.3.1.2 Bistatic Processing .....                                       | 20   |
| 3.3.2 Advanced Processing .....   | 20   |
| 3.4 Display.....  | 21   |
| 3.5 Applications.....   | 22   |
| 3.6 Design.....   | 23   |
| 3.6.1 Center Frequency .....  | 23   |
| 3.6.2 Selection of the Antenna .....                                    | 24   |

|         |   |    |
|---------|---|----|
| 3.6.3   | Selecting Sampling Interval .....                                       | 25 |
| 3.6.4   | Operation Modes and Stacking .....                                      | 26 |
| 3.6.4.1 | Common Offset (CO) Mode .....   | 26 |
| 3.6.4.2 | Common Mid-point (CMP) Mode .....                                       | 27 |
| 3.6.4.3 | Transillumination Mode .....  | 28 |
| 3.6.5   | Wave Properties .....   | 29 |
| 3.6.6   | Resolution .....  | 30 |
| 3.6.6.1 | Lateral Resolution .....  | 30 |
| 3.6.6.2 | Range Resolution .....  | 32 |
| 3.6.7   | Propagation Velocity and Depth .....                                    | 33 |
| 3.6.8   | Selecting Antenna Separation .....                                      | 34 |
| 3.6.9   | Antenna Gain and Antenna Radiation Pattern .....                        | 35 |
| 3.6.10  | Clutter .....   | 37 |
| 3.6.11  | Losses .....  | 37 |
| 3.7     | Typical GPR Assumptions .....   | 38 |
| 3.8     | The Advantages and the Drawbacks of GPR .....                           | 39 |
| 4       | DETERMINATION OF THE SCATTERED ELECTRIC FIELDS .....                    | 40 |
| 4.1     | Introduction .....  | 40 |
| 4.2     | The Configuration .....   | 40 |
| 4.3     | The Scattered Electric Fields .....                                     | 43 |
| 4.3.1   | The Reflected Electric Field from the Dielectric Interface .....        | 43 |
| 4.3.2   | The Scattered Electric Field from the Buried Cylinder .....             | 43 |
| 4.3.3   | The Total Scattered Electric Field above the Dielectric Interface ..... | 48 |
| 5       | GENERAL REVIEW OF OPTICAL FIBER SENSOR (OFS) .....                      | 50 |
| 5.1     | Introduction .....  | 50 |
| 5.2     | Basic Information .....   | 51 |
| 5.3     | OFS Types .....   | 52 |
| 5.4     | Basic Components of an OFS Interrogation System .....                   | 53 |
| 5.4.1   | Optical Fibers .....  | 54 |
| 5.4.1.1 | Light Propagation in an Optical Fiber .....                             | 54 |
| 5.4.1.2 | Fiber Types .....   | 55 |
| 5.4.2   | Light Sources .....   | 58 |
| 5.4.2.1 | Semiconductor Sources of Light .....                                    | 58 |
| 5.4.2.2 | Laser Diode (LD) .....  | 59 |
| 5.4.3   | Optical Modulators .....  | 61 |
| 5.4.3.1 | Direct Optical Modulation .....   | 62 |
| 5.4.3.2 | External Optical Modulation .....                                       | 63 |
| 5.4.4   | Light Detectors .....   | 66 |
| 5.4.4.1 | Positive Intrinsic Negative (PIN) Photodiode .....                      | 67 |
| 5.4.4.2 | Avalanche Photodiode (APD) .....  | 68 |
| 5.5     | Fiber Materials .....   | 70 |
| 5.6     | Signal Degradation in Optical Fibers .....                              | 71 |
| 5.6.1   | Attenuation .....   | 71 |
| 5.6.2   | Distortion .....  | 72 |

|         |  |     |
|---------|--|-----|
| 5.6.2.1 | Intermodal Dispersion.....   | 72  |
| 5.6.2.2 | Intramodal Dispersion.....   | 73  |
| 5.7     | Applications.....  | 73  |
| 5.8     | The Advantages and the Drawbacks of Optical Fiber Sensors .....                      | 74  |
| 5.8.1   | The Advantages of Optical Fiber Sensors.....   | 74  |
| 5.8.2   | The Drawbacks of Optical Fiber Sensors.....  | 75  |
| 6       | IMPLEMENTATION OF GROUND PENETRATING RADAR (GPR) USING AN OPTICAL FIBER SENSOR ..... | 76  |
| 6.1     | Purpose and Problem Structure .....  | 76  |
| 6.2     | The Configuration of the GPR System.....   | 76  |
| 6.3     | Electric Field Strength at the OFS.....  | 79  |
| 6.4     | Analyses Performed in MATLAB .....   | 80  |
| 6.4.1   | Soil Model Used in the Study .....   | 80  |
| 6.4.1.1 | The Attenuation .....  | 81  |
| 6.4.1.2 | The Attenuation of Wet Soil.....   | 87  |
| 6.4.2   | MATLAB Analysis of Electric Field Distribution.....                                  | 89  |
| 6.4.2.1 | Simulation Results .....   | 90  |
| 6.4.3   | MATLAB Analysis of OFS .....   | 98  |
| 6.4.3.1 | Simulation Results .....   | 100 |
| 6.4.4   | Determining the Cylinder's Position.....   | 108 |
| 6.4.5   | Determining the Cylinder's Depth .....   | 110 |
| 6.4.5.1 | Simulation Results .....   | 112 |
| 6.5     | Accounting for Noise in the System.....  | 119 |
| 6.5.1   | Extracting Noise of the System from OPTIWAVE .....                                   | 119 |
| 6.5.1.1 | Determining Noise of the System without Filtering.....                               | 121 |
| 6.5.1.2 | Determining Noise of the System with Filtering .....                                 | 122 |
| 6.5.2   | Adding Noise to the System in MATLAB.....  | 126 |
| 6.5.2.1 | Simulation Results .....   | 126 |
| 7       | CONCLUSIONS AND FUTURE WORK .....  | 133 |
|         | REFERENCES.....  | 138 |
|         | APPENDICES   |     |
|         | A. MATLAB CODE .....   | 143 |
|         | B. OPTIWAVE SCREEN CAPTURE.....  | 149 |

## LIST OF TABLES

### TABLES

|   |     |
|---|-----|
| Table 3.1 The applications of GPR [24] .....  | 22  |
| Table 5.1 Some important properties of APDs and PIN photodiodes [37].....                               | 70  |
| Table 6.1 The noise values of APD for different frequency values.....                                   | 124 |
| Table 6.2 The modified noise and the receiver sensitivity values of APD for different frequencies ..... | 125 |
| Table 6.3 The SNR values for $f = 200$ MHz and $f = 1$ GHz .....  | 130 |

# LIST OF FIGURES

## FIGURES

|  |    |
|--|----|
| Figure 1.1 The block diagram of a typical GPR system [1].....  | 2  |
| Figure 1.2 The configuration of the GPR system that is used in the study where PD stands for photodetector .....                                     | 3  |
| Figure 3.1 Scattering types: a) spectral reflection scattering, b) refraction scattering, c) diffraction scattering and d) resonant scattering ..... | 15 |
| Figure 3.2 The working principle of GPR in CO mode.....  | 27 |
| Figure 3.3 The working principle of GPR in CMP mode .....  | 28 |
| Figure 3.4 The working principle of GPR in transillumination mode .....  | 29 |
| Figure 3.5 The types of GPR resolution: lateral and range resolution.....  | 31 |
| Figure 3.6 Range resolution versus relative permittivity for different bandwidths [17] .....   | 32 |
| Figure 3.7 The illustration of cross-coupling, clutter and reflected wave from the buried object.....  | 35 |
| Figure 4.1 The configuration of the scattering problem .....   | 41 |
| Figure 4.2 The geometry of the total scattered electric field above the dielectric interface.....  | 42 |
| Figure 4.3 The ray diagram of the scattered electric fields from cylinder for above the interface.....   | 48 |
| Figure 5.1 The basic optical communication system block diagram.....   | 51 |
| Figure 5.2 The OFS interrogation system block diagram .....  | 52 |
| Figure 5.3 The propagation of light in an optical fiber and the principle of the optical fiber .....   | 54 |
| Figure 5.4 The geometrical structure of an optical fiber.....  | 54 |

|   |    |
|---|----|
| Figure 5.5 The propagation of light in different types of fibers.....   | 57 |
| Figure 5.6 Schematics of an LED where arrows show spontaneous emission in all directions .....  | 59 |
| Figure 5.7 Schematics of an LD where arrow shows stimulated emission in one direction.....  | 60 |
| Figure 5.8 The configuration of MZ modulator.....   | 64 |
| Figure 5.9 The operation of MZ modulator .....  | 65 |
| Figure 5.10 The operation of the EA modulator .....   | 66 |
| Figure 5.11 The structure of a PIN photodiode.....  | 67 |
| Figure 5.12 The structure of an APD .....   | 68 |
| Figure 6.1 The configuration of the buried circular cylinder.....   | 77 |
| Figure 6.2 The configuration of the GPR system where PD stands for photodetector .....  | 78 |
| Figure 6.3 The configuration of the OFS .....   | 79 |
| Figure 6.4 The graph shows depth versus attenuation of martian soil at $f = 100$ MHz .....  | 83 |
| Figure 6.5 The graph shows frequency versus attenuation of martian soil at a fixed depth of $b = 20$ cm .....   | 83 |
| Figure 6.6 a) The graph shows frequency versus real part of index of refraction of martian soil at a fixed depth of $b = 20$ cm b) The graph shows frequency versus imaginary part of index of refraction of martian soil at a fixed depth of $b = 20$ cm.. | 85 |
| Figure 6.7 a) The graph shows frequency versus real part of permittivity of martian soil at a fixed depth of $b = 20$ cm b) The graph shows frequency versus imaginary part of permittivity of martian soil at a fixed depth of $b = 20$ cm.....            | 86 |
| Figure 6.8 The graph shows depth versus attenuation of wet soil at $f = 100$ MHz ...  | 88 |
| Figure 6.9 The graph shows frequency versus attenuation of wet soil at a fixed depth of $b = 20$ cm .....   | 88 |
| Figure 6.10 The 2D plot of electric field distribution variation due to vertical displacement versus height values for $f = 1$ GHz and $b = 10$ cm.....   | 90 |

|   |     |
|---|-----|
| Figure 6.11 The 2D plot of electric field distribution variation due to vertical displacement versus height values for $f = 1$ GHz and $b = 50$ cm .....  | 91  |
| Figure 6.12 The 2D plot of electric field distribution variation due to vertical displacement versus height values for $f = 1$ GHz and $b = 100$ cm .....   | 91  |
| Figure 6.13 The 3D plot of vertical displacement versus height versus total electric field for $f = 1$ GHz and $b = 10$ cm .....  | 92  |
| Figure 6.14 The 3D plot of vertical displacement versus height versus total electric field for $f = 1$ GHz and $b = 50$ cm .....  | 92  |
| Figure 6.15 The 3D plot of vertical displacement versus height versus total electric field for $f = 1$ GHz and $b = 100$ cm .....   | 93  |
| Figure 6.16 The 2D plot of electric field distribution variation due to vertical displacement versus height values for $b = 20$ cm and $f = 500$ MHz .....  | 94  |
| Figure 6.17 The 2D plot of electric field distribution variation due to vertical displacement versus height values for $b = 20$ cm and $f = 1$ GHz .....  | 95  |
| Figure 6.18 The 2D plot of electric field distribution variation due to vertical displacement versus height values for $b = 20$ cm and $f = 1.5$ GHz .....  | 95  |
| Figure 6.19 The 3D plot of vertical displacement versus height versus total electric field for $b = 20$ cm and $f = 500$ MHz .....  | 96  |
| Figure 6.20 The 3D plot of vertical displacement versus height versus total electric field for $b = 20$ cm and $f = 1$ GHz .....  | 96  |
| Figure 6.21 The 3D plot of vertical displacement versus height versus total electric field for $b = 20$ cm and $f = 1.5$ GHz .....  | 97  |
| Figure 6.22 The graph shows x displacement versus the measured voltage for $b = 20$ cm, probe height = 10 cm and $f = 100$ MHz .....  | 101 |
| Figure 6.23 a) The graph shows x displacement versus the measured voltage for $b = 20$ cm, probe height = 10 cm and $f = 500$ MHz b) The graph shows x displacement versus the measured voltage for $b = 20$ cm, probe height = 10 cm and $f = 1$ GHz ..... | 102 |
| Figure 6.24 The graph shows x displacement versus the measured voltage for $f = 500$ MHz, probe height = 10 cm and $b = 10$ cm .....  | 103 |
| Figure 6.25 The graph shows x displacement versus the measured voltage for $f = 500$ MHz, probe height = 10 cm and $b = 50$ cm .....  | 104 |

|  |     |
|--|-----|
| Figure 6.26 The graph shows x displacement versus the measured voltage for $f = 500$ MHz, probe height = 10 cm and $b = 100$ cm .....  | 105 |
| Figure 6.27 The graph shows x displacement versus the measured voltage for $f = 600$ MHz, probe height = 10 cm, $b = 100$ cm and $a = 5$ cm .....  | 106 |
| Figure 6.28 The graph shows x displacement versus the measured voltage for $f = 600$ MHz, probe height = 10 cm, $b = 100$ cm and $a = 55$ cm .....   | 107 |
| Figure 6.29 The interference fringe pattern for the values of probe height = 10cm, $f = 200$ MHz and $b = 60$ cm .....   | 109 |
| Figure 6.30 The graphs show the increase in relative amplitudes of side interference fringe patterns a) The interference fringe pattern for the values of probe height = 10 cm, $f = 500$ MHz and $b = 50$ cm b) The interference fringe pattern for the values of probe height = 10 cm, $f = 500$ MHz and $b = 100$ cm..... | 111 |
| Figure 6.31 The graphs show x displacement versus relative amplitude values for each depth from $b = 10$ cm to $b = 100$ cm and probe height of 10 cm a) The 2D plots are for $f = 1$ GHz b) The 2D plots are for $f = 500$ MHz.....   | 113 |
| Figure 6.32 The graph shows how the measurement is performed in XDVRA graphs. It is for $b = 10$ cm, $f = 1$ GHz and probe height of 10 cm.....  | 114 |
| Figure 6.33 The graph shows depth versus FWHMX for probe height of 10 cm and $f = 500$ MHz .....   | 115 |
| Figure 6.34 The graph shows depth versus FWHMX for probe height of 10 cm and $f = 1$ GHz.....  | 116 |
| Figure 6.35 The graph shows frequency versus depth versus FWHMX for probe height of 10 cm and radius ( $a$ ) of 5 cm .....   | 117 |
| Figure 6.36 First graph shows x displacement versus measured voltage values and second graph shows x displacement versus photodetected voltage values for $f = 200$ MHz and $b = 10$ cm .....  | 127 |
| Figure 6.37 First graph shows x displacement versus measured voltage values and second graph shows x displacement versus photodetected voltage values for $f = 200$ MHz and $b = 100$ cm .....   | 127 |
| Figure 6.38 First graph shows x displacement versus measured voltage values and second graph shows x displacement versus photodetected voltage values for $f = 1$ GHz and $b = 10$ cm.....   | 128 |

|   |     |
|---|-----|
| Figure 6.39 First graph shows $x$ displacement versus measured voltage values and second graph shows $x$ displacement versus photodetected voltage values for $f = 1$ GHz and $b = 100$ cm..... | 128 |
| Figure 6.40 The graph shows an example of the smallest voltage variation .....  | 129 |
| Figure 6.41 The graph shows depth versus attenuation of wet soil at $f = 200$ MHz   | 131 |
| Figure 6.42 The graph shows depth versus attenuation of wet soil at $f = 1$ GHz....   | 131 |
| Figure A.1 The screen capture of the system in OPTIWAVE.....  | 149 |

## LIST OF ABBREVIATIONS

|        |  |
|--------|--|
| A/D    | Analog to Digital  |
| APD    | Avalanche Photodiode   |
| CO     | Common Offset  |
| CMP    | Common Mid-point   |
| CW     | Continuous Wave  |
| DF     | Direction-finding  |
| EA     | Electroabsorption  |
| EM     | Electromagnetic  |
| EMI    | Electromagnetic Interference                                       |
| E/O    | Electrical to Optical  |
| FWHM   | Full Width Half Maximum  |
| FWHMX  | Full Width Half Maximum of Relative Amplitude's Distance to Origin |
| GPR    | Ground Penetrating Radar   |
| InGaAs | Indium Gallium Arsenide  |
| LD     | Laser Diode  |
| LED    | Light Emitting Diode   |
| LPGF   | Low Pass Gaussian Filter   |
| MOM    | Method of Moments  |
| MUSIC  | Multiple Signal Classification                                     |
| MZ     | Mach-Zhender   |

|       |   |
|-------|---|
| OFS   | Optical Fiber Sensor                      |
| OFSIS | Optical Fiber Sensor Interrogation System |
| O/E   | Optical to Electrical                     |
| PD    | Photodetector                             |
| PPF   | Perfluorinated Polymer                    |
| PIN   | Positive Intrinsic Negative               |
| PM    | Phase Modulation                          |
| PMMA  | Polymethylmethacrylate                    |
| PN    | p-type and n-type                         |
| RF    | Radio Frequency                           |
| SAR   | Synthetic Aperture Radar                  |
| SNR   | Signal to Noise Ratio                     |
| SPR   | Surface-penetrating Radar                 |
| TDR   | Time Domain Reflectometry                 |
| TE    | Transverse Electric                       |
| Tx    | Transmitter                               |
| TEM   | Transverse Electromagnetic                |
| UWB   | Ultra Wide Band                           |
| WARR  | Wide-angle Reflection-refraction          |
| XDVRA | X Displacement versus Relative Amplitude  |
| 2D    | Two Dimensional                           |
| 3D    | Three Dimensional                         |

# CHAPTER 1

## INTRODUCTION

Ground penetrating radar (GPR) is considered to be one of the most promising technologies for detecting, imaging and mapping of the subsurfaces. Its main function is to search for the presence of the subsurface objects by identifying their position beneath the surfaces. Subsurfaces can include different types of media such as rock, ice, soil, structures and much more.

The terms ‘ground-probing radar’, ‘ground penetrating radar (GPR)’, ‘sub-surface radar’ or ‘surface-penetrating radar (SPR)’ refer to different kinds of electromagnetic (EM) techniques that are designed for determining the position of buried objects or interfaces beneath the surfaces. Among these terms, GPR is used widely to describe the technique and it is now a worldwide accepted EM geophysical technique which is used in different kinds of applications [1].

The operating principle of a typical GPR system is as follows. A typical GPR system comprises of a transmitting and a receiving antenna. GPR systems work by sending an EM wave through a wideband antenna into the subsurface. The wideband antenna is considered as the transmitting antenna. Whenever the wave faces any EM property contrasts, it will be scattered. When the wave travels into the subsurface and hits any electrical or magnetical parameter discontinuity, there will be scattering and it will make a reflection. The reflections then come back up to the surface. The reflections coming up to the surface are measured and recorded by the receiving antenna. Those recorded measurements are then processed. After the data is achieved, it is displayed

on a printed paper or a computer [2]. A block diagram of a typical GPR system is shown in Figure 1.1 below.

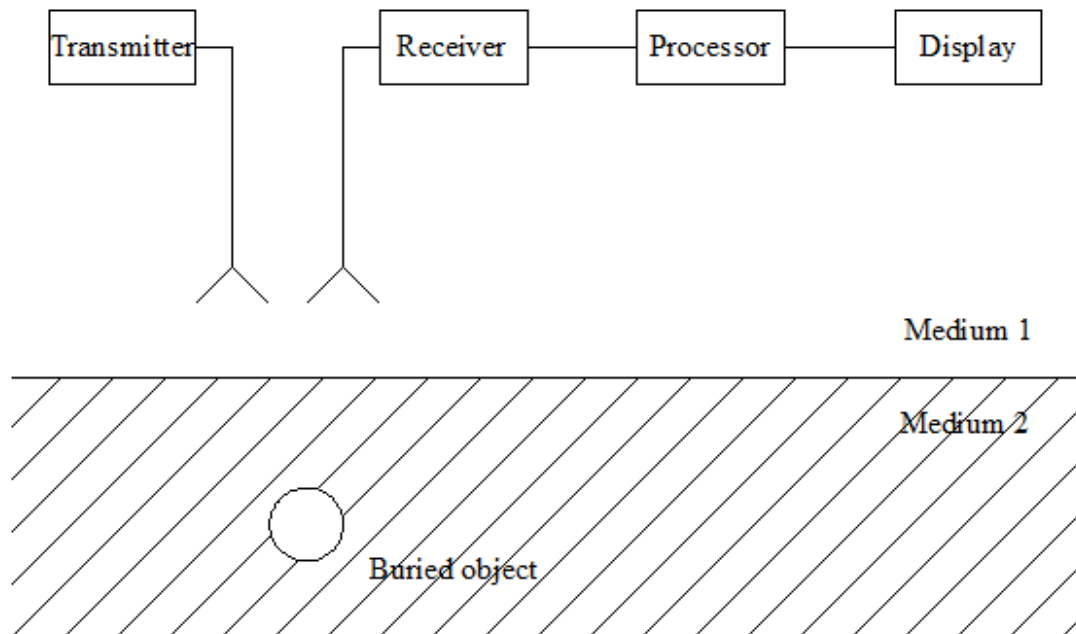


Figure 1.1: The block diagram of a typical GPR system [1]

The GPR system that is used in the study is as follows. It comprises of a transmitter, a target (a circular cylinder) and an optical fiber sensor interrogation system (OFSIS). This configuration is shown in Figure 1.2.

As seen in Figure 1.2, there are two mediums. Medium 1 is taken as air and medium 2 is taken as dry soil. The circular cylinder is deeply buried inside the dry soil. Tx stands for the transmitter. OFSIS comprises of a light source (laser as a transmitter), an optical fiber sensor (OFS) and a photodetector (as a receiver). The operating frequency of the system is taken between 100 MHz to 1 GHz. The reason of this is as follows. When the frequency is lower than 100 MHz, the antenna cannot collect the

signals. When the frequency is higher than 1 GHz, surface roughness will create scattering interference patterns.

A sensor is a device that converts the measured quantities into a readable form. OFS is a device that converts the optical signals into electrical signals. OFSIS is an optical communication system. Its main goal is sending a signal to start a response in order to obtain information.

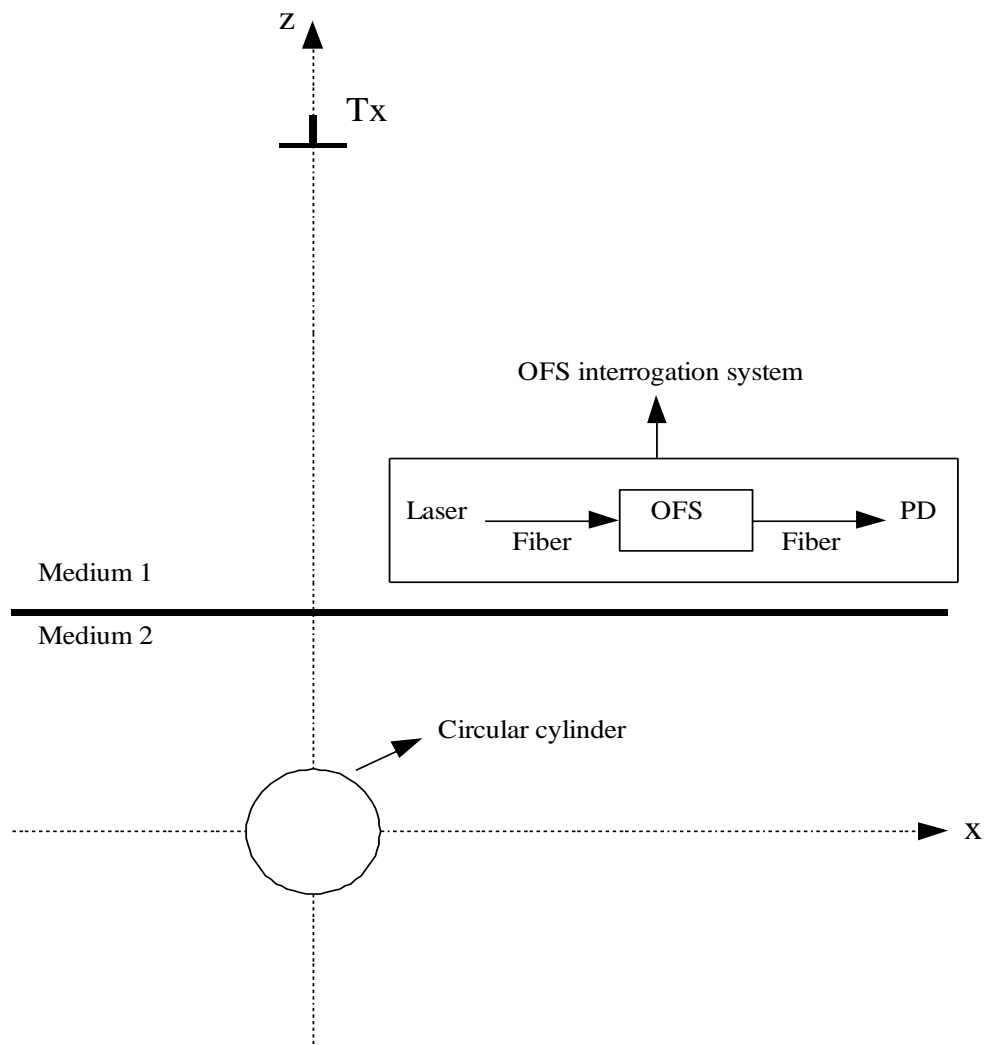


Figure 1.2: The configuration of the GPR system that is used in the study where PD stands for photodetector

There are many reasons which make OFS attractive for sensing. Using OFS offers many advantages. Some of them are as follows: OFS makes detection efficiently and faster. It is not affected by the outside effects. It is immune to radio frequency especially to electromagnetic interference (EMI). Detection is performed with low loss and large bandwidth. Due to its small size, it is easier to carry and control. It is superior to RF systems because it has lower noise. So it can offer a sensor technology which is small, easy to carry, multiplexable, easy interface with optical communication systems, secure and not affected by EMI [3], [4]. The advantages of OFS can be expanded. Besides all advantages, OFS has a disadvantage that the cost of OFSs is more than other types of sensors. The advantages and the disadvantages of OFSs are explained in more detail in Section 5.8.

The purpose of this study is to detect the buried cylinder's depth and position. This is performed using a GPR system which comprises of an OFS. In order to determine the position and the depth of the cylinder, MATLAB R2007b and OPTIWAVE OPTISYSTEM 7.0 programs are used. The detailed analyses of how those are performed are explained in Chapter 6. After determining the place of the object, noises are added to the system. By this way it is observed that frequencies at which the system operates better. The depth limits are also observed for various frequencies.

The organization of the thesis is as follows: the next chapter involves the literature survey which is related to the thesis subject. Chapter 3 describes the basic principles and important concepts of GPR. It involves a review of GPR. Chapter 4 describes how the total scattered electric field due to cylinder and interface (or the electric field distribution at the OFS) is obtained. Those are needed for determining the cylinder's depth and position. The basic principles and important concepts of OFS are described in Chapter 5. It involves a review of OFS. Chapter 6 includes the implementation of GPR using an OFS. The work performed in this chapter shows step by step how the depth and the position of the object are obtained. The simulation results are also shown in this chapter. Finally, the thesis is concluded in Chapter 7.

## **CHAPTER 2**

### **LITERATURE SURVEY**

Although the first study on GPR was attributed to Hülsmeier in 1904, the techniques were developed from 1930s. The range of applications has been increasing from 1970s [1].

The basic principles of OFSs have been perceived for more than forty years. The technology related to them has shown itself for over twenty years. The market growing rate has increased 50% per year due to the growing interest on OFSs since 2008 [4].

Although there are many studies related to solely GPR or to solely OFS, there are not many studies related to both GPR and OFS. The important studies related to the thesis subject are searched within the scientific literature and they are explained below.

The estimation of the direction of the waves is obtained in [5]. This is performed in a borehole using an OFS array. Borehole is a type of radar that is used in places where GPR cannot reach. The experiments are performed with two dipole array antennas which are the receivers in borehole and the transmitter is set 0.9 m away from the borehole. The operating wavelength is longer than the available space in antennas. It is larger than 0.3 m. The borehole radar comprises of an OFS which is used for converting the electrical signals into optical signals. The directions of the incoming waves or the source positions are estimated using borehole radar with optical modulator. Multiple Signal Classification (MUSIC) Algorithms using Method

Of Moments (MOM) technique is applied to array data and it is used for estimating the source position by borehole. MUSIC algorithm is a technique which is used for estimating the frequency content of the signal by a method of eigenspace. MOM is a technique which is used for solving EM boundary or integral equations of volume in frequency domain. It is very useful for scattering and radiation problems because the magnetic sources are of interest [6].

When the study of this thesis is compared to the previous work [5], there are various differences. The transmitter is placed 100 m above from the interface in the study. GPR is used instead of borehole radar. The receiver comprises of a short dipole and it moves back and forward along x axis to obtain the voltages. The electric field probe length is taken as 5 cm and it is smaller than half of the wavelength. The voltages are obtained from the electric field distribution which is obtained from the Green's function. The measured voltages are used to detect the cylinder's depth and position.

The landmines are detected by a bistatic type of GPR system in [7]. The system uses a transverse electromagnetic (TEM) horn antenna as a transmitter and a passive optical sensor as a receiver. The sensor comprises of a dipole antenna which has a length of 30 cm. A vector network analyzer is used as a receiver or a transmitter. As a whole the system operates as a stepped frequency radar system. This system needs long time to acquire data although it has high signal to noise ratio (SNR). The operating frequency of the system varies between 3 MHz to 2.4 GHz. A laboratory experiment is set up. The transmitter is kept at a fixed position and a metallic sphere, which has a diameter of 75 mm, is buried inside a sandbox. It has a depth of 25 mm. The sandbox includes dry sand of permittivity 3. The sensor scans the surface using a positioner. The signal achieved is used for synthetic aperture processing and the two dimensional (2D) images of the buried object are obtained.

The landmines are also detected by a GPR system in [8]. The configuration and the methods of the system are same as the one used in [7]. The system is improved using a broadband optical electric field sensor the bandwidth of which varies from

100 MHz to 5 GHz. The laboratory experiment's configuration is also the same except the target has a depth of 5 cm. The target is buried in a dry sand of permittivity 2.5. Although the buried object is detected clearly using this system, the plotted images are not clear due to inverse filtering error.

Land mines are detected efficiently by a bistatic GPR in [9]. It uses an optical electric field sensor. The configuration and the methods of the system are basically the same as the ones used in [7], [8]. One of the differences is as follows: the sensor is tested in both stepped frequency radar system and impulse radar system. The stepped frequency radar system comprises of a vector network analyzer, a transmitter and a receiver positioner which is controlled by a computer. Although it has high SNR, it needs long time to acquire data. The impulse radar system has the same equipments except that it comprises of a digital oscilloscope, an impulse generator and a diffraction stacking. The model is tested in impulse radar system because data acquisition is faster. Data acquisition is performed by two modes: stepped and continuous data acquisition. When the receiver acquires data in stepped data acquisition, it stops at each position. In continuous data acquisition, the receiver moves continuously while acquiring and it only stops at the ending point of the scanning lines. The mine is detected clearly in both of the acquisition modes but better scanning velocity is obtained in continuous data acquisition.

A bistatic ultra wide band (UWB) radar system is also introduced in [10]. The configuration of the system is basically the same as the ones used in [7], [8], [9] except time domain data acquisition system is placed instead of vector network analyzer. The system is a bistatic synthetic aperture radar (SAR) which comprises of a TEM horn antenna as a transmitter, an OFS as a receiver, a pulse generator for transmitter and a digitizing oscilloscope for receiver. The system operates as an impulse radar system. The operating frequency of the system is 5 GHz. The receiving antenna scans the area using a positioner. The data is acquired faster by this way. Data is preprocessed by pulse compression and diffraction stacking algorithm is used for image reconstruction. Diffraction stacking algorithm is a process of summing and

averaging for an improved data and for a higher SNR. A laboratory experiment is set up and a metallic sphere is detected clearly using this system.

A bistatic radar system for detection of buried objects is developed in [11]. The configuration of the system is basically the same as the ones used in [7], [8]. Diffraction stacking is used for reconstruction of images. The incoming signal from the transmitter is very strong so the received signal suffers from this effect. F-k filtering algorithm (k shows the spatial frequency and F shows the frequency) is developed to overcome this difficulty. This algorithm can be explained as follows. F-k spectrum distribution is obtained from the minimum and the maximum value of horizontal velocity of the direct wave. The spectrum component of direct wave in F-k domain needs to be suppressed. Inverse Fourier transformation is applied to determine the signal in time domain. After high pass filtering is applied to suppress the direct signal. So signal processing is performed by F-k filtering. It is performed by suppressing the strong transmitted signal in order to achieve clear images. A laboratory experiment of the system is set up to test the performance of this filtering. It is seen that the method works efficiently and it determines the subsurface objects clearly. It suppresses the effect of the strong incoming signal and it can also be applied to the new studies.

When the works [7], [8], [9], [10], [11] are compared to the study of this thesis, the configuration of the systems are similar except the proposed technique in this thesis does not require a vector network analyzer. The measurement methods used in the studies are different. The transmitter's location is different. It is 100 m above the soil surface in the study. Martian soil sample is used. The operating frequency of the system varies between 100 MHz to 1 GHz. The system is not tested in any data acquisition modes in the study. Although the system is not set up in the laboratory environment, the MATLAB code of the optical sensor is written in order to simulate the measurement of the voltages induced in the OFS. After measuring the voltages, the depth and position of the cylinder are estimated using MATLAB and OPTIWAVE programs.

An array type of directional borehole radar system is developed in [12]. A general borehole radar system can detect the range to a target from the radar but it cannot detect the target's azimuth location. This work is developed to overcome this difficulty. The system uses a dipole antenna as a transmitter and four optical electric field sensors as a receiver. The azimuth angle of the target is determined from the phase differences among the sensors. A laboratory experiment is set up to observe the effects of the mutual coupling and to test the ability of obtaining small phase difference. The system operates as a stepped frequency radar system. The transmitting antenna is connected to the network analyzer by a 50 m optical fiber. The network analyzer is also connected to the sensors by optical fibers through a switch and a detector. The sensors are arranged evenly on circumference. The positions of the receiver antennas are changed manually to acquire the datas. The operating frequency of the system varies between 100 MHz to 401 MHz. As a result, small phase differences are observed and distortions are caused by mutual couplings.

A direction finding algorithm is developed in [13]. Its main purpose is to obtain three dimensional (3D) imaging of targets inside the subsurface. The transmitting antenna is a dipole antenna of length 90 cm. The receiver comprises of OFS with four uniform circular array antennas attached to electrodes. In order to achieve the azimuth sensitivity, Adcock direction-finding (DF) algorithm is developed. This algorithm is applied to field measurement data and it is based on Adcock DF antenna principle in which the optimization, the filtering procedure and the complex time series expression are combined to provide an accurate estimation. This algorithm is first configured as cross-hole to detect azimuth direction. In cross-hole configuration the transmitting antenna is fixed in borehole and the receiving antenna is scanned along the borehole by keeping a fixed distance of 15 m between them. After it is configured as single-hole. In single-hole configuration, the receiver and the transmitter are lying on the same line inside the borehole. Shortly, the borehole radar is equipped with transmitter and receiver antennas which suffer from azimuth ambiguity. As a result, the 3D location of the subsurface objects is detected correctly.

A directional borehole radar system is also developed to detect 3D location of a subsurface tunnel in [14]. The receiver comprises of an array of optical electric field sensors. The system is configured as single-hole and it is a stepped frequency radar system which uses vector network analyzer. Adcock DF antenna principle is also applied to detect azimuth direction. As a result of this study it is observed that the system is good at acquiring coherent signals which helps to estimate the azimuth. The 3D location of subsurface tunnel is detected and the azimuth location of the tunnel is estimated. The experiments are performed with the same antenna configuration by RAMAC directional borehole radar system. The elements of the RAMAC system is the same as the stepped frequency radar system except that it comprises of metallic parts such as A/D (analog to digital) converters, O/E (optical to electrical) converters and batteries in the receiver. The two results are consistent; both of them give the same results. The 3D location of subsurface tunnel detection and the azimuth locating are validated.

A directional borehole radar system which uses optical electric field sensors are developed in [15]. The system comprises of a single dipole antenna as a transmitter and four dipole circular arrays as a receiver. The phase differences between four dipole antennas and the azimuth direction of incoming reflection wave are measured by the receiver array. A laboratory experiment is set up to see the effects of the mutual coupling and to observe the accuracy of phase difference. The system operates as a stepped frequency radar system. The transmitting antenna is connected to the network analyzer by an E/O (electrical to optical) converter. The network analyzer is also connected to the sensors by optical fibers through a switch and a detector. The sensors are arranged evenly on circumference. Single-hole and cross-hole borehole radar measurements are carried out. The peak power of the system, which is 70 MHz, is determined from the cross-hole measurement. The azimuth orientation of subsurface fractures is estimated using single-hole measurement configuration. An in situ calibration technique is developed due to differences in sensitivity. This technique can be explained as follows. The signals are achieved for different depths of each sensor. The average of these signals is taken and the received signal spectrum at each depth is normalized by averaged signal spectrum. This

equalizes the sensitivity of each receiver. By combining this technique with single-hole measurement configuration, the azimuth orientations are obtained.

A high range resolution directional borehole radar is also developed in [16]. The configuration of the system is basically the same as the one used in [15]. The system comprises of a single dipole antenna as a transmitter and four dipole circular arrays as a receiver. The azimuth direction of a reflected wave is determined by the phase differences among four dipole elements. The voltages are measured by optical electric field sensors. Highly correlated signal is achieved because OFS has high electric isolation. A switch is used to reduce mutual coupling between the dipole elements. An experiment is set up in a test site. Single-hole and cross-hole borehole radar measurements are carried out. The peak power of the system, which is 70 MHz, is determined from the cross-hole measurement. The azimuth orientation of subsurface fractures is estimated using single-hole measurement configuration. A simple algorithm is developed for determining the azimuth orientation. It arises from the rotations of the radiation pattern. By adding this algorithm to the system the reflected wave's azimuth angle is obtained clearly. The 3D orientation of subsurface fractures can also be imaged. By looking at the results of the experiment it can be concluded that the system determines small phase difference when there is sufficient SNR. This amount of difference is enough for estimating the azimuth angle.

When the previous works [12], [13], [14], [15], [16] are compared to the study, it is observed that the configuration and the methods of the systems are different. A single OFS is used in the study and the network analyzer is not used. The azimuth angle and the azimuth direction are not calculated but the depth and the position of the target are determined. The elements of the systems may be the same but their purposes are different.

## **CHAPTER 3**

# **GENERAL REVIEW OF GROUND PENETRATING RADAR (GPR)**

### **3.1 Introduction**

GPR is now a well-accepted EM geophysical method which is used for investigating subsurfaces [17]. Moreover it is used for detecting in high resolution, imaging and mapping of subsurfaces. Subsurfaces can include different types of media such as rock, ice, soil, structures and much more.

EM wave propagation and scattering principles are used to image and locate the buried objects in the ground. GPR can provide high resolution imaging and depth estimation of the subsurface objects. Those are achieved accurately without time consuming. GPR can obtain much information such as: orientation, geometry of the buried objects, depth, water content of soils and much more. GPR is also used in many applications such as engineering, environmental, archeological and much more [17].

### **3.2 Basic Principles**

#### **3.2.1 Operating Principle**

A short high-frequency EM wave is sent from the transmitting antenna into the subsurface. When there is an EM property contrast between mediums, there will be

refraction at the interface and the wave will propagate from medium 1 to medium 2. When the wave hits a buried object or a medium with different EM properties, part of the wave will be diffracted and there will be reflection. The reflections from the subsurface are detected and measured by the receiving antenna. The measurements are recorded and they are later processed and displayed [18]. The block diagram of a typical GPR system is shown in Figure 1.1.

Any EM parameter discontinuity (i.e. a buried object or a medium with different relative permittivity ( $\epsilon_r$ ) or relative permeability ( $\mu_r$ ) or conductivity ( $\sigma$ )) causes a reflection. The higher the relative permittivities' difference, the more intense the buried object becomes. As the waves are transmitted to the buried object, their velocity will change depending on the material through which they are travelling. The propagation velocity ( $v$ ) of the EM wave is determined by the relative permittivity of the material. The relative permittivity is defined as the capacity of a material to store a charge when an electric field is applied and it is closely related to the permittivity ( $\epsilon$ ) of a material.

The time it takes for a wave going from transmitting antenna to the receiving antenna is called the travel time and it is used to determine the propagation velocity of the material. The travel times are measured in nanoseconds. Since the propagation velocity is inversely proportional to the square root of the permittivity, the materials with smaller permittivity have higher velocity. The materials with high velocity also have a high travel time.

The amplitude and the attenuation of the propagating wave are determined by the relative permeability and the conductivity of the material. The relative permeability is defined as the capacity of a material to get magnetized when a magnetic field is applied and it is closely related to the permeability ( $\mu$ ) of a material. The higher the relative permeability and conductivity values get, the higher the amplitude and attenuation values become. This also results in worse data quality and penetration depth [2].

So when the travel time and the propagation velocity of a wave are known, the penetration depth can be estimated easily and accurately. In order to achieve a good resolution, high frequencies are needed. However the penetration depth of fields is inversely proportional to the frequency [2].

In order to operate successfully, GPR needs to meet some requirements. It needs to have an adequate SNR, an adequate signal to clutter ratio, an adequate depth resolution of the target and an adequate spatial resolution of the target [1], [19].

### **3.2.2 Scattering of Electromagnetic (EM) Waves**

When a wave travels from medium 1 to medium 2, it faces an object with different EM properties. Then the direction of the wave will change. This process is called scattering. There are four types of scattering: a) spectral reflection scattering, b) refraction scattering, c) diffraction scattering and d) resonant scattering. Spectral reflection scattering is used mainly in most of the researches.

Spectral reflection scattering is based on the law of reflection. When a wave is transmitted to a different medium, part of the wave can make a reflection at the interface. The law of reflection states that when a wave reflects off a surface, the angle of incidence is equal to the angle of reflection [2], [18]. The configuration of the spectral reflection scattering is shown in Figure 3.1.a.

Scattering happens depending on the geometry of the interface and the EM property contrasts. When a wave is transmitted to a different medium, other than making reflection at the interface part of the wave can travel into the other medium by making refraction. This type of scattering is called refraction scattering. The configuration of the refraction scattering is shown in Figure 3.1.b.

Diffraction is the bending of the EM waves and diffraction scattering takes place when a wave is partially blocked by a sharp boundary. When there is diffraction, the wave scatters off a point and emits in many directions. Diffraction happens

depending on the shape of the objects and boundaries. The configuration of the diffraction scattering is shown in Figure 3.1.c.

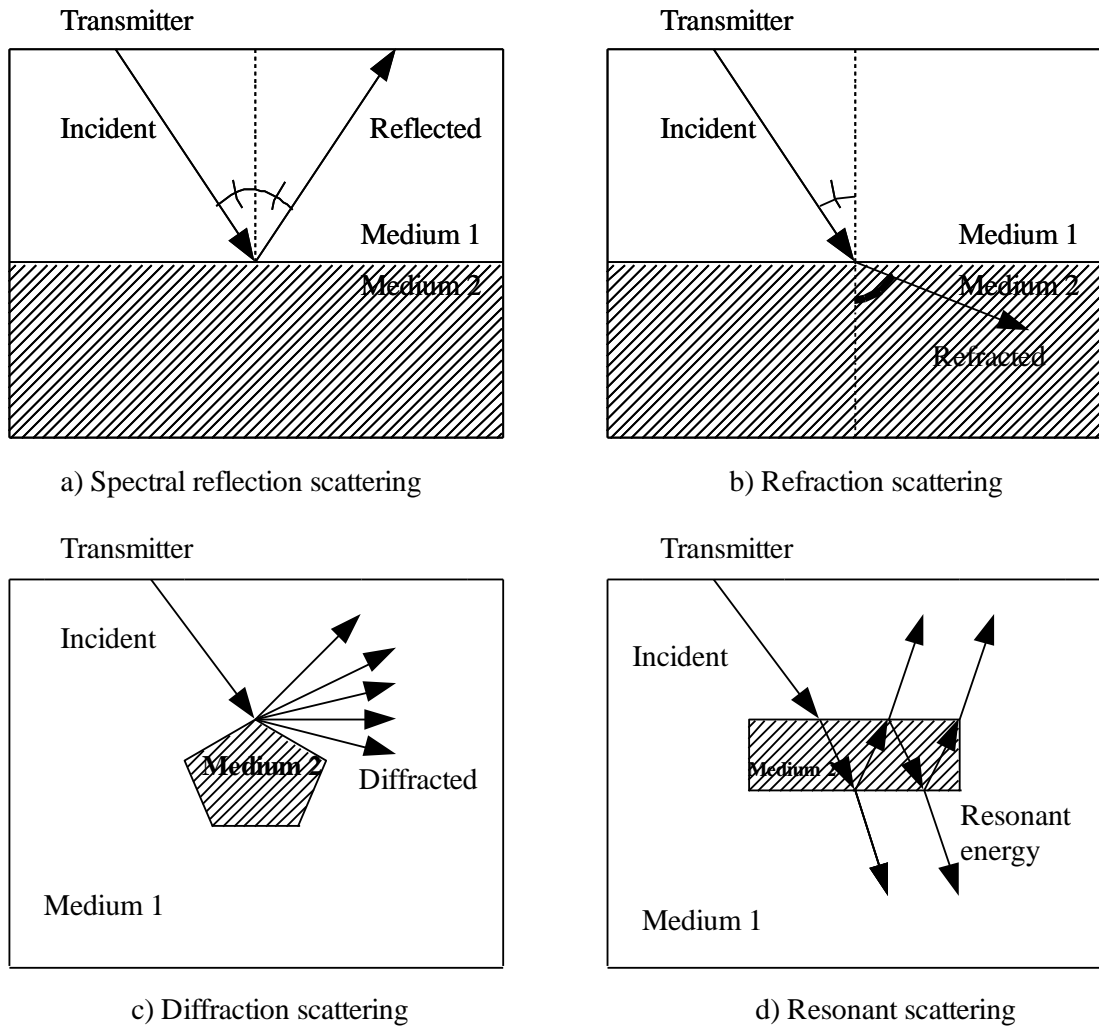


Figure 3.1: Scattering types: a) spectral reflection scattering, b) refraction scattering, c) diffraction scattering and d) resonant scattering

When a wave hits a closed object, the wave bounces many times within the boundary of the object. Inside the boundary of the object, part of the wave is refracted outside and part of the wave is reflected inside. This happens many times and causes the EM

energy to resonate within the object. The energy then diffuses outside the object. This process is called resonant scattering. Resonant scattering happens depending on the wavelengths [2], [18]. The configuration of the resonant scattering is shown in Figure 3.1.d.

### 3.2.3 Electromagnetic (EM) Wave Propagation in Subsurface Material

GPR is used to measure the EM reflections from the subsurfaces. The EM wave behaviour is based on the electrical conductivity of the materials. Depending on the conductivity property, the propagation of the EM field as an EM wave changes. When the material is conductive, the EM field can not propagate as an EM wave. Conversely when the material is dielectric, the EM field can propagate as an EM wave. When the frequency is changed, the material properties change too. Although higher frequency changes result in a higher attenuation, it also affects all the materials to behave as a dielectric. Electrical conductivity, permittivity and permeability are the most important parameters of materials and any material behaves as dielectric in high frequencies [20].

### 3.2.4 Physical Basis

EM wave propagation is an important principle for understanding the basic operations of GPR. The propagation of EM waves is controlled by several factors such as the geometry and the physical properties of the medium. Relative permittivity, relative permeability and the conductivity are the physical properties that help to understand these operations. The relationship among relative permittivity, relative permeability and index of refraction is defined as

$$n = \sqrt{\frac{\epsilon\mu}{\epsilon_0\mu_0}} = \sqrt{\epsilon_r\mu_r} \quad (3.1)$$

where

$n$  = index of refraction,  $\epsilon$  = permittivity,  $\mu$  = permeability,  $\epsilon_0$  = permittivity of free space,  $\mu_0$  = permeability of free space,  $\epsilon_r$  = relative permittivity,  $\mu_r$  = relative permeability.

### 3.2.4.1 Permittivity and Relative Permittivity

Permittivity is defined as the capability of a material to polarize and the storage of the energy when an external field is applied [21]. It is in complex form where the real part of the permittivity ( $\epsilon'$ ) describes the energy storage and can be written as

$$\epsilon' = \epsilon = \epsilon_r \epsilon_0 \left[ \frac{F}{m} \right] \quad (3.2)$$

The imaginary part of the permittivity ( $\epsilon''$ ) describes the energy loss and can be written as

$$\epsilon'' = \sigma / \omega \left[ \frac{F}{m} \right] \quad (3.3)$$

where

$\omega$  = angular frequency and  $\sigma$  = conductivity.

Relative permittivity (dielectric constant or dielectric permittivity) is defined as the capacity of a material to store a charge when an electric field is applied and it is closely related to the permittivity of a material. The relationship is written in Equation 3.2 above. Using this equation, complex form of the relative permittivity can be written as

$$\epsilon_r = \left( \frac{\epsilon'}{\epsilon_0} - i \frac{\epsilon''}{\epsilon_0} \right) \quad [dimensionless] \quad (3.4)$$

Relative permittivity is a useful parameter in GPR studies. It controls the propagation velocity and the wavelength. After finding the wavelength, the resolution can be determined. Lower relative permittivity results in a higher propagation velocities and longer wavelengths. Longer wavelengths have lower resolution [2], [22].

### 3.2.4.2 Permeability and Relative Permeability

Permeability is described as the capability of a material to store magnetic energy when an induced magnetic field is applied. It is in complex form where the real part of the permeability describes the energy storage and the imaginary part of the permeability describes the energy dissipated [2], [22].

Relative permeability is defined as the capacity of a material to get magnetized when a magnetic field is applied and it is closely related to the permeability of a material. This relationship is written as

$$\mu_r = \frac{\mu}{\mu_o} \quad [dimensionless] \quad (3.5)$$

The value of permeability for most of the nonferromagnetic materials is approximately equal to the free space permeability for most of the rocks, soils and sediments. Free space permeability is equal to

$$\mu_o = 4\pi = 10^{-7} \quad [H/m] \quad (3.6)$$

As it is mentioned above for most of the rocks, soils and sediments  $\mu \approx \mu_o$ . Then using Equation 3.5, it can be seen that the value of the relative permeability is approximately equal to 1.

### 3.2.4.3 Conductivity

Electrical conductivity is described as the ease of the electron movement when an external electric field is applied. The EM wave behaviour is based on the electrical

conductivity of the materials. Depending on the conductivity property, the propagation and the penetration of the EM field as an EM wave change [2], [22].

The electrical current propagates through rocks and minerals. This is performed with three methods. These are ohmic, electrolytic and dielectric. Ohmic conduction requires free electrons like the ones found in metals. Electrolytic conduction requires ions to hold and move the charges. Those are like the ones found in groundwater. Dielectric conduction requires atoms to produce currents. Those are like the ones found in soils, sediments and rocks.

Conductivity is related to the imaginary part of the permittivity. This relationship is shown in Equation 3.3. It also attenuates the propagation of the EM waves. If the conductivity and the frequency values are increased, the attenuation becomes larger. The electrical conductivity is used to estimate the signal attenuation constant ( $\alpha$ ). The related equations are written as

$$\alpha = \frac{\sigma}{2} \sqrt{\frac{\mu_r \mu_0}{\epsilon_r \epsilon_0}} \quad [Neper/m] \quad (3.7)$$

$$\alpha = \sqrt{\pi f \mu_r \mu_0 \sigma} \quad [Neper/m] \quad (3.8)$$

where

$f$  = frequency in hertz and  $\sigma$  = conductivity.

The equations above show that the signal attenuation constant value depends on the permittivity, permeability, conductivity, frequency and angular frequency values. Equation 3.7 can be used for materials that are low-loss dielectric medium. Equation 3.8 can be used for materials that are conductors. The results of these equations are correct under the estimation of ferromagnetic materials are not present [2], [22].

### **3.3 Processing**

The acquired data takes some processing steps most of the time. The processing can be different depending on the type of GPR system. The general objective of processing is to present an image that can be interpreted easily and test the returned wave depending on some procedures. It is needed for reducing the clutter and achieving a higher SNR.

#### **3.3.1 Normal Processing**

The way of processing changes depending on the type of the GPR system. A little more messaging of the raw field records is required in monostatic systems.

##### **3.3.1.1 Monostatic Processing**

The processing steps that might be applied to GPR data are static shifting to remove the time offset, subtracting average trace to remove banding, distance stretching for constant trace separation to remove the effects of nonconstant motion and amplifying gain to get stable amplitude variations in order to increase the visibility of the deeper parts of the image [23].

##### **3.3.1.2 Bistatic Processing**

The processing steps that might be applied to GPR data are static shifting to remove time offset and applying gain or amplifier to get stable amplitude variations.

#### **3.3.2 Advanced Processing**

Other filtering operations can be applied to GPR data. The processing steps that might be applied to GPR data are lateral averaging to improve SNR, frequency filtering to remove the unwanted high or low frequencies for more understandable GPR image, deconvolution to remove the effects of source for a better interpretation of GPR image and migration to correct the geometry of the subsurface in the GPR image [23].

### **3.4 Display**

When the data is acquired, it is displayed on a printed paper or a computer. The processed data closely approximates an image of the subsurface. In order to interpret the subsurface, a display is always helpful.

Mainly, there are three types of displays. These are one dimensional trace, two dimensional (2D) cross section and three dimensional (3D) displays. A trace is defined as the single recording of a transmitted pulse. One dimensional trace does not give enough information for us. A 2D cross section is obtained by placing traces side by side. A 3D display is obtained by placing traces in a block view. The wiggle trace comprises of the building block of all displays.

A single trace is used to detect objects. A wiggle trace is a common display that shows surface position versus travel time. GPR traces comprise of two types of wiggle trace cross sections [18].

Scan displays can be obtained by applying a colour on the wiggle trace display. There are two types of scan displays. These are gray-scale scan display and colour intensity scan display. A gray-scale scan display is obtained by applying black to white colours on wiggle trace display. A colour intensity scan display is obtained by applying a single colour to white colours on wiggle trace display.

3D displays are obtained by placing GPR traces in block views at different positions on the surface. In order to interpret the GPR data correctly, a valid 3D display is required. A simple image without the noise and the clutter is enough for a valid display. By looking at the display, the continuity of the reflection of the waves and the noise can be observed [18].

### 3.5 Applications

GPR has many applications in a variety of fields. These applications vary from measurement of dielectric constant, material parameters, thickness, detection of buried objects and much more. The applications are shown in Table 3.1.

Some important applications are discussed in more detail below.

Table 3.1: The applications of GPR [24]

|   |                           |   |
|---|---------------------------|---|
| <b>CIVIL AND STRUCTURAL ENGINEERING</b> | <b>Several</b>            | <ul style="list-style-type: none"> <li>- Void detection</li> <li>- Pavement thickness</li> <li>- Reinforced concrete locating</li> <li>- Pipe and cable locating</li> <li>- Wall and building conditioning</li> </ul>   |
|   | <b>Utilities</b>          | <ul style="list-style-type: none"> <li>- Pipe leak detection</li> <li>- Buried pipe and cable mapping</li> </ul>  |
| <b>GEOTECHNICAL AND GEOPHYSICAL</b>     | <b>Mining</b>             | <ul style="list-style-type: none"> <li>- Coal mining</li> <li>- Peat profiling</li> </ul>   |
|   | <b>Hazardous Waste</b>    | <ul style="list-style-type: none"> <li>- Hazardous waste mapping</li> <li>- Buried drums</li> <li>- Underground storage tank detection</li> </ul>   |
|   | <b>Several</b>            | <ul style="list-style-type: none"> <li>- Geological layer mapping</li> <li>- Earthquake fault mapping</li> <li>- Borehole inspection</li> <li>- Highway and tunnel excavations</li> <li>- Water table detection</li> <li>- Snow, ice and glacier profiling</li> </ul> |
|   | <b>Ordnance Detection</b> | <ul style="list-style-type: none"> <li>- Detection of buried mines</li> <li>- Detection of unexploded bombs</li> </ul>  |
| <b>TRANSPORTATION</b>                   | <b>Roads</b>              | <ul style="list-style-type: none"> <li>- Pavement thickness</li> <li>- Void detection</li> <li>- Road condition survey</li> </ul>   |
|   | <b>Railroads</b>          | <ul style="list-style-type: none"> <li>- Rail track and bed inspection</li> </ul>   |
|   | <b>Airports</b>           | <ul style="list-style-type: none"> <li>- Runway integrity testing</li> <li>- Remote sensing from aircraft and satellites</li> </ul>   |
|   | <b>Forensic</b>           | <ul style="list-style-type: none"> <li>- Security applications</li> <li>- Buried body and weapon detection</li> </ul>   |
|   | <b>Archaeology</b>        | <ul style="list-style-type: none"> <li>- Treasure finding</li> <li>- Cavity detection</li> </ul>  |

GPR is successfully used in forensic investigations. It is used for finding the buried victims of serial killers. It is also used for finding the buried weapons and some security applications.

In military applications, GPR is used for finding and mapping anti-personnel land mines, unexploded bombs and unexploded ordnance. It is also used for finding secret transmitters, receivers, microphones, internal boxes, secret rooms, tunnels, buried evidences and much more [1]. When compared to the other methods, GPR is the most effective one for reducing false alarm rate and it can detect both metallic and nonmetallic mines successfully.

Some methods can be time consuming for getting the right information about the subsurface conditions. GPR is used for surveying different types of geological underground layers. It is used for finding and mapping of granite, limestone, marble, hard rocks, water table, holes and much more. Those are performed quickly without making error and cost effectively.

GPR successfully detects the buried subsurface features. It is a cost effective tool for locating underground utilities. It can identify the depth and position of any human made objects such as pipes, power, water mains and sewage. The thickness and the voids of various layers can also be measured and mapped. The advantage of the method is that it is nondestructive and it has a high speed [1].

## **3.6 Design**

The terms and some concepts related to GPR are explained below.

### **3.6.1 Center Frequency**

The pulses' energy is concentrated mostly around the frequency which is called the center frequency ( $f_c$ ). GPR frequency is not defined by the bandwidth. The frequency needs to be kept as low as possible above the transition frequency. Attenuation comprises of electrical and scattering losses. If the frequency is

increased, the attenuation also increases. A wave penetrates into the medium easily with low frequencies.

Bandwidth to center frequency ratio is equal to

$$R = \frac{B}{f_c} \quad (3.9)$$

where

$B$  = bandwidth and  $f_c$  = center frequency.

The aim is keeping the value of  $R$  above unity. So by keeping this value above unity, the bandwidth needs to be maximized and the center frequency needs to be minimized. When the value of  $R = 1$  then  $f_c = B$  and GPR is characterized by its center frequency. This type of characterization is mostly achieved by GPRs [17].

### 3.6.2 Selection of the Antenna

Antennas are considered to be transducers that convert electric currents to EM waves. Antennas radiate EM energy when there is a change in the acceleration of the current on the antenna. Radiation takes place whenever the current changes its direction. The aim of the antenna design is to control the radiations. Antennas also convert the EM waves to currents. It can be understood that the receiving and the transmitting antennas are interchangeable. This only happens when the antennas are placed above the subsurface.

Dipole antennas are used in most of the GPR systems. A dipole antenna comprises of a pair of insulated metallic elements which are conductive. The dipole antennas are arranged as either monostatic or bistatic. Bistatic scattering is the case when the transmitting and receiving antennas are different. Monostatic scattering is the case when the transmitting and receiving antennas are the same. The pulse width of the transmitted pulse depends on the length of the dipole antenna. The longer the antenna gets, the broader the pulse becomes [18], [20], [24].

The plan resolution is determined by the characteristics of the antenna and signal processing. In order to get a worthy plan resolution, a high gain antenna is needed. Although high gain and small antenna dimensions require a high carrier frequency, it does not penetrate the ground material depth sufficiently. So by considering these issues; plan resolution, antenna size, signal processing and penetration of the material must be determined carefully [18], [20], [24].

### 3.6.3 Selecting Sampling Interval

Converting a continuous time signal into a discrete time numeric sequence is called sampling. The inverse of the sampling frequency is the sampling interval at which the incoming signals are sampled. Shortly the sampling interval is the time between samples. The Nyquist-Shannon Sampling Theorem Criterion states that if the sampling rate is higher than twice the bandwidth of the samples, a bandlimited analog signal can be reconstructed from sequence of samples [25]. This is defined as

$$f_s > 2B \quad (3.10)$$

where

$f_s$  = the sampling rate or the sampling frequency and  $B$  = the bandwidth.

Equation 3.10 can be rewritten as

$$B < \frac{1}{2T_s} \quad (3.11)$$

where

$T_s$  = the sampling period.

Conversely, the bandwidth must be less than half of the sampling period. The sampling theorem provides a method of reconstruction of the original signal from the sampled values and it also gives an upper bound on the sampling interval that is

required for reconstruction. The bandwidth is equal to the highest frequency only in baseband signals [25].

### **3.6.4 Operation Modes and Stacking**

Although there are different methods that are used in surface investigations, most surface investigations are made in reflection mode. In both of the continuous profiling and stationary point collection methods, a configuration of cross-line antenna is used. Dipoles are put perpendicularly to the profile direction in a cross-line antenna configuration.

In continuous profiling, while the GPR is scanning, the antennas are pulled along the profile. This profiling results in a nonuniform basic quality profile and it needs to be sampled again.

In stationary point collection, while the scans are being summed and averaged, the antennas are kept constant at the measurement point. The process of summing and averaging is called stacking. Stacking many times results in an improved GPR data and an increased SNR. When the data quality is good enough, the antennas are moved to the next stations. This is performed at uniform intervals along the profile by stacking each one at a time [2], [17], [23].

Survey design of GPR depends on the type of survey and the operating frequency of the source. Higher frequency sources result in better resolution but their penetration is not deep enough. Lower frequency sources are preferred for deeper penetration.

GPR operates at some modes such as: common offset (CO), common mid-point (CMP) and transillumination modes.

#### **3.6.4.1 Common Offset (CO) Mode**

The most common operation mode of GPR is the CO (common offset) or reflection mode. In this mode the antennas are moved along the survey line by keeping the distances between antennas constant. The EM pulses are transmitted at constant time

or distance intervals. The returned wave from the subsurface is recorded and displayed as GPR profiles on a computer screen. These profiles are displayed in two or three dimensional. In 2D profile, the vertical axis shows the two way travel time and the horizontal axis shows the measured distance. In 3D profile, the horizontal axis shows the distance along profile and one of the vertical axes show two way travel time and the other one shows the depth. Both the monostatic and the bistatic radar systems are used in CO mode [2], [17], [23]. The working principle of the CO mode is shown in Figure 3.2.

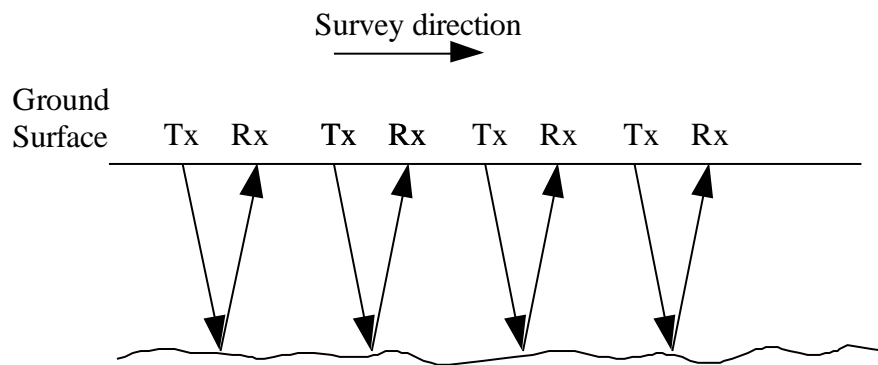


Figure 3.2: The working principle of GPR in CO mode

#### 3.6.4.2 Common Mid-point (CMP) Mode

The common mid-point (CMP) or wide-angle reflection-refraction (WARR) mode is used for establishing wave velocity. The CMP researches can be performed using bistatic antennas by increasing antenna separation of transmitting and receiving antennas for each point relative to a fixed midpoint. The acquired GPR profile consists of the received waves in a CMP. In 3D profile, the horizontal axis shows the distance between the transmitting and the receiving antenna and the vertical axis shows two way travel time [2], [17], [23]. Monostatic radar system can not be used

in CMP mode. Working in CMP mode results in an improved SNR and known wave velocity. The working principle of the CMP mode is shown in Figure 3.3.

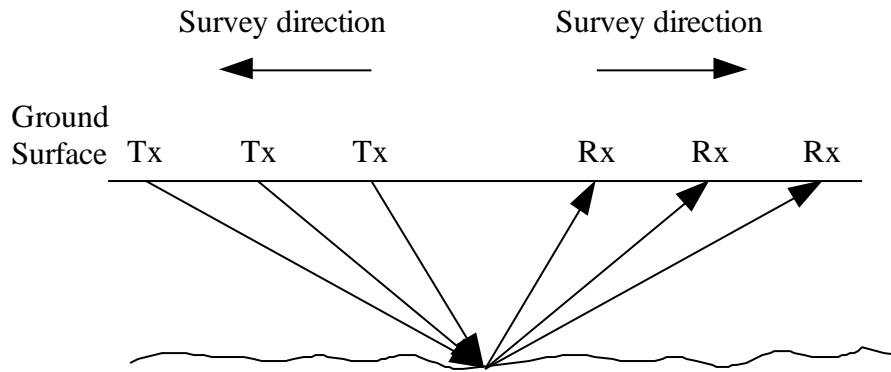


Figure 3.3: The working principle of GPR in CMP mode

### 3.6.4.3 Transillumination Mode

The least common operation mode of GPR is the transillumination mode. This mode is performed in two boreholes by lowering both the transmitting and the receiving antenna. After doing this the antennas are moved relative to each other to image the subsurfaces. This mode operates in transmission mode because the energy propagates through subsurfaces. Wave travel time and amplitude measurements are used to find the estimates of velocity and angle. In order to interpret GPR data measurements in transillumination researches correctly, the geometrical information is needed. Due to the deviations in the geometry, there may be errors in the values of velocity and angle [2], [17], [23]. The working principle of the transillumination mode is shown in Figure 3.4.

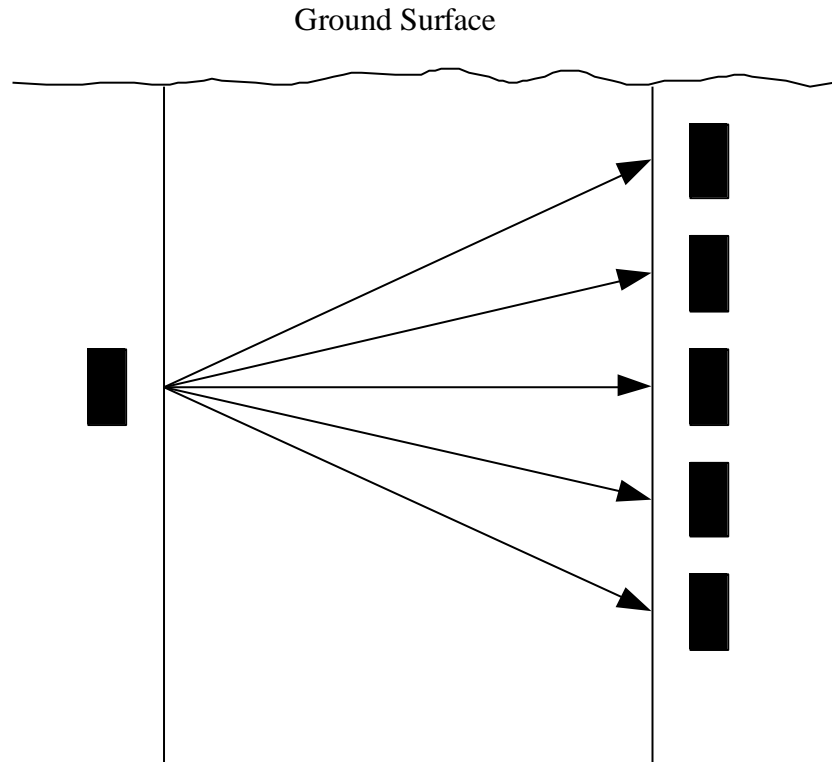


Figure 3.4: The working principle of GPR in transillumination mode

### 3.6.5 Wave Properties

Velocity, attenuation constant and EM impedance ( $Z$ ) are the key terms that are related to the wave properties. A sinusoidal time variation is undertaken in a simple medium with constant permittivity, permeability and conductivity. At low frequencies wave properties depend on the frequency. At high frequencies wave properties does not depend on the frequency. This happens when the permittivity, permeability and conductivity do not depend on the frequency [17]. The relationship among velocity, attenuation constant and the EM impedance can be understood from the equations below.

$$v = \frac{1}{\sqrt{\epsilon\mu}} = \frac{c}{\sqrt{\epsilon_r}} \quad (3.12)$$

By making some changes, Equation 3.7 can be rewritten as

$$\alpha = \sqrt{\frac{\mu}{\epsilon}} \frac{\sigma}{2} = Z_o \frac{\sigma}{2\sqrt{\epsilon_r}} \quad (3.13)$$

$$Z = \sqrt{\frac{\mu}{\epsilon}} = \frac{Z_o}{\sqrt{\epsilon_r}} \quad (3.14)$$

where

$c$  = speed of light and  $Z_o$  = the impedance of free space.

where

$$Z_o = \sqrt{\frac{\mu_o}{\epsilon_o}} \quad (3.15)$$

### 3.6.6 Resolution

Resolution is defined as the process to determine the position and the geometrical properties of the targets. The steepness of the focus of the system controls the resolution of a GPR image. Resolution is the ability to distinguish between two closed signals or two targets with similar ranges. It is achieved while GPR is mapping. GPR has two types of resolution. These are lateral resolution and range resolution. The two types of GPR resolution is shown in Figure 3.5.

#### 3.6.6.1 Lateral Resolution

The lateral resolution is also called angular or sideways displacement resolution. It is the resolution in the cross range direction. The lateral resolution length is defined as

$$\Delta l \geq \sqrt{\frac{vrW}{2}} \quad (3.16)$$

where

$r$  = distance to the target,  $W$  = pulse width and  $v$  = propagation velocity.

As seen from Equation 3.16, the lateral resolution depends on the distance, pulse width and the velocity. If the distance is increased, the lateral resolution length increases too. The pulse width of the signals are related to the bandwidth ( $B$ ), the center frequency ( $f_c$ ) and the center frequency wavelength ( $\lambda_c$ ) [17]. This relationship can be understood from

$$W = \frac{1}{B} = \frac{1}{f_c} \quad (3.17)$$

The center frequency wavelength is equal to

$$\lambda_c = \frac{f_c}{v} \quad (3.18)$$

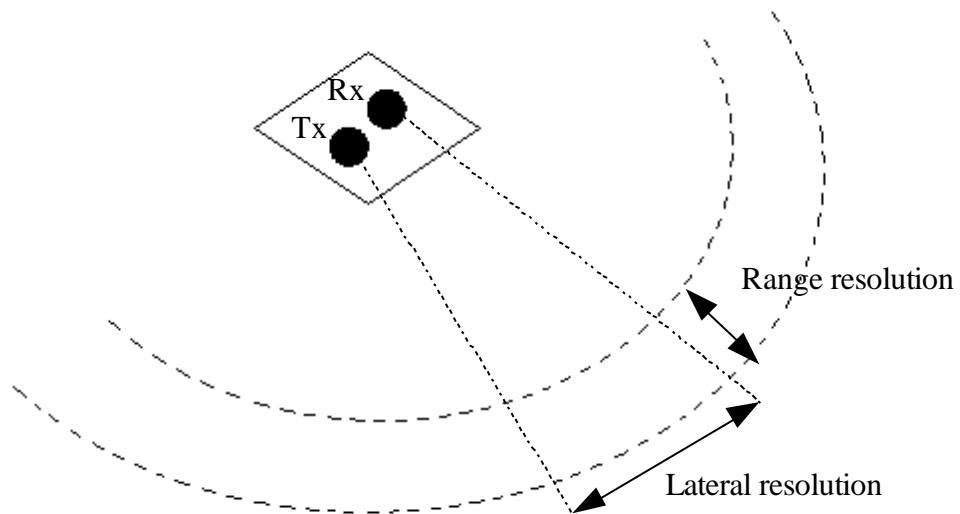


Figure 3.5: The types of GPR resolution: lateral and range resolution

### 3.6.6.2 Range Resolution

The range resolution is also called longitudinal or depth resolution. Range resolution is defined as the ability of radar to resolve between two closely spaced targets. It is written as

$$R_{res} = \frac{1.39c}{2B\sqrt{\epsilon_r}} \quad (3.19)$$

where

$c$  = the speed of light,  $B$  = the bandwidth and  $\epsilon_r$  = relative permittivity.

The range resolution length is also defined as

$$\Delta r \geq \frac{Wv}{4} \quad (3.20)$$

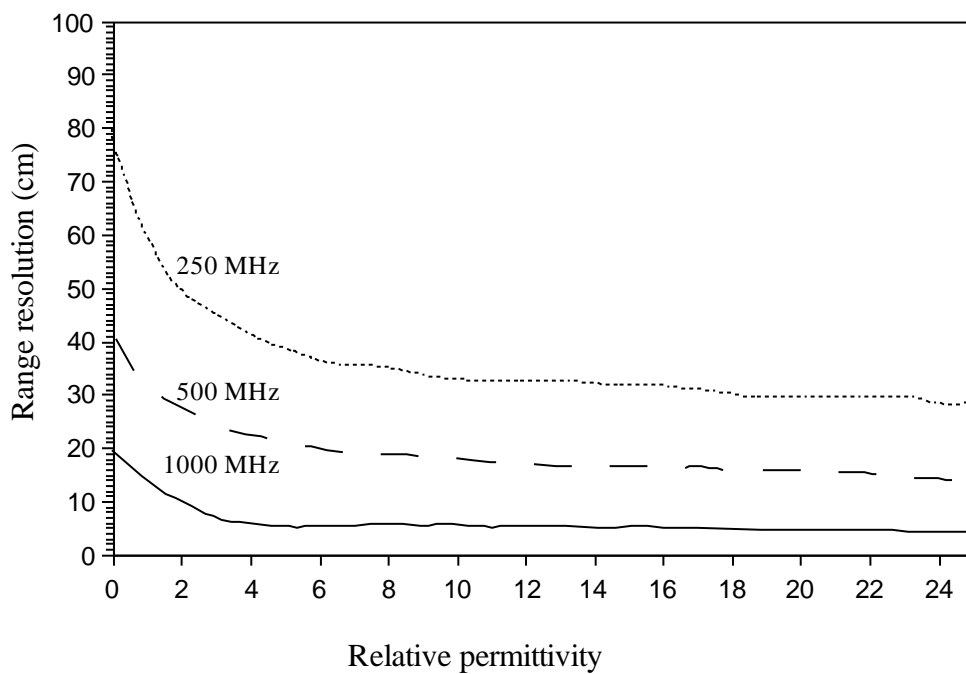


Figure 3.6: Range resolution versus relative permittivity for different bandwidths [17]

As seen from the Equation 3.20, the range resolution length depends on the pulse width and the velocity. However, pulse dispersion and attenuation affects range resolution at longer distances. As seen from the Equation 3.19, the range resolution depends on the speed of light, bandwidth and the relative permittivity [17]. If the bandwidth is increased, the range resolution decreases. The relationship between range resolution and relative permittivity for different bandwidths is shown in Figure 3.6.

### 3.6.7 Propagation Velocity and Depth

Although the propagation velocity of EM waves is taken as  $3 \times 10^8 \text{ ms}^{-1}$  in free space, the value of this velocity is cut down on in a dielectric medium. By finding the velocity, the target depth and thickness can be determined. The propagation velocity can be determined from Equation 3.12. This is only valid for isotropic and homogeneous materials. Using the propagation velocity and the transmit time the depth of the target can be determined. The depth is determined from

$$d = v \frac{t_r}{2} \quad (3.21)$$

where

$t_r$  = the transmit time to and from the target.

Most of the experimental studies are performed without knowing the permittivity. At those times the propagation velocity is determined by either measuring the value of the depth or making many measurements.

When the permittivity is increased, the propagation velocity decreases. This decrease also affects the wavelength within the material to decrease too. This relationship among the velocity, wavelength and frequency of an EM wave can be understood from

$$\lambda_m = \frac{v}{f} \quad (3.22)$$

where

$\lambda_m$  = the wavelength within the material.

CMP method is used in GPR to determine the propagation velocity of environments. Transillumination mode is used to measure velocities inside rock bodies or objects. Any dielectric discontinuity will cause a reflection. The higher the relative permittivities' difference, the more intense the buried object will get.

Typical pulses have a width of a nanosecond or less. This belongs to frequency spectrum of hundreds of MHz to 1-2 GHz. In order to achieve a good resolution, high frequencies are needed. However the penetration depth of the electric fields is inversely proportional to the frequency [1], [19], [26].

### 3.6.8 Selecting Antenna Separation

Most GPR systems use dipole antennas in bistatic arrangement. Changing the antenna spacing can help to optimize the system for definite types of target detection. The purpose is to minimize cross-coupling and clutter so that only the reflected wave from the buried object is obtained. In a bistatic antenna configuration, cross-coupling is the signal that travels from the transmitting antenna to the receiving antenna. The cross-coupling configuration is shown in Figure 3.7.

In order to achieve this purpose, the transmitting and the receiving antennas should be placed in a way that the peak which focuses refraction directs to the common depth to be researched. The optimum antenna separation estimation is given as

$$S = \frac{2d}{\sqrt{\epsilon_r - 1}} \quad (3.23)$$

Increasing the antenna separation causes the reflectivity to increase and depth resolution to decrease. Small antenna spacing is preferred generally for simplicity [24], [27].

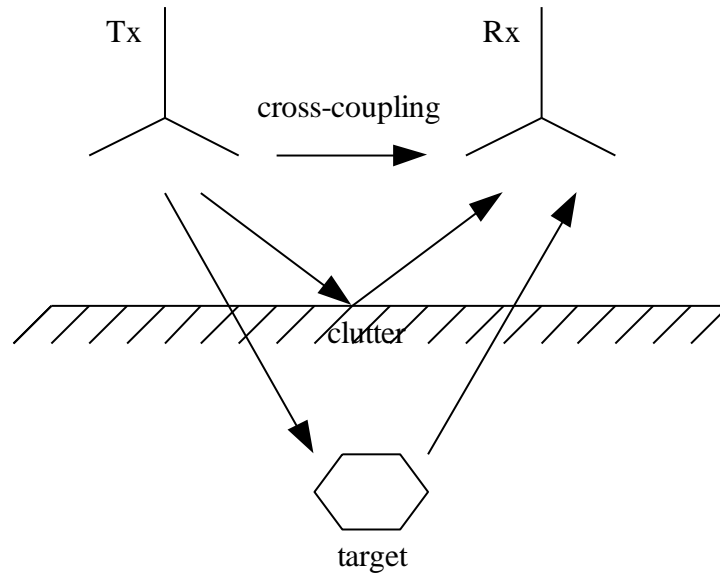


Figure 3.7: The illustration of cross-coupling, clutter and reflected wave from the buried object

### 3.6.9 Antenna Gain and Antenna Radiation Pattern

Gain is defined as measuring the antenna's capability to concentrate the transmitted energy in a particular direction. It is expressed in dB. There are two types of antenna gains. These are directive gain and power gain. The directive gain is also called as directivity. It is defined as the maximum radiation intensity in a direction relative to the average intensity of an isotropic radiator and it is mostly used in antenna radiation patterns and antenna engineering [28]. The directivity can be determined from

$$G_D = \frac{P_{max}}{P_t / 4\pi R^2} \quad (3.24)$$

where

$P_{max}$  = maximum radiated power,  $P_t$  = total radiated power and  $R$  = distance from antenna to the point of observation.

The Equation 3.24 shows that the directivity can be determined from radiation pattern of an antenna.

The power gain is closely related to the directivity of an antenna. One small difference is that it includes dissipative losses. The power gain is defined as the ratio of maximum radiation intensity to the intensity of a lossless isotropic radiator with equal power input and it is mostly used in radar range equations and radar engineering. The power gain can be determined from

$$G = \frac{P_{max}}{P_o/4\pi R^2} \quad (3.25)$$

where

$P_o$  = total accepted power.

The power gain is used more often in radar equations because it includes dissipative losses. The directivity is related to the antenna beamwidth. The relation between the directivity and the power gain is as follows

$$G = \rho_r G_D \quad (3.26)$$

where

$\rho_r$  = radiation efficiency.

Both of the gains are the same in terms of transmitting or receiving antenna. A radiation pattern of an antenna shows how much an antenna radiates on each direction. It shows the gain of the antenna versus angle. The radiation patterns show gain and beamwidth values for main lobe, side lobes and back lobe of the antenna. The strength of the radiated field and the polarization properties of the antenna are also understood by looking at these patterns [28].

### **3.6.10 Clutter**

“The clutter that affects a GPR is defined as those signals that are unrelated to the target scattering characteristics but occur in the same sample time window and have similar spectral characteristics to the target wavelet” [1].

Transmitting and receiving many signals at the same time and having many reflections between antenna and surface cause the clutter to take place. As the time increases, clutter decreases. The effect of the clutter can be understood more clearly in short ranges.

Clutter depends on the antenna type, arrangement and parallel planar dipole arrangement. In parallel planar dipole arrangement, breakthrough level is most constant. So the antennas need to be carefully chosen and arranged to reduce the effects of clutter [19].

There are several techniques that help to reduce the effect of clutter and these techniques continue to improve as the time passes.

### **3.6.11 Losses**

When the signal propagates from transmitting antenna to receiving antenna, it encounters various losses. These losses are realized when they are detected by the receiving antenna. The total loss detected at the receiver is the summation of some losses in dB. These losses are antenna efficiency loss, antenna mismatch loss, transmission loss, retransmission loss, antenna spreading loss, target scattering loss and attenuation loss of material [1].

The antenna efficiency loss is a measure of the power loss from the available power for radiation which is applied to the antenna terminals. The efficiency is low in resistively loaded antennas. The antenna mismatch loss shows the similarity between the antenna and the transmitter. The transmission loss shows the losses from air to material and the retransmission loss shows losses from material to air. The antenna

spreading loss shows the losses of the power when the wave propagates anywhere away from the antenna. The more distance wave travels, the more power the wave loses. The attenuation loss of a material shows the losses or signal weakening due to the material types of the medium. This subject is explained in more detail in Section 3.2.4.3 before.

The target scattering loss shows the losses due to the physical properties of targets. When the target has small dimensions, the target scattering loss increases and the returned signal gets smaller. If there is resonance in targets, the target scattering loss decreases and the returned signal gets larger. The targets with higher permittivity than the surrounding material produce a stronger radar return. A stronger radar return means that the returned signal is larger and the scattering loss is lower. So the scattering cross-section also depends on properties of the surrounding medium [1].

### **3.7 Typical GPR Assumptions**

Although EM waves are 3D, they are considered as 2D in most of the times except propagating through anisotropic materials.

The experimental studies related to GPR are generally performed with EM waves whose transmitted frequencies are greater than the materials transition frequency. The result of this is propagation and reflection of the EM waves. The assumption is only valid in materials whose permeability is low.

Most of the materials are considered as dielectric and lossless in GPR studies. These conditions allow the EM waves to propagate and oscillate.

Even if some of the assumptions mentioned above are optional, they need to be taken into account in every GPR study. These should be performed during the study including the times before and after the study [2].

### **3.8 The Advantages and the Drawbacks of GPR**

The advantages of GPR are as follows. The antennas of GPR do not need to touch the surface during the experiment. The antennas' properties are designed to be adequate. Those properties include the bandwidth and the beam shape. Many impulses can be produced by signal sources. Any dielectric discontinuity is detected by GPR. It can detect the given target and produce the three dimensional image of the target.

The signal attenuation needs to be considered during the experiment. Materials with high conductivity have low frequency and large signal attenuation.

The success of GPR lies on the fact that the requirements below should be met [1]:

- a) There should be efficient coupling of EM radiation in the ground.
- b) There should be adequate penetration of the radiation. The target depth needs to be considered to determine the penetration of the radiation.
- c) A large scattered signal should be obtained from the discontinuities. This helps to investigate the subsurfaces easily.
- d) There should be adequate bandwidth of the detected signal. The resolution and noise levels need to be considered to determine the bandwidth of the detected signal.

The requirements that are mentioned above are the most significant ones. These requirements help us to understand why GPR is a successful and an efficient method.

The disadvantages of GPR are as follows. The size of the antenna is too large and heavy to carry. This is due to the fact that it comprises of wide band antennas and complex structures which are difficult to produce [1].

## CHAPTER 4

# DETERMINATION OF THE SCATTERED ELECTRIC FIELDS

### 4.1 Introduction

The total scattered electric field due to cylinder and interface is obtained mathematically in this chapter. It is also equal to the total scattered electric field above the interface or the electric field distribution at the OFS or the electric field strength at the OFS.

### 4.2 The Configuration

A cylinder is deeply buried in a dielectric half-space. The depth from the dielectric interface to the center of the cylinder is  $b$ . The circular cylinder has a radius of  $a$ . The cylinder propagating on  $y$  axis has an infinite size and it is perfectly conducting. A line source is placed at point  $B$ . This configuration is shown in Figure 4.1.

$\epsilon_1$  is the relative permittivity of medium 1 and  $\epsilon_2$  is the relative permittivity of medium 2.

The total scattered electric field above the dielectric interface needs to be determined [29]. There is a line source and a unit amplitude plane wave coming from this source is perpendicularly polarized. When a wave is sent from the source, the wave will

propagate either in medium 1 or medium 2. Part of the wave that is propagating in medium 1 direction will make reflection at the interface. However the other part of the wave that is propagating in medium 2 direction will make refraction and after there will also be some scattering from the circular cylinder.

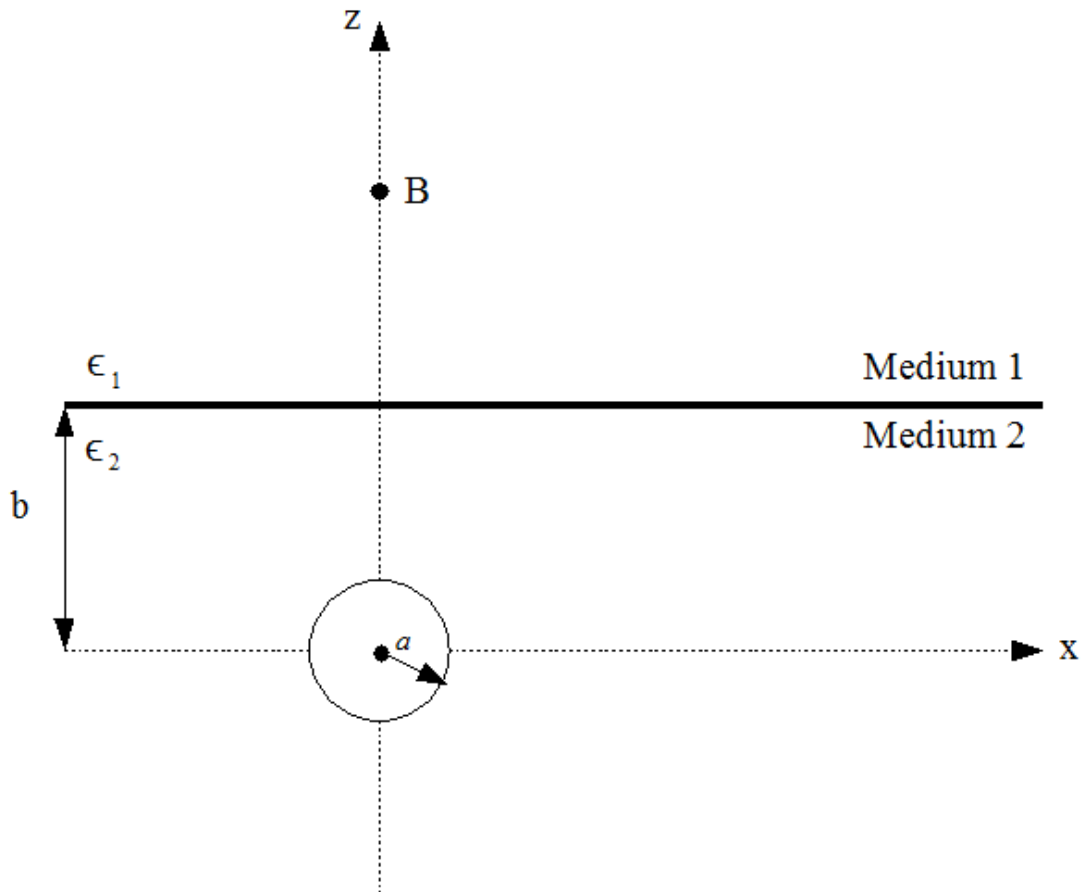


Figure 4.1: The configuration of the scattering problem

The total scattered electric field above the dielectric interface is the summation of the reflected electric field from the dielectric interface and the scattered electric field from buried cylinder above the interface between two media. The geometry is shown in Figure 4.2.

The total scattered electric field above the dielectric interface is

$$E_{total} = E_{surface\_ref} + E_{scattered} \quad (4.1)$$

where

$E_{surface\_ref}$  = the reflected electric field from the dielectric interface and  
 $E_{scattered}$  = the scattered electric field from buried cylinder above the interface between two media.

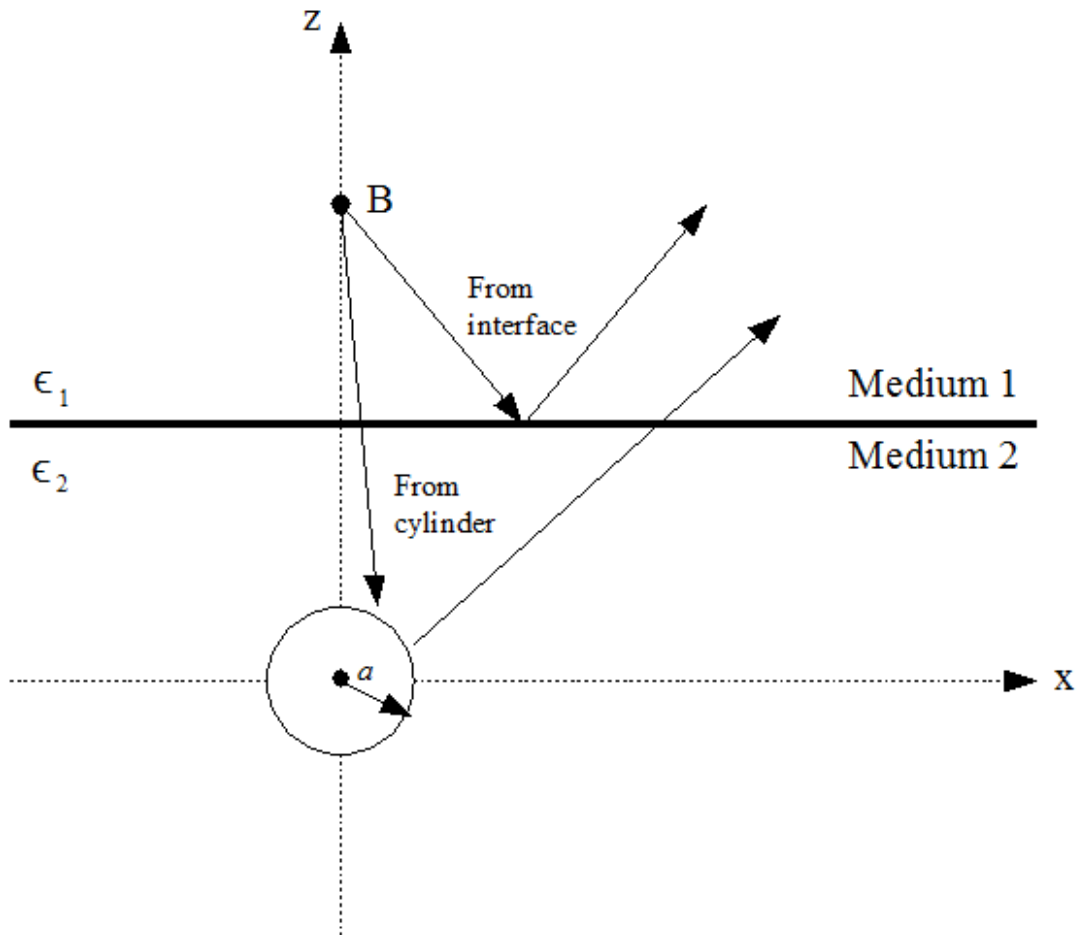


Figure 4.2: The geometry of the total scattered electric field above the dielectric interface

### 4.3 The Scattered Electric Fields

#### 4.3.1 The Reflected Electric Field from the Dielectric Interface

When working in transverse electric (TE) mode, the magnetic field on the propagating direction is zero and the electric field on the propagating direction is different from zero. The reflected electric field from the dielectric interface needs to be determined.

A field coming from medium 1 is a plane wave whose electric field is given as

$$E_i = \exp \{-ik_1(z - b)\} \quad (4.2)$$

where

$k_1$  = propagation constant of medium 1.

The incident field sent from the line source will make a reflection at the dielectric surface. Then the reflected electric field from the dielectric interface is written as

$$E_{surface\_ref} = \frac{(n-1)}{(n+1)} \exp \{-ik_1(z - b)\} \quad (4.3)$$

where

$n$  = the relative index of refraction or the index of refraction.

#### 4.3.2 The Scattered Electric Field from the Buried Cylinder

In order to determine  $E_{total}$ ,  $E_{scattered}$  needs to be determined first.

Induced currents are used to calculate the scattered electric field from buried cylinder. By integrating the Green's function over the induced current distribution, the scattered electric field can be determined. In order to overcome the difficulty of finding the induced current distribution, an approximation is used [29]. It states that

the cylinder is so deeply buried that the scattered fields due to initial induced currents have no interaction with the buried cylinder.

The incident field is given by Equation 4.2. The field transmitted in medium 2 is given as

$$E_t = T_{12} \exp(-ik_2 z) \quad (4.4)$$

where

$k_2$  = propagation constant of medium 2 and  $T_{12}$  = the Fresnel transmission coefficient which is given as

$$T_{12} = \frac{2k_1}{k_1 + k_2} \exp(ik_2 b) \quad (4.5)$$

The transmitted field from medium 1 to medium 2 is given by Equation 4.4. It is converted into cylindrical coordinates [29]. The transmitted field is then written as

$$E_t = T_{12} \sum_{n=-\infty}^{n=\infty} (-1)^n J_n(k_2 \rho) \exp(in\varphi) \quad (4.6)$$

where

$J_n(k_2 \rho)$  = the Bessel function.

When the transmitted wave hits the circular cylinder, the wave scatters due to the cylinder. Then the scattered field can be written as

$$E_s = \sum_{n=-\infty}^{n=\infty} -\frac{(-1)^n T_{12} J_n(k_2 a)}{H_n^{(1)}(k_2 a)} H_n^{(1)}(k_2 \rho) \exp(in\varphi) \quad (4.7)$$

where

$H_n^{(1)}(k_2 a)$  and  $H_n^{(1)}(k_2 \rho)$  = first order Hankel functions.

The total tangential magnetic field can be determined from Maxwell's equations which can be written as

$$H_{\phi total} = \frac{i}{\omega \mu} \frac{\partial E_{total 2}}{\partial \rho} \quad (4.8)$$

where

$\omega$  = angular frequency,  $\mu$  = permeability and  $E_{total 2}$  = total electric field in medium 2.

The total electric field in medium 2 is equal to

$$E_{total 2} = E_s + E_t \quad (4.9)$$

Using the relationship between the total tangential magnetic field and the surface current density, the surface current density on perfect conductor is calculated as

$$J_s(a, \varphi) = \frac{2T_{12}}{\pi \omega \mu a} \sum_{n=-\infty}^{n=\infty} (-1)^n \frac{\exp(in\varphi)}{H_n^{(1)}(k_2 a)} \quad (4.10)$$

In order to find the scattered electric field from buried cylinder above the interface, first of all the scattered field for each element on conducting cylinder needs to be calculated. Then they need to be summed over all elements of surface current [29].

The total scattered electric field from conducting cylinder above the interface is then written as

$$E_{scattered} = a \int_0^{2\pi} J_s(a, \varphi') G_e(\rho, \varphi; a, \varphi') d\varphi' \quad (4.11)$$

where

$G_e(\rho, \varphi; a, \varphi')$  = the Green's function. It is equal to

$$G_e(\rho, \varphi; a, \varphi') = \begin{cases} G_{e1}(\rho, \varphi; a, \varphi'), & y \geq b \\ G_{e2}(\rho, \varphi; a, \varphi'), & y \leq 0 \end{cases} \quad (4.12)$$

It is also known that

$$\varphi_o = \tan^{-1} \sqrt{\left(\frac{k_2}{k_1 \cos \varphi}\right)^2 - 1} \quad (4.13)$$

Putting in the values of Green's function and surface current density from Equations 4.10, 4.12 and 4.13 to Equation 4.11. After making some simplifications the Equation 4.11 is obtained as

$$\begin{aligned} E_{scattered} &= \frac{-8k_1^2}{\sqrt{2\pi}(k_1^2 - k_2^2)(k_1 + k_2)} \\ &\times \exp(ik_2b - ik_1b \sin \varphi + ib\sqrt{k_2^2 - k_1^2 \cos^2 \varphi}) \\ &\times \left\{ k_1 \sin^2 \varphi - \sin \varphi \sqrt{k_2^2 - k_1^2 \cos^2 \varphi} \right\} \sum_{n=-\infty}^{n=\infty} \left\{ \frac{(i)^n J_n(k_2 a) \exp(in\varphi_o)}{H_n^{(1)}(k_2 a)} \right\} \\ &\times \frac{\exp(ik_1\rho - i\pi/4)}{\sqrt{k_1\rho}}, \quad 0 \leq \varphi \leq \pi \end{aligned} \quad (4.14)$$

The above expression is the scattered electric field from buried cylinder above the interface and it looks complicated. After making some changes, Equation 4.14 can be understood more clearly. The Equation 4.14 can be rewritten as

$$E_{scattered} = PQSWTUV \quad (4.15)$$

where

$$P = \frac{2}{1+n} \quad (4.16)$$

$$Q = \exp(ik_2b) \quad (4.17)$$

$$S = -\sqrt{\frac{2}{\pi}} \exp\left(-i\frac{\pi}{4}\right) \sum_{m=-\infty}^{\infty} (i)^m \frac{J_m(k_2a)}{H_m^{(1)}(k_2a)} \exp\left\{im\left(\frac{\pi}{2} - \varphi_2\right)\right\} \quad (4.18)$$

$$W = \frac{\cos \varphi_1}{n \cos \varphi_2} \quad (4.19)$$

$$T = \frac{2n \cos \varphi_2}{\cos \varphi_1 + n \cos \varphi_2} \quad (4.20)$$

$$U = \exp\{ik_1b(n \cos \varphi_2 - \cos \varphi_1)\} \quad (4.21)$$

$$V = \frac{\exp(ik_1\rho)}{\sqrt{k_1\rho}} \quad (4.22)$$

In the above formulas the relative index of refraction is defined as  $n = k_2/k_1$ .  $\varphi_1$  is the angle of refraction and  $\varphi_2$  is the angle of incidence. These are defined from medium 2 to medium 1. The relationship between the angles can be seen from

$$\varphi_1 = \frac{\pi}{2} - \varphi \quad \varphi_2 = \sin^{-1}\left(\frac{\sin \varphi_1}{n}\right) \quad 0 \leq \varphi \leq \pi \quad (4.23)$$

The ray diagram of the scattered electric fields propagating from the circular cylinder to and above the interface is shown in Figure 4.3. The relationship between the angles can be understood from this figure.

An incident TE wave has unit amplitude. When a wave is sent from medium 1 to medium 2, the wave is excited with amplitude given by  $P$ .  $P$  shows the Fresnel transmission coefficient [29]. When the wave propagates through the cylinder, it

encounters a phase change given by  $Q$ .  $Q$  shows the phase change  $ik_2b$  and  $S$  shows the angular distribution of the field scattered from buried cylinder. The amplitude of the scattered field in medium 2 is  $PQS$ . The scattered field coming from medium 2 is refracted at the interface. After making refraction, it propagates through medium 1 again [29].

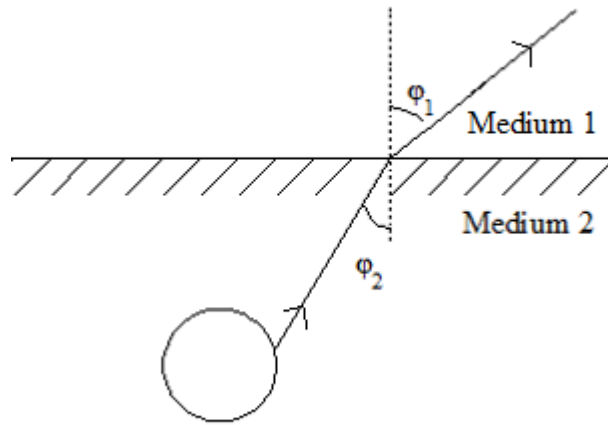


Figure 4.3: The ray diagram of the scattered electric fields from cylinder for above the interface

### 4.3.3 The Total Scattered Electric Field above the Dielectric Interface

As it is mentioned before,  $E_{surface\_ref}$  and  $E_{scattered}$  are needed to determine  $E_{total}$ . They are obtained in Equations 4.14 and 4.3.

From Equation 4.1, it is seen that  $E_{total} = E_{surface\_ref} + E_{scattered}$ .

Writing Equations 4.3 and 4.14 into the above equation, the total scattered electric field above the dielectric interface or the electric field distribution at the OFS can be obtained as

$$\begin{aligned}
E_{total} &= \frac{(n-1)}{(n+1)} \exp\{-ik_1(z-b)\} \\
&+ \frac{-8k_1^2}{\sqrt{2\pi}(k_1^2 - k_2^2)(k_1 + k_2)} \exp(ik_2b - ik_1b \sin \varphi + ib\sqrt{k_2^2 - k_1^2 \cos^2 \varphi}) \\
&\times \left\{ k_1 \sin^2 \varphi - \sin \varphi \sqrt{k_2^2 - k_1^2 \cos^2 \varphi} \right\} \sum_{n=-\infty}^{n=\infty} \left\{ \frac{(i)^n J_n(k_2 a) \exp(in\varphi_o)}{H_n^{(1)}(k_2 a)} \right\} \\
&\times \frac{\exp(ik_1\rho - i\pi/4)}{\sqrt{k_1\rho}}
\end{aligned} \tag{4.24}$$

The total scattered electric field due to cylinder and interface is obtained mathematically in this chapter. It is also equal to the total scattered electric field above the interface or the electric field distribution at the OFS or the electric field strength at the OFS. These formulas are modeled and run in the MATLAB and OPTIWAVE package programs in order to simulate the working of the proposed system of this thesis study.

## **CHAPTER 5**

# **GENERAL REVIEW OF OPTICAL FIBER SENSOR (OFS)**

### **5.1 Introduction**

A sensor is a measuring device which converts the measured quantity into a readable form. This form is observed either by humans or objects. Sensors are used in many applications that some of which people are aware of and some of which they are not.

Optical fiber sensors (OFS) are measuring devices that convert optical signals to electrical signals. This is performed by means of an optoelectronic transducer [30]. OFSs play an important role in people's lives. Those include many applications where distance, EM compatibility and risk of explosion limit the usage of other technologies other than optical fibers. The technology related to optical fibers has improved lately and it will continue to improve as the time passes.

The signal passing through fiber is modulated while communicating and the fiber acts as a modulator while sensing. It converts measured quantities into a change in optical radiation by means of an optoelectronic transducer. Light is described by amplitude, phase, frequency and polarization of the signal. Although all or some of those values can pass through a change, the operating of the OFSs depend on only the magnitude of the change and the capability of the measurement [31], [32].

## 5.2 Basic Information

Like all the communication systems, an optical communication system comprises of a transmitter, a communication channel and a receiver. The basic optical communication system block diagram is shown in Figure 5.1 below.

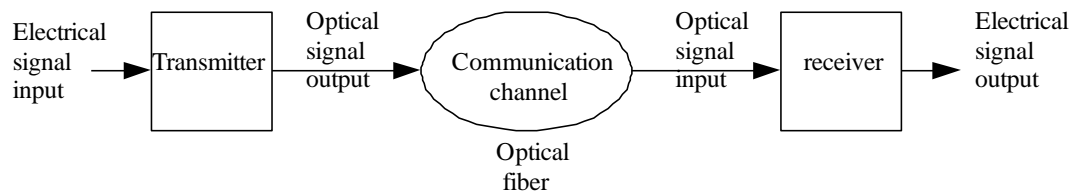


Figure 5.1: The basic optical communication system block diagram

Optical transmitters convert the electrical signal into optical signal form. This optical signal is sent to the communication channel which is the optical fiber. The optical transmitter comprises of an optical source, an electrical pulse generator and an optical modulator. Communication channel takes the optical signal from the transmitter and sends it to the receiver without distorting it. Optical fiber is used in most of the light systems because it has a small amount of power loss. Optical receivers convert the optical signal coming from the communication channel back into electrical signal. It comprises of a photodetector, an amplifier and a demodulator. As a result, the electrical signal is converted into optical signal at the optical transmitter and after passing through an optical fiber channel the optical signal is then converted back into the electrical signal at the optical receiver.

The optical communication system block diagram shown in Figure 5.1 can be modified using OFS. The modified block diagram is shown in Figure 5.2.



Figure 5.2: The OFS interrogation system block diagram

The name OFS interrogation system (OFSIS) can be used instead of optical communication system. Interrogation is transmitting a signal for starting an appropriate response and its main goal is to obtain information. A transmitter sends a signal which triggers transponder and transponder sends a reply to the transmitter. The output is then obtained. This process is called as interrogation process. Transponder is an element that sends and receives optical signal from fiber [3].

As shown in Figure 5.2 an OFSIS comprises of a light source (laser as a transmitter), an optical fiber sensor and a photodetector (as a receiver). OFS is included in this system. OFS comprises of an optical modulator and an electric field probe. More explanation is given about the system in one page before. The optoelectronic device can also include a subsystem for generating, detecting, processing and conditioning the signal. After those processes, a reproduction of the input signal is obtained. So the electrical signal is converted back into the electrical signal. The transmitted signal can be modulated by amplitude, phase, frequency or polarization characteristics [3].

### 5.3 OFS Types

There are many types of OFSs and they can be categorized as follows:

- a) They can be categorized as extrinsic or intrinsic sensors. In an extrinsic sensor, the fiber acts as a two way communication tool for transmission of light to sensing part. Sensing occurs in an external optical device which is away from the fiber. Modulation processes also take place outside the optical waveguide. There are some advantages of extrinsic sensors [3], [31], [32].

They have the ability to reach inaccessible places and they act as a shield to reduce the effect of noise in signal measurements. The acceleration, velocity, displacement and rotation are measured using extrinsic sensors.

In an intrinsic sensor, sensing occurs inside the fiber. Modulation processes also take place inside the optical waveguide. All or some of the physical properties can pass through a change. These are amplitude, phase, frequency and polarization of the signal. There are some advantages of intrinsic sensors. They have the ability to sense over very large distances and they make very accurate measurements [3], [31], [32].

- b) They can be categorized based on the modulation and demodulation process. Based on this categorization a sensor is then called an amplitude (intensity), a phase, a frequency or a polarization sensor. All of these four properties are named as an interferometric sensor. This sensor uses interferometric techniques for detection and the technique comprises of heterodyne (coherent) detection. Because of the fact that intensity sensors are incoherent, they are also called incoherent sensors. They have a simple design whereas interferometric sensors have a complex one. Although the interferometric sensors are complex, they result in a better resolution and sensitivity.
- c) They can be categorized based on their applications. Some of these applications are physical sensors, biomedical sensors, thermal sensors, chemical sensors, mechanical sensors, electromagnetic sensors and much more. The applications comprise of intensity and interferometric types of sensors [3], [31], [32].

## **5.4 Basic Components of an OFS Interrogation System**

An OFS interrogation system comprises of a light source, modulation, communication channel which is optical fiber, a photodetector, demodulation, processing, display and other electronics needed. OFS can also be included in this system which is shown in Figure 5.2. Those are explained in more detail in Section 5.2.

## 5.4.1 Optical Fibers

### 5.4.1.1 Light Propagation in an Optical Fiber

An optical fiber is a long, thin, cylindrical dielectric waveguide. The light propagates along the fiber using total internal reflection process. The propagation of light in an optical fiber and the principle of the optical fiber are shown in Figure 5.3 below.

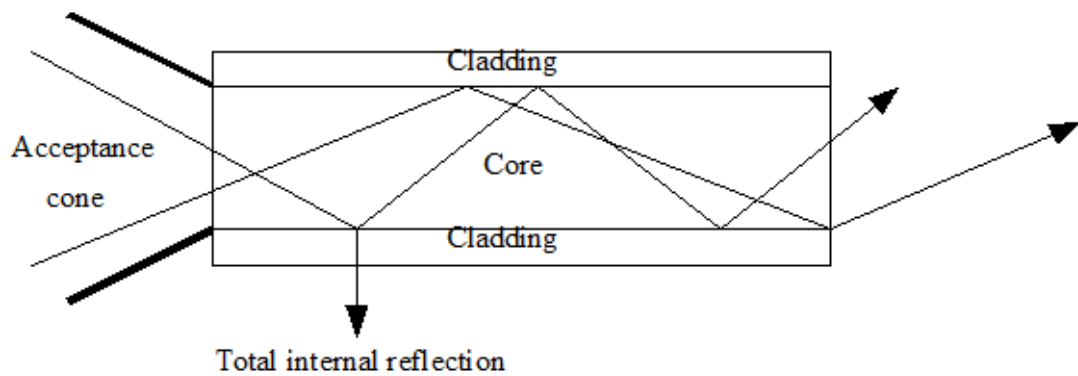


Figure 5.3: The propagation of light in an optical fiber and the principle of the optical fiber

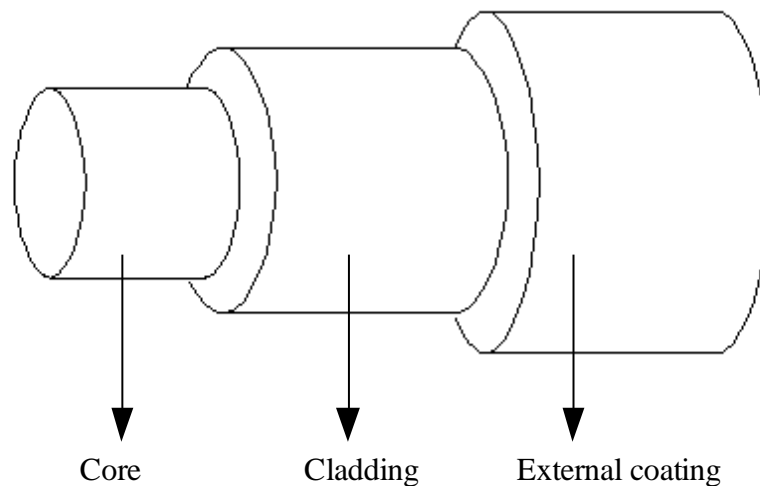


Figure 5.4: The geometrical structure of an optical fiber

An optical fiber basically has three parts: core, cladding and external coating. The geometrical structure of an optical fiber is shown in Figure 5.4.

Core is the inner region and light wave propagation occurs here. Core is surrounded by a thin dielectric layer which is the cladding. Core is denser than cladding and the index of refraction of core ( $n_j$ ) needs to be greater than the index of refraction of cladding ( $n_p$ ) for total internal reflection to store and let the optical signal continue propagating in the core. Cladding is surrounded by the external coating which is the outer layer. External coating insulates and protects the fiber from the medium. External coating comprises of two layers. The inner layer is soft and flexible while the outer layer is hard and it is not flexible. In low to medium loss fibers the core is made up of silica glass and the cladding is made up of silica glass or plastic. In high loss fibers both the core and the cladding are made up of plastic [30], [31], [32].

It is important to have a minimum amount or no loss during propagation. This can be achieved by accomplishing the requirements for total internal reflection. The requirements are accomplished when the angle of incidence is greater than the critical angle. For total internal reflection on the interface between the core and coating, the critical angle is found from

$$\sin\varphi_c = \frac{n_p}{n_j} \quad (5.1)$$

The light propagating in the fiber makes a reflection at the walls of the fibers and this continues until the signal goes away from the fiber.

#### **5.4.1.2 Fiber Types**

There are two types of fibers that are used commonly in optical fiber sensors. First type is the step index fiber. It has a core diameter of 50  $\mu m$  or larger and cladding diameter of 125  $\mu m$ . The index of refraction of core and cladding are fixed in this type of fiber. The rays of light are directed along the core by total internal reflection and they are reflected at the core cladding interface [31], [32]. Rays that hit the

interface with high incoming angle are reflected. Conversely, rays that hit the interface with low incoming angle are refracted.

By taking the difference of index of refraction of core and cladding, the minimum angle for total internal reflection is determined. The minimum angle helps to determine the acceptance angle or the numerical aperture. Numerical aperture is determined from

$$NA = \sqrt{(n_j^2 - n_p^2)} \quad (5.2)$$

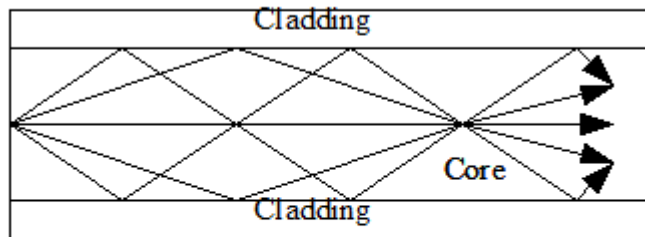
If the numerical aperture increases, it is easier to combine the transmitter or the receiver to the fiber. The increase in numerical aperture leads the signal to scatter more than normal. As a result, more dispersion takes place. The light propagation in the step index fiber is shown in Figure 5.5.a.

Second type is the graded index fiber. It has a core diameter of  $50 \mu m$  or larger and cladding diameter of  $125 \mu m$ . The index of refraction of core is variable and the index of refraction of cladding is fixed in this type of fiber. The index of refraction decreases when the ray propagates through core layer. This leads the rays to bend when approaching the cladding. The increase in bended rays leads the signal to scatter less than normal. As a result, less dispersion takes place. The graded index fibers have larger bandwidths, less number of modes and larger data rate capabilities than the step index fibers [31], [32]. The light propagation in the graded index fiber is shown in Figure 5.5.b.

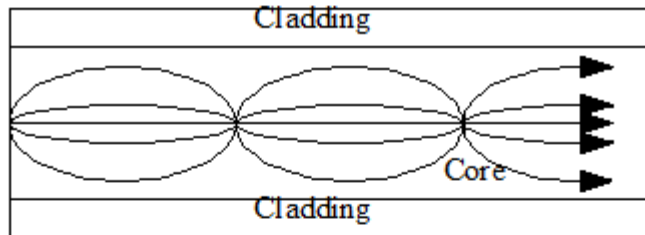
Both the step and the graded index fibers can be divided into classes of single and multi modes. Fibers can support one or more modes. Modes are defined as the set of guided EM waves. Fiber which supports one mode is defined as single-mode fiber. The mode of the fiber depends on the wavelength of the light. It can be seen that the single-mode fiber supports small number of modes which is one. In most of the fibers, the light energy in the fiber is not totally stored in the core [31], [32], [33]. In single-mode fibers most of the light energy is stored in the cladding after refracting

from the interface. The single-mode fiber has a core diameter of 2-10  $\mu\text{m}$  and cladding diameter of 125  $\mu\text{m}$ . The index of refraction of core and cladding are fixed in this type of fiber. The light propagation in the single mode fiber is shown in Figure 5.5.c.

a) The multi-mode step index fiber



b) The multi-mode graded index fiber



c) The single-mode step index fiber

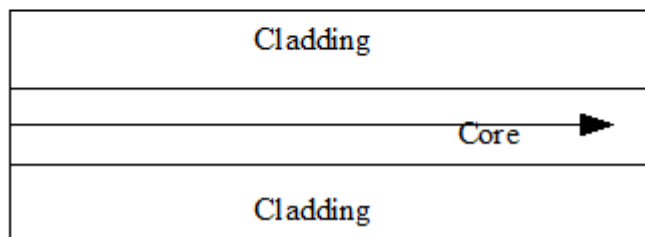


Figure 5.5: The propagation of light in different types of fibers

Fiber which supports more than one mode is defined as multi-mode fiber. The multi-mode fiber has a core diameter of  $50\ \mu\text{m}$  or larger. The index profile of the core is either step index (uniform) or graded (parabolic). It has some advantages when compared to single-mode fiber. Multi-mode fiber uses light emitting diodes (LED) and single-mode fiber uses laser diodes. LEDs have less optical output power and long time usage. They are also less expensive than laser diodes.

A disadvantage of multi-mode fibers is more intermodal dispersion that takes place. When a pulse is sent to the fiber, the pulse spreads through all modes with different velocities. Different modes arrive at the end of the fibers at different times. This case is called as intermodal dispersion. Less dispersion takes place in single-mode fibers [31], [32], [33]. The light propagations in all of the three fiber types are shown in Figure 5.5.

## **5.4.2 Light Sources**

### **5.4.2.1 Semiconductor Sources of Light**

Semiconductor sources of light have many advantages which are power consumption, reliability and cost. Light emitting diodes (LED) are solid light sources. Light is brought forward by electroluminescence. LEDs are made from p-n junction and the junction included in them is forward biased. When the electrons from n-type and holes from p-type combine, photons are produced. This process is called electroluminescence.

LEDs are usually the best light source. They are cheap with incoherent light. Incoherence shows the phase jumps of the signal. The phase changes during propagation of light and no optical cavity exists for wavelength selectivity. They have broad spectral width, spontaneous emission, high reliability and low sensitivity reflected light. They are beneficial in intensity sensors. LEDs are used with multi-mode fibers and they are employed in high speed local area applications where several wavelengths can be transmitted on one fiber [30], [31], [33].

An LED comprises of three semiconductor layers: p-type, active region and n-type. LEDs are manufactured from ternary alloys (Ga, Al and As) for short wavelengths and from quaternary alloys (In, Ga, Al, As) for long wavelengths. The construction of an LED is shown in Figure 5.6 below.

When the electrons and holes combine in the active region, the emission occurs. If p-n combination is a diode which is forward biased, electrons from n-type and holes from p-type move to the active region. Emission occurs in all of the structure of LED.

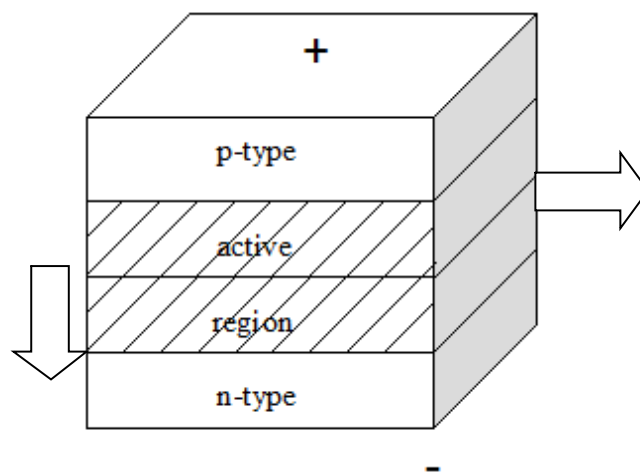


Figure 5.6: Schematics of an LED where arrows show spontaneous emission in all directions

#### 5.4.2.2 Laser Diode (LD)

LDs are made from p-n junction by forming two doped Ga Se layers. The junction included in them is forward biased. Two ends of the structure are parallel and flat. One end is mirrored and the other end's part of is reflective. Longitudinal size is the longer side of the structure's ends whose size changes from  $250 \mu\text{m}$  to  $500 \mu\text{m}$ . It

determines the spectral density of LDs output. The lateral size is the shorter side of the structure's ends whose size changes from  $5\ \mu\text{m}$  to  $15\ \mu\text{m}$ .

LDs are expensive with coherent light. Coherence does not show any phase change. The phase is constant during propagation of light and optical cavity exists for wavelength selectivity. They have narrow line width, stimulated emission, less reliable and high optical output power. They are also less durable to temperature and light changes. LDs are beneficial in interferometric sensors. LDs are used with both single and multi mode fibers. Single mode diode lasers are produced using external cavity schemes [30], [31], [33].

An LD comprises of three layers: p-type, depletion region and n-type. The construction of an LD is shown in Figure 5.7 below. When the electrons and holes combine in the depletion region, emission occurs. Photons are then produced by stimulated emission from a standing wave in the resonator.

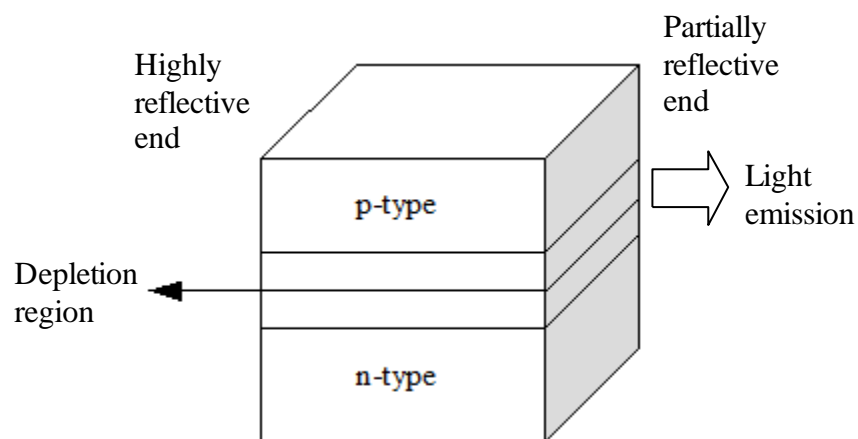


Figure 5.7: Schematics of an LD where arrow shows stimulated emission in one direction

### 5.4.3 Optical Modulators

An electro-optic device helps the electrical and optical signals to communicate with each other. The modulation processes require a single polarization mode and they face up more losses than the other intrinsic optical fiber components. Optical modulators require high frequencies to operate. Electro-optic materials are described as the materials with a voltage-controlled index of refraction because the speed of light varies due to a control voltage [34]. The index of refraction can be written as

$$n = \frac{c_{vacuum}}{c_{material}} \quad (5.3)$$

where

$n$  = index of refraction,  $c_{vacuum}$  = speed of light in vacuum and  $c_{material}$  = speed of light in a material.

An optical modulator is an optical device in which the electro-optic effect is used for modulation of light. An electro-optic effect is described as the variation of the optical properties due to electric field. The change in the optical properties leads a change of the absorption and the index of refraction.

The most important optical modulator parameters are as follows [34]:

- a) The output power is determined by the modulator's insertion loss.
- b) The ratio of the number of 1 bits of the output power to the number of 0 bits of the output power is the extinction ratio. It is described by optical powers.
- c) The modulation speed is characterized by frequency response.

The optical signal produced by the light source needs to be modulated. Mainly there are two modulation schemes: direct optical modulation and external optical modulation.

### 5.4.3.1 Direct Optical Modulation

After a digital modulation current is added to the DC bias current, the direct optical modulation begins. Although the level of the DC bias current should be above the laser threshold current, the current level might be lower than the laser threshold current in low speed cases.

In LEDs the modulator design is flexible and high output power needs to be acquired. The modulation curve is the graph showing variations of the output signal versus the direct currents. In LDs the modulation curve is affected by the temperature and the time passes by. As the time passes and the temperature changes, the curve loses its strength and output power decreases. The loss of the strength also decreases SNR [34].

Direct modulation requires frequencies up to 1 Gbps to operate. Laser frequency chirp and the extinction ratio are the important parameters for direct modulation. Signal degradation is caused by chromatic dispersion which is proportional to laser frequency chirp in scaling. Chirp is defined as the linear change in frequency with time. When there is a change between the modulation current of two logical levels, the frequency chirp occurs. These changes are due to the changes in the carrier densities which affect the index of refraction. The output frequency changes due to the change in the index of refraction. So if the change between the modulation currents is limited, the laser frequency chirp can be minimized. Low laser frequency chirp needs to be obtained to acquire full potential of an optical system.

The ratio of the number of 1 bits of the output power to the number of 0 bits of the output power is the extinction ratio. When there is a large change between the modulation current of two logical levels, the extinction ratio is obtained in a high level. The increase in the ratio causes the SNR to increase. The extinction ratio is limited because the laser should not be turned off at 0 bits. It can be seen that the frequency chirp is contrary to the extinction ratio [3], [34].

### 5.4.3.2 External Optical Modulation

This type of modulation is more complex than direct optical modulation but it provides an increased bit rate and transmission distance. This is achieved using smaller frequency chirp. Laser diode produces a continuous wave (CW) signal and sends it to the external modulator. An intensity modulated optical signal is produced at the output of the modulator so it is called intensity modulation. External optical modulation comprises of some modulation types such as amplitude, phase, frequency and polarization.

There are two types of external modulators that are used more often which are Mach-Zhender (MZ) and electroabsorption (EA). The operating principle of both of the modulators depends on the electro-optic effect. When there is an external electric field, the index of refraction changes. This change leads to electro-optic effect. Lithium Niobate ( $\text{LiNbO}_3$ ), Gallium Arsenide (GaAs) and Indium Phosphate (InP) are some of the adaptive polymers used in electro-optic effect. Among those Lithium Niobate ( $\text{LiNbO}_3$ ) is used more often because of its high electro-optic coefficients and high optical transparency. It is also chemically and mechanically stable and it is compatible in manufacturing [3], [34].

MZ modulator is an integrated optical waveguide that is embedded into a substrate. Among the polymers the substrate is generally made up of Lithium Niobate ( $\text{LiNbO}_3$ ). There are two pairs of electrodes in the waveguide. One is the DC bias electrode and the other one is the radio frequency (RF) electrode. Input is made up of polarization maintained single-mode fiber and output is made up of standard single-mode fiber. MZ modulator requires small waveguide separation for coupling. Directional coupler is difficult to design for high frequency to low speed modulators. The configuration of the MZ modulator is shown in Figure 5.8.

When a CW signal from light source is transmitted, it propagates through both arms of the modulator. They are combined again at the modulator output. Electrical information appears as an amplitude modulation on optical transmission.

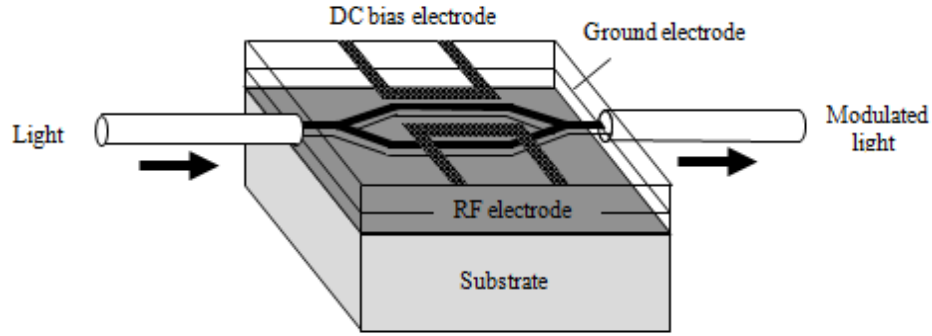


Figure 5.8: The configuration of MZ modulator

As a result the phase lags. The two incoming phases are combined at the modulator output. If the index of refraction values are equal, their amplitudes are added at the output. A high output signal level is produced. If the index of refraction values are different, their amplitudes are subtracted at the output. A low output signal level is produced. Electro-optic coefficient is the parameter that determines how large an effect is observed for an applied voltage. The electro-optic coefficient is determined from

$$V_{\pi} = \lambda d / 2n^3 r_{33} L \Gamma \quad (5.4)$$

where

$V_{\pi}$  = the voltage required to achieve signal transduction,  $r_{33}$  = electro-optic coefficient,  $d$  = distance to the ground electrode,  $n$  = the relative index of refraction,  $L$  = path length and  $\Gamma$  = phase difference.

MZ modulator carries through the sum of the input signal with phase modulated copy of itself. Phase and intensity are modulated as response to a voltage signal [3], [34]. How those are performed is shown in Figure 5.9 where  $E_i(t)$  = input signal,  $E_o(t)$  = output signal,  $V(t)$  = voltage signal and PM = phase modulation.

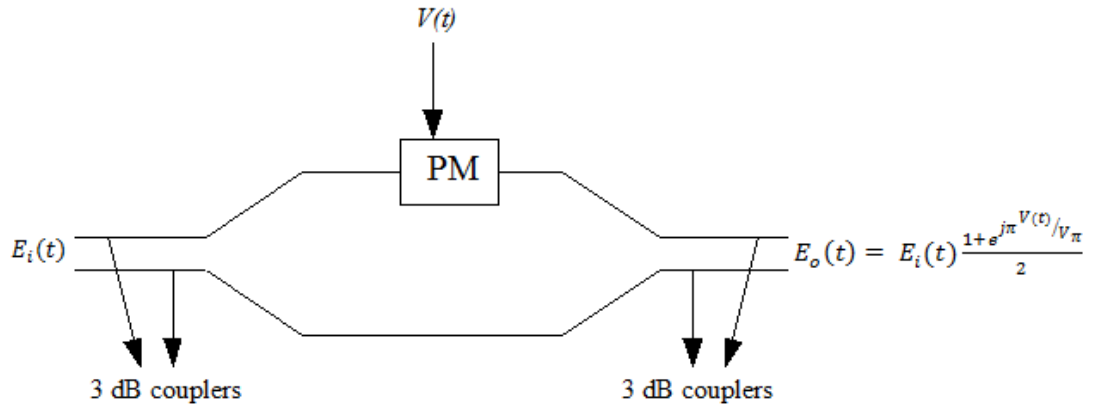


Figure 5.9: The operation of the MZ modulator

EA modulator is a semiconductor waveguide that comprises of several p-type and n-type layers. This type of modulator has similar structure with laser. The design of the EA modulator can either be alone or combining with laser by isolating each of them. Combination of the EA modulator with laser is used more often in high speed communication systems. Due to this combination the insertion losses and the cost of the device are reduced.

The EA modulators are reverse biased. When no bias voltage is applied to the modulator waveguide, the modulator acts as if there is no incoming CW signal. Because of this electron-hole pairs are produced and this causes attenuation of the signal.

When a bias voltage is applied to the modulator waveguide, the voltage separates the electron-hole pairs. Because of this photocurrent is produced. This causes attenuation of the waveguide and signal losses to increase. The highest output signal is obtained when there is no bias voltage applied to the modulator waveguide. The output signal from the EA modulator decreases as the bias voltage increases [3], [34].

EA modulator changes the materials absorption coefficient. The intensity of output light also changes due to a response to a voltage signal. How those are performed is shown in Figure 5.10 below where  $E_i(t)$  = input signal,  $E_o(t)$  = output signal and  $V(t)$  = voltage signal. The extinction ratio value of EA modulators are 10 dB to 13 dB smaller than MZ modulators. EA modulators are stronger than MZ modulators due to the effects of the polarization. The output power of MZ modulators is higher than the output power of EA modulators [3], [34].

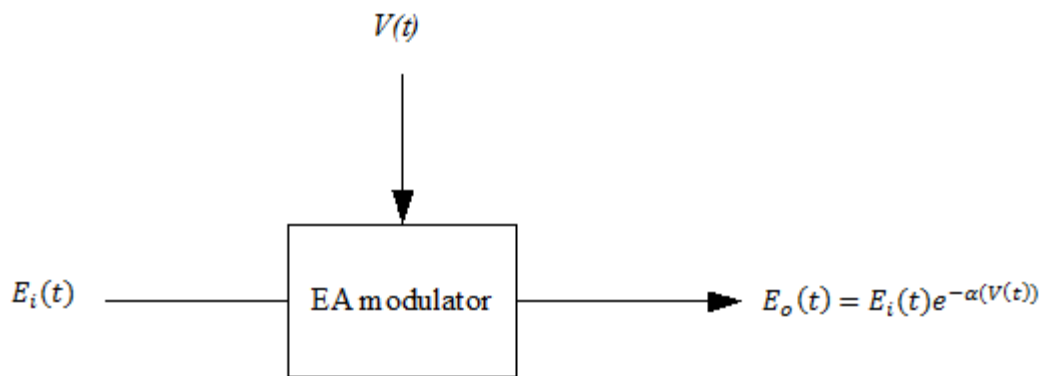


Figure 5.10: The operation of the EA modulator

#### 5.4.4 Light Detectors

There must be a receiving device in a communication system. First element of the receiver is a photodetector which converts the optical signal into electrical signal. A photodetector has basic structure of p-type and n-type of photodiode (PN photodiode) and it can be called as an optical receiver. All the photodetectors operate in reverse bias mode and they also explain the meaning of the optical information signal. Photodetectors should have a high sensitivity in emission wavelength range,

an insensitive to changes in temperature, a minimum amount of noise, a low cost and a fast response speed.

There are several types of photodetectors which are as follows. Phototransistors, photomultipliers, pyroelectric detectors, semiconductor based photoconductors and photodiodes. Among those types, photodiodes are used more often because they have high sensitivity, good efficiency, fast response speed and small size. There are two types of photodiodes that are preferred in optical fiber systems. These are positive intrinsic negative (PIN) photodiode and avalanche photodiode (APD) [33].

#### 5.4.4.1 Positive Intrinsic Negative (PIN) Photodiode

PIN photodiode comprises of three layers which are p-type layer, n-type layer and intrinsic (i-type) semiconductor layer. A layer of intrinsic region is added between p-n junction. Intrinsic region does not have any free charges and due to its high resistance most of the voltage is concentrated in this region. Because of these reasons the depletion region is widened in this type of photodiode. Depletion region is another name for intrinsic region. This region absorbs photons with improved efficiency and the width of it depends on the relationship between responsivity and response time [3], [35], [36]. The structure of a PIN photodiode is shown in Figure 5.11 below.

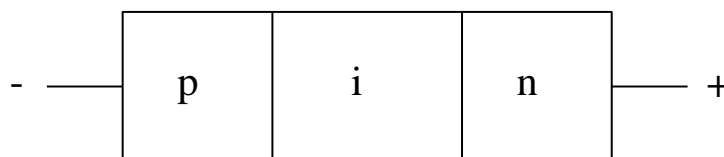


Figure 5.11: The structure of a PIN photodiode

PIN photodiode has some advantages compared to PN photodiode. Stronger doping results in a higher electric field and the concentration of the minority carriers is lower. Although it has some advantages, there are disadvantages too. PIN photodiode does not have an optical to electrical conversion gain and it does not provide an increase in signal strength. PIN photodiode provides some advantages which are as follows. It has higher sensitivity, faster bandwidth response, higher speed, wider optical spectral range and lower polarization current [3], [35], [36].

#### 5.4.4.2 Avalanche Photodiode (APD)

APD is a modified version of PIN photodiode. It is designed to achieve a gain by impact ionization. APD multiplies the primary signal photocurrent which increases receiver sensitivity. When the photo generated carriers pass through a high electric field region, they obtain energy to ionize bound electrons in the valance band. This process is called impact ionization. So the gain is achieved by impact ionization [33], [35], [36].

Unlike PIN photodiode, APD has an additional p-type (or n-type) layer between i-type and n-type regions. The n-type region is highly doped. So APD comprises of four layers which are p-type layer, n-type layer, intrinsic semiconductor layer and an additional p-type (or n-type) layer. The structure of it is similar to PIN photodiode which is shown in Figure 5.12 below.

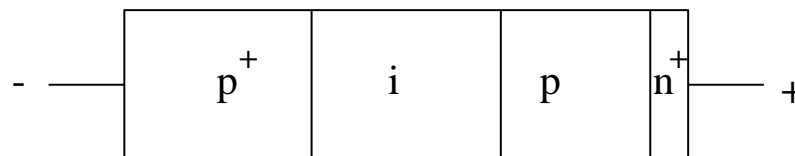


Figure 5.12: The structure of an APD

The advantage of the additional layer is the avalanche multiplication which occurs in p region. By this way the shot noise can be reduced. The multiplication factor ( $M$ ) of APD is written as

$$M = \frac{1}{1 - \left(\frac{V}{V_b}\right)^m} \quad (5.5)$$

where

$V$  = applied reverse bias,  $V_b$  = breakdown voltage and  $m$  = constant.

When  $V = V_b$ ,  $M = \infty$  then the photodiode breaks down. The responsivity ( $R_{APD}$ ) of APD is

$$R_{APD} = MR_{PIN} \quad (5.6)$$

where

$R_{PIN}$  = responsivity of the PIN photodiode.

If the reverse voltage bias is increased, the charge collision time and capacitance decrease. The increase in the reverse bias also increases shot noise. APD has an additional noise called excess noise. When APDs and PIN photodiodes are compared, it is seen that APDs are more sensitive because they use a strong electric field during flow of electrons. They can detect more precisely, more effectively and more clearly than PIN photodiodes. APDs can be characterized as a high gain photodiode receiver. They are more expensive and they require higher bias voltage than PIN photodiodes. Although APDs are more effective, they require more electrical power than PIN photodiodes. They are also more sensitive to temperatures and they include more noise [33], [35], [36].

Some important properties and comparison of silicon, germanium, InGaAs (Indium Gallium Arsenide) APDs and PIN photodiodes are shown in Table 5.1.

Table 5.1: Some important properties of APDs and PIN photodiodes [37]

| Parameter                   | Silicon  |         | Germanium |         | InGaAs                  |                |
|-----------------------------|----------|---------|-----------|---------|-------------------------|----------------|
|                             | PIN      | APD     | PIN       | APD     | PIN                     | APD            |
| Wavelength range (nm)       | 400-1100 |         | 800-1800  |         | 900-1700                |                |
| Peak (nm)                   | 900      | 830     | 1550      | 1300    | 1300<br>(1550)          | 1300<br>(1550) |
| Responsivity (A/W)          | 0.6      | 77-130  | 0.65-0.7  | 3-28    | 0.63-0.8<br>(0.75-0.97) |                |
| Quantum efficiency (%)      | 65-99    | 77      | 50-55     | 55-75   | 60-70                   | 60-70          |
| Gain ( $M$ )                | 1        | 150-250 | 1         | 5-40    | 1                       | 10-30          |
| Excess-noise factor ( $x$ ) | -        | 0.3-0.5 | -         | 0.95-1  | -                       | 0.7            |
| Bias voltage ( $-V$ )       | 45-100   | 220     | 6-10      | 20-35   | 5                       | <30            |
| Dark current (nA)           | 1-10     | 0.1-1   | 50-500    | 10-500  | 1-20                    | 1-5            |
| Capacitance (pF)            | 1.2-3    | 1.3-2   | 2-5       | 2-5     | 0.5-2                   | 0.5            |
| Rise time (ns)              | 0.5-1    | 0.1-2   | 0.1-0.5   | 0.5-0.8 | 0.06-0.5                | 0.1-0.5        |

## 5.5 Fiber Materials

In order to choose a suitable material for an optical fiber, the following conditions should be met [33]:

- a) The material must be suitable for making long and flexible fibers.
- b) In order to direct light efficiently, the material must be transparent.
- c) The material must be suitable for different refractive indices. This is required both for core and cladding.

Main material for most of the glass fibers is silicate or silica ( $SiO_2$ ). High loss glass fibers are used for short transmission distances and low loss glass fibers are used for long transmission distances. Silica must be purified to lower the attenuation. In order to change the index of refraction, different materials are added to silica. Possible combinations for core and cladding are as follows. First option is as follows: cladding can be made up of pure silica and core can be made up of germanium dioxide ( $GeO_2$ ) and silica. Second option is as follows: cladding can be made up of

pure silica and core can be made up of phosphorus pentoxide ( $P_2O_5$ ) and silica. Third option is as follows: core can be made up of pure silica and cladding can be made up of boron trioxide ( $B_2O_3$ ) and silica.

Plastic fibers are used less than glass fibers because they have higher attenuation. They are often used in short distance applications. This is because of the fact that they are durable. Main core material for most of the plastic made fibers is either polymethylmethacrylate (PMMA) or perfluorinated polymer (PFP). The core diameters for plastic fibers are larger than glass fibers because they allow relaxation of connector tolerances [33].

## 5.6 Signal Degradation in Optical Fibers

### 5.6.1 Attenuation

Attenuation is the loss of the signal during propagation. Attenuation is an important concept in optical fibers because it is used for determining the maximum unamplified distance between the transmitter and receiver. Attenuation can also be called as a fiber loss or a signal loss.

When the light propagates along the fiber, its power gets lower. The attenuation in an optical fiber can be calculated from

$$\alpha(dB/km) = \frac{10}{z} \log \left[ \frac{P(0)}{P(z)} \right] \quad (5.7)$$

where

$\alpha$  = attenuation constant,  $z$  = distance,  $P(0)$  = optical power at origin and  $P(z)$  = optical power at distance  $z$ .

Attenuation is closely related to absorption, scattering and radiative losses of optical energy.

Absorption is the process where incident energy is kept without reflecting or sending it while passing through a medium. Absorption is related to the fiber material and it is caused by various mechanisms which are as follows [33]:

- a) Absorption which is caused by atomic faults in glass production.
- b) Intrinsic absorption which is caused by atomic components of optical fiber material.
- c) Extrinsic absorption which is caused by atoms in glass material.

When a light travels through an object or a medium with different properties, the direction of the wave will change. This process is called scattering. Scattering is related to fiber materials and structural faults. The losses due to scattering is called scattering losses which include microscopic changes in material densities and structural faults during production [33].

Attenuation which is caused by the radiative losses arises from the perturbations of fiber geometry.

## **5.6.2 Distortion**

When the optical signals propagate along the optical fiber, the signals get wider and distorted. As the time passes, the signals overlap. The overlapping signals produce errors at the output. The distortion is the result of intermodal and intramodal dispersions.

### **5.6.2.1 Intermodal Dispersion**

Intermodal dispersion is the pulse widening that takes place in multi-mode fibers. It is due to the existence of many modes propagating in the fiber and it measures the time delay between different modes. The signals operating at constant frequency have different group velocities at different modes. Group velocity of a wave is defined as the measured speed of the overall shape of the wave's envelope [33].

### **5.6.2.2 Intramodal Dispersion**

Intramodal dispersion is the pulse widening that takes place in single-mode fibers. It is due to the existence of many wavelengths emitted from the source and variation of the index of refraction with wavelengths. It measures the time delay between the different versions of the same mode. Intramodal dispersion can also be called as chromatic dispersion.

There are two reasons of intramodal dispersion which are material dispersion and waveguide dispersion. In material dispersion the index of refraction changes as a function of wavelength. Fiber appears as many fibers to the source. In waveguide dispersion the index of refraction is not a function of wavelength. Source appears as many sources to the fiber [33].

## **5.7 Applications**

OFSs have many applications in a variety of fields. Some of the applications are explained below.

OFSs are used in measuring and displaying the surroundings with EM radiation. Those environments are transformers, electric motors, power supplies etc. They are also used in applications that require high sensitivity which are gyroscopes, accelerometers and field measurement tools.

The places where nuclear radiation threatens people's health and the measurement of chemical compounds include OFSs. For example photonic nets are used to protect the environment from chemical compounds. They are also used in aircrafts, medicine and biotechnology because of their small size, low weight and immunity to the EMI. Medical measurements include temperature, pressure, blood analysis etc.

OFSs are used in sensing of variables such as cables, fiber optic communication networks etc. Other uses of OFSs are civil engineering structures, electrical machines, many engineering applications, buildings and much more [3], [33].

## **5.8 The Advantages and the Drawbacks of Optical Fiber Sensors**

### **5.8.1 The Advantages of Optical Fiber Sensors**

OFSs offer a large bandwidth and a low transmission loss. This means that more data can be sent over longer distances and this decreases the cost and complexity. Because of their dielectric nature, OFSs are not affected by EMI. They are used safely in military applications without being affected by EM disturbances.

Optical fibers are made up of glass which is an electrical insulator, so they can be used safely in electrically dangerous places. Light is safer than the electric current included technology. The sensors do not need a metallic coaxial cable and metallic parts which disturb the electric field. They are also passive sensors due to their dielectric constructions.

Due to their small size and low weight, the sensors are easier to control and it is possible to scan in narrow places. For example, photonic circuits are placed in a single optical device that helps to miniaturize, become economical and improve capabilities.

Since optical fibers include signals that are inclosed within the waveguide, the signals are sent securely over optical fibers. Some important security applications that use optical fibers are banking, networking and military.

Sensitivity, resolution and dynamic range are higher than other types of sensors. Sensitivity is the ratio between the output signal and measured property. If this ratio is constant, then the sensor is linear or ideal. They need to be sensitive to the measured properties and insensitive to any other properties that are not measured. They can also resist high temperatures and bad conditions [3], [9], [31], [32], [33].

Another importance is the raw material of the optical fiber. The optical fibers are made up of silica which can be found in ordinary sand and it is cheap. A pure glass is made using this raw material.

OFSs also make long distance measurements. In remote sensing and telemetry applications, the fiber can be segmented into parts where one part can be used as the calibration of the sensor and the other part can be used to carry the information to a remote station [3], [9], [31], [32], [33].

The advantages of the optical fiber sensors can be expanded. Because of the reasons explained above, many signal processing devices such as combiner, multiplexer, splitter etc. are made up of optical fibers.

### **5.8.2 The Drawbacks of Optical Fiber Sensors**

In general OFSs cost more than other types of sensors which are produced with different material other than fiber. The cost is obtained directly from the components.

Another disadvantage is the crossed sensitivity. Sensitivity is defined as the reaction capability of the system to the input variables. The output variable can respond one or more than one input variable. The crossed sensitivity is the reaction capability of the system to other input variables which are not desired. However the output variable should only respond to the desired variable. If the crossed sensitivity occurs, the output variables are not obtained correctly. There exist errors. The crossed sensitivity is also a problem for conventional sensors [3], [33].

## CHAPTER 6

# IMPLEMENTATION OF GROUND PENETRATING RADAR (GPR) USING AN OPTICAL FIBER SENSOR

### 6.1 Purpose and Problem Structure

GPR is a method for exploring subsurface geological structures, subsurface objects and much more. As it is explained in Chapter 1 and Chapter 3 before, a typical GPR system comprises of a transmitting and a receiving antenna. The block diagram of a typical GPR system is shown in Figure 1.1. In this study GPR system comprises of an optical fiber sensor (OFS) which makes detection efficiently.

A perfectly conducting circular cylinder is deeply buried in a dielectric half-space. The radius of the cylinder is  $a$  and the depth from the dielectric interface to the center of the cylinder is  $b$ . The cylinder is placed at coordinates  $(0,0)$  which is the origin. This configuration is shown in Figure 6.1.

The purpose is to detect the cylinder's position and depth using a GPR system that comprises of an OFS. By this way the detection is performed efficiently.

### 6.2 The Configuration of the GPR System

The configuration of the GPR system that is used in this study is as follows. It comprises of a transmitter, a target (a perfectly conducting circular cylinder) and an optical fiber sensor interrogation system (OFSIS). This configuration is shown in Figure 6.2.

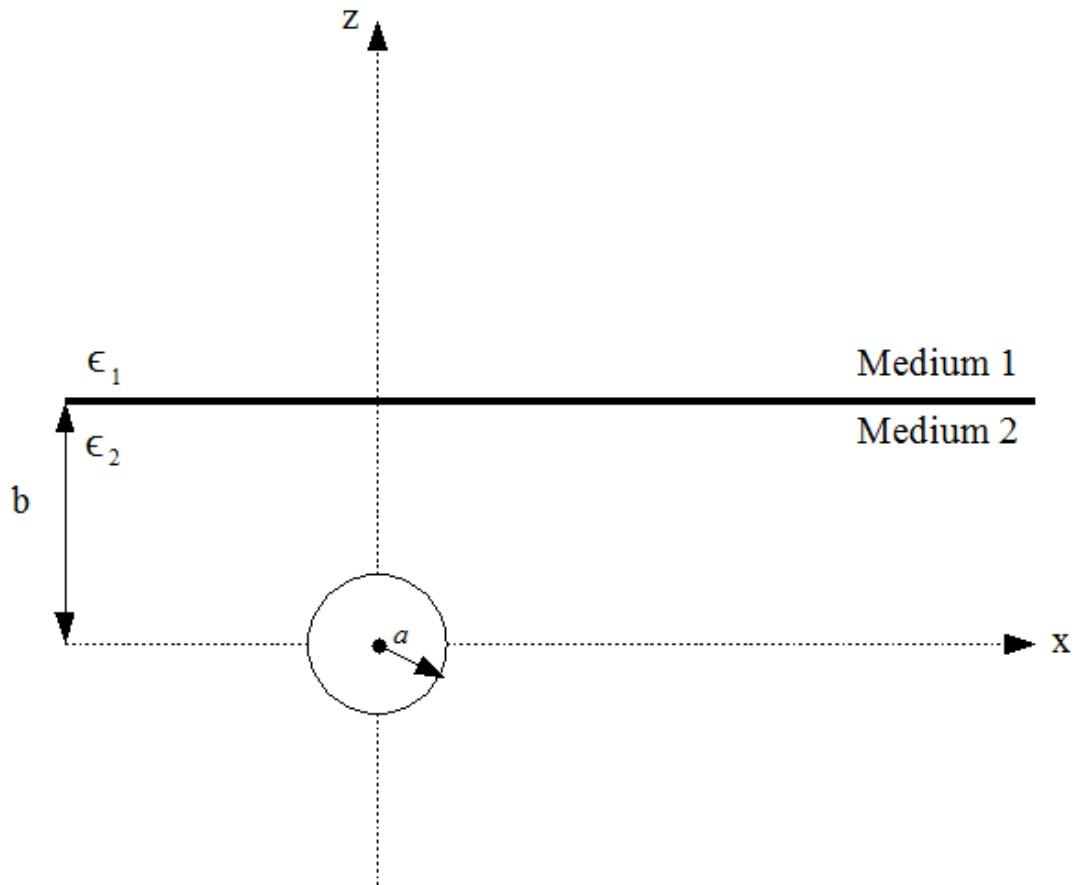


Figure 6.1: The configuration of the buried circular cylinder

The transmitter is placed 100 meters above from the interface. A continuous plane wave, which has unit amplitude and frequency, is sent from the transmitter. In general the radius of the cylinder is taken 5 cm fixed in the study. Medium 1 is taken as air and medium 2 is taken as soil. Soil, which is used in the study, is a sample of martian soil. Both are assumed dielectric and homogeneous, but soil is lossy compared to lossless air medium. OFSIS comprises of a light source (laser as a transmitter), an OFS and a photodetector (as a receiver). OFS comprises of a  $50 \Omega$  optical modulator and an electric field probe. The optical modulator that is used in the study is Mach-Zhender modulator. The configuration of the OFS is shown in Figure 6.3.

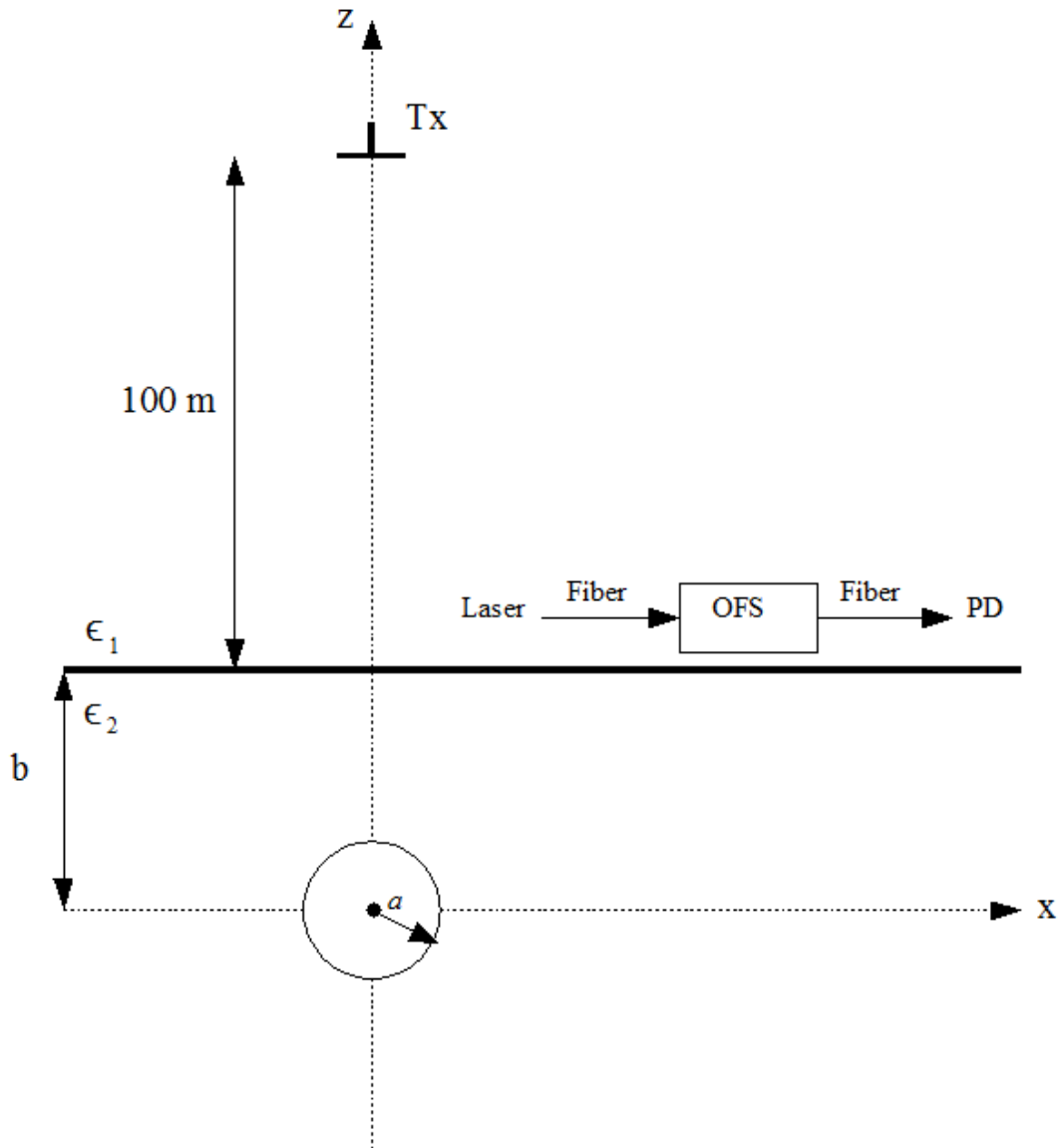


Figure 6.2: The configuration of the GPR system where PD stands for photodetector

An OFS modulates the optical signal strength by the electric field. It has a small size and most of its components are nonmetallic except the electrode. The operating principle of an OFS is as follows. A uniform light is transmitted into the optical wave guides. They are embedded in a  $LiNbO_3$  (Lithium Niobate) board. The electric field in the electric field probe or in the antenna is put in the use of the wave guides. The optical phase shift between two optical paths is induced by electro-optic effect. As a

result interference occurs at the output and the optical intensity changes. The modulated light is then converted into electric field by a photodiode. As a result the output is obtained as a voltage signal [9].

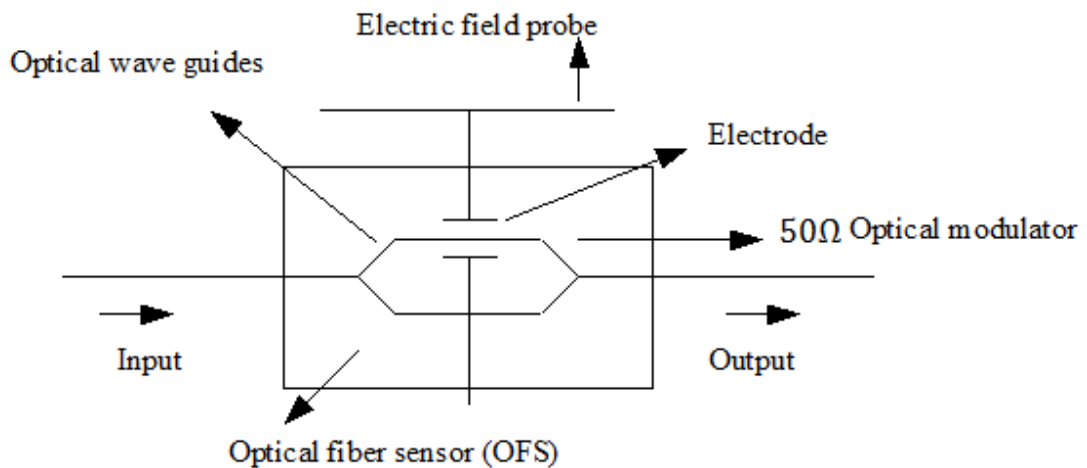


Figure 6.3: The configuration of the OFS

### 6.3 Electric Field Strength at the OFS

In order to detect the circular cylinder's depth and position using an OFS, the electric field strength at the OFS needs to be determined. This electric field strength is equal to the total scattered electric field above the interface.

A unit amplitude plane wave is transmitted from the source. The wave coming from the source propagates either in medium 1 or medium 2. Part of the wave which propagates in medium 1 reflects at the interface. The other part of the wave which propagates through medium 2 refracts at the interface and it scatters after hitting the cylinder. The scattered wave which comes from the cylinder refracts again at the interface. The total scattered electric field above the dielectric interface is the

summation of the reflected electric field from the dielectric interface and the scattered electric field from buried cylinder above the interface. The geometry is shown in Figure 4.2.

The total scattered electric field above the dielectric interface is obtained in Equation 4.24. The detailed analysis of how this expression is obtained is explained in Chapter 4 before. The obtained Equation 4.24 is rewritten as

$$\begin{aligned}
E_{total} &= \frac{(n-1)}{(n+1)} \exp\{-ik_1(z-b)\} \\
&+ \frac{-8k_1^2}{\sqrt{2\pi}(k_1^2 - k_2^2)(k_1 + k_2)} \exp(ik_2b - ik_1b \sin \varphi + ib\sqrt{k_2^2 - k_1^2 \cos^2 \varphi}) \\
&\times \left\{ k_1 \sin^2 \varphi - \sin \varphi \sqrt{k_2^2 - k_1^2 \cos^2 \varphi} \right\} \sum_{n=-\infty}^{n=\infty} \left\{ \frac{(i)^n J_n(k_2 a) \exp(in\varphi_o)}{H_n^{(1)}(k_2 a)} \right\} \\
&\times \frac{\exp(ik_1\rho - i\pi/4)}{\sqrt{k_1\rho}}
\end{aligned} \tag{6.1}$$

So the above equation shows the total scattered electric field above the dielectric interface. It is equal to the electric field strength at the OFS or coming through the OFS.

## 6.4 Analyses Performed in MATLAB

### 6.4.1 Soil Model Used in the Study

Before writing the code of Equation 6.1, the soil model that is used in the study is explained. As it is mentioned before, medium 1 is taken as air and medium 2 is taken as soil. Permeability of air and soil are equal to 1. Permittivity of air is also equal to 1. Soil used in the study is a sample of martian soil. The model of Debye is the most common model for characterizing the dielectric properties of soils. Time domain

reflectometry (TDR) is a technique that is used for measuring dielectric properties of soils. The purpose of this technique is to show the relationship between dielectric constant (relative permittivity) of soils and water content of soils. It is seen that the permittivity of a medium indicates its moisture. The medium has a dielectric behaviour that is explained by Debye model [38], [39]. In the Debye model permittivity of soil is defined as

$$\epsilon_{soil} = \epsilon_{\infty} + \frac{\epsilon_s - \epsilon_{\infty}}{1 + i2\pi f\tau_r} \quad (6.2)$$

where

$\epsilon_{\infty}$  = permittivity at infinity,  $\epsilon_s$  = static permittivity and  $\tau_r$  = permittivity of relaxation time.

Martian soil has values of  $\epsilon_{\infty} = 3.12$ ,  $\epsilon_s = 3.57$  and  $\tau_r = 0.041$  ns [39].

#### 6.4.1.1 The Attenuation

The attenuation appears little because of the Debye model of martian soil that is used during the study. Martian soil is very dry. The attenuation constant ( $\alpha$ ) is the rate that the waves attenuate when they propagate. When there is lossless medium, there is no attenuation ( $\alpha = 0$ ).

The attenuation can be determined in many ways. The real part of the propagation constant ( $\gamma$ ) is defined as the attenuation constant and the imaginary part ( $\beta$ ) of the propagation constant is defined as the phase constant. The phase constant is the rate that the phase changes when waves propagate [22]. The propagation constant is defined as

$$\gamma = \sqrt{i\omega\mu(\sigma + i\omega\epsilon)} = \alpha + i\beta \quad (6.3)$$

The attenuation constant can be determined from

$$\alpha = \omega \sqrt{\frac{\mu\epsilon}{2} \left[ \sqrt{1 + \left(\frac{\sigma}{\omega\epsilon}\right)^2} - 1 \right]} \quad (6.4)$$

The imaginary part of the index of refraction also helps to determine the attenuation constant. In the study the attenuation in dB is determined using the equation below.

$$A = 10 \log_{10} \left( e^{-\text{imag}(n) \frac{2\pi}{\lambda} b} \right) \quad (6.5)$$

where

$n$  = the index of refraction and  $b$  = the depth from the dielectric interface to the center of the cylinder.

In the study the attenuation in dB is also obtained from the attenuation term in the equation of the total scattered electric field above the interface (Equation 6.1). The attenuation term in dB is then written as

$$A = 10 \log_{10} (e^{ik_2 b - i}) \quad (6.6)$$

So the attenuation is determined using Equation 6.5 and Equation 6.6 in the study. Both of the equations give the same result. In general the radius of the cylinder is taken 5 cm fixed. By changing the depth of the cylinder ( $b$ ) from 10 cm to 100 cm, the attenuation is observed at a fixed frequency ( $f$ ) of 100 MHz. The graph in Figure 6.4 shows depth versus attenuation of martian soil at  $f = 100$  MHz.

It is observed that as the depth of the cylinder increases, the attenuation also increases. From Equation 6.5 it can also be observed that as the depth increases, the attenuation increases too. As it is mentioned before, attenuation appears little because of the Debye model of martian soil that is used in the study. If the depth is increased more, attenuation can be observed more clearly.

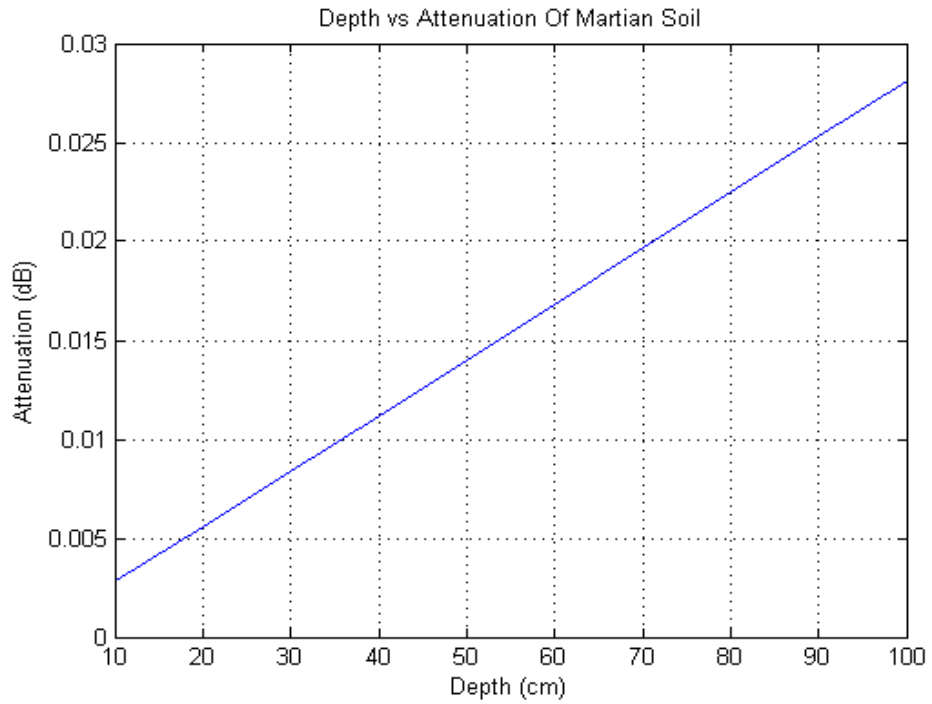


Figure 6.4: The graph shows depth versus attenuation of martian soil at  $f = 100$  MHz

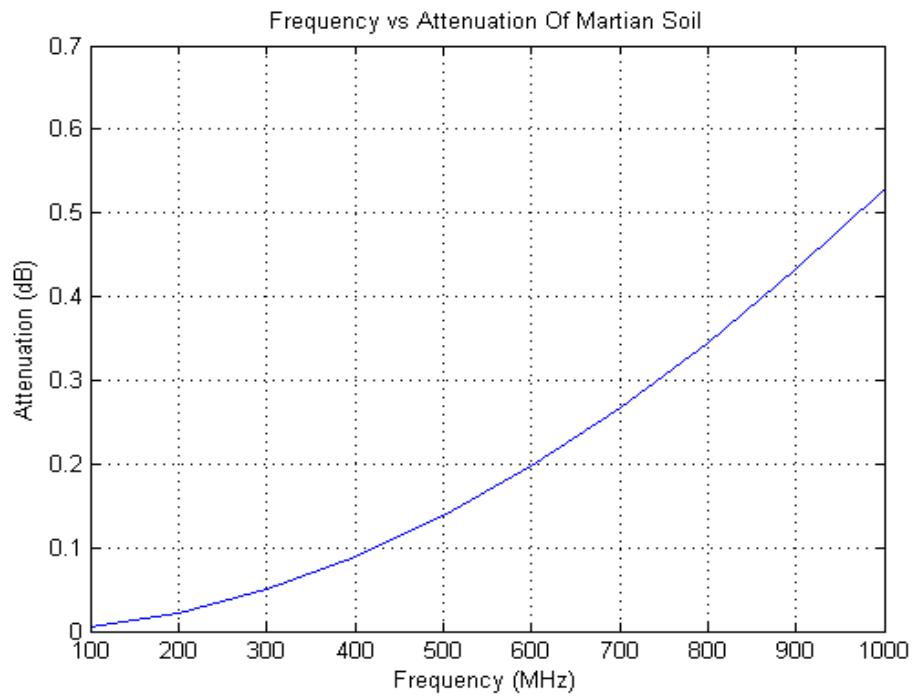


Figure 6.5: The graph shows frequency versus attenuation of martian soil at a fixed depth of  $b = 20$  cm

By changing the frequency ( $f$ ) of the system from 100 MHz to 1 GHz, the attenuation is observed at a fixed depth of  $b = 20$  cm. The graph in Figure 6.5 shows frequency versus attenuation of martian soil at  $b = 20$  cm. It is observed that as the frequency of the system increases, the attenuation also increases. From Equation 6.5 it can also be observed that as the frequency increases, the attenuation increases too. This is because of wavelength that is related to the frequency.

As it is mentioned before the attenuation in Equation 6.5 is obtained using the imaginary part of the index of refraction. By changing the frequency of the system from 100 MHz to 1 GHz, the index of refraction ( $n$ ) is observed at a fixed depth of  $b = 20$  cm. The graph in Figure 6.6.a shows the frequency versus the real part of index of refraction of martian soil at  $b = 20$  cm. The graph in Figure 6.6.b shows the frequency versus the imaginary part of index of refraction of martian soil at  $b = 20$  cm. It is observed that as the frequency of the system increases, the imaginary part of index of refraction also increases. However, the real part of index of refraction decreases very little.

The index of refraction is related to the permittivity of martian soil. The relationship is shown from

$$n = \text{real}(\sqrt{\epsilon_{soil}}) + i|\text{imag}(\sqrt{\epsilon_{soil}})| \quad (6.7)$$

So in order to obtain the index of refraction, permittivity is needed. By changing the frequency of the system from 100 MHz to 1 GHz, the permittivity of the martian soil is observed at a fixed depth of  $b = 20$  cm. The graph in Figure 6.7.a shows the frequency versus the real part of the permittivity of martian soil at  $b = 20$  cm. The graph in Figure 6.7.b shows the frequency versus the imaginary part of the permittivity of martian soil at  $b = 20$  cm. It is observed that as the frequency of the system increases, both the real and the imaginary parts of the permittivity decrease. From Equation 6.7 it can also be observed that as the frequency increases, both the real and imaginary parts of the permittivity decrease.

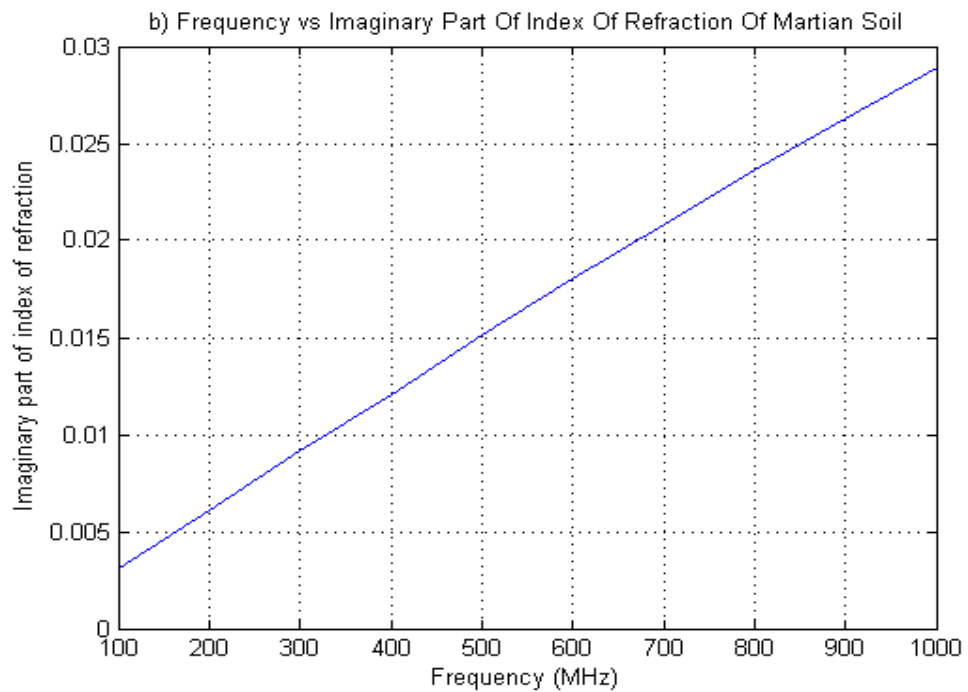
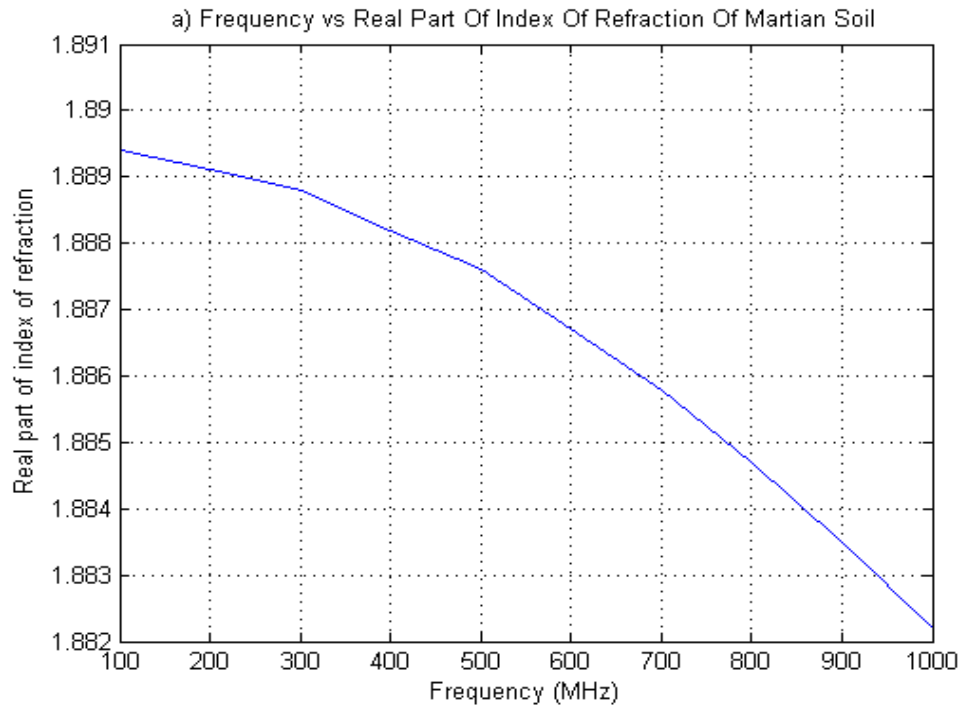


Figure 6.6: a) The graph shows frequency versus real part of index of refraction of martian soil at a fixed depth of  $b = 20$  cm b) The graph shows frequency versus imaginary part of index of refraction of martian soil at a fixed depth of  $b = 20$  cm

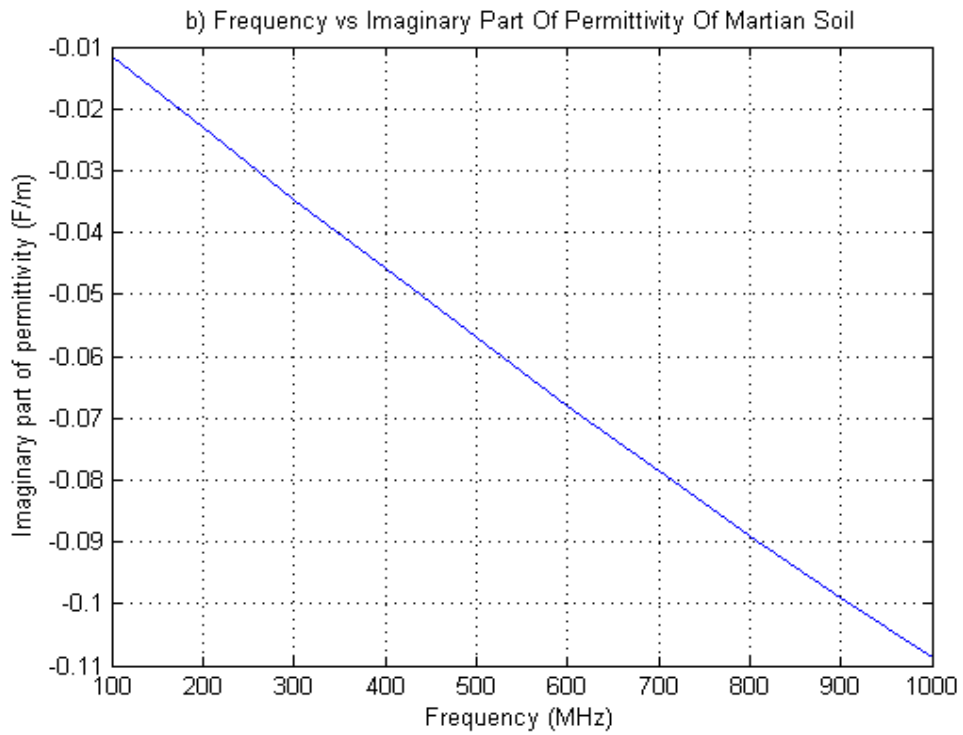
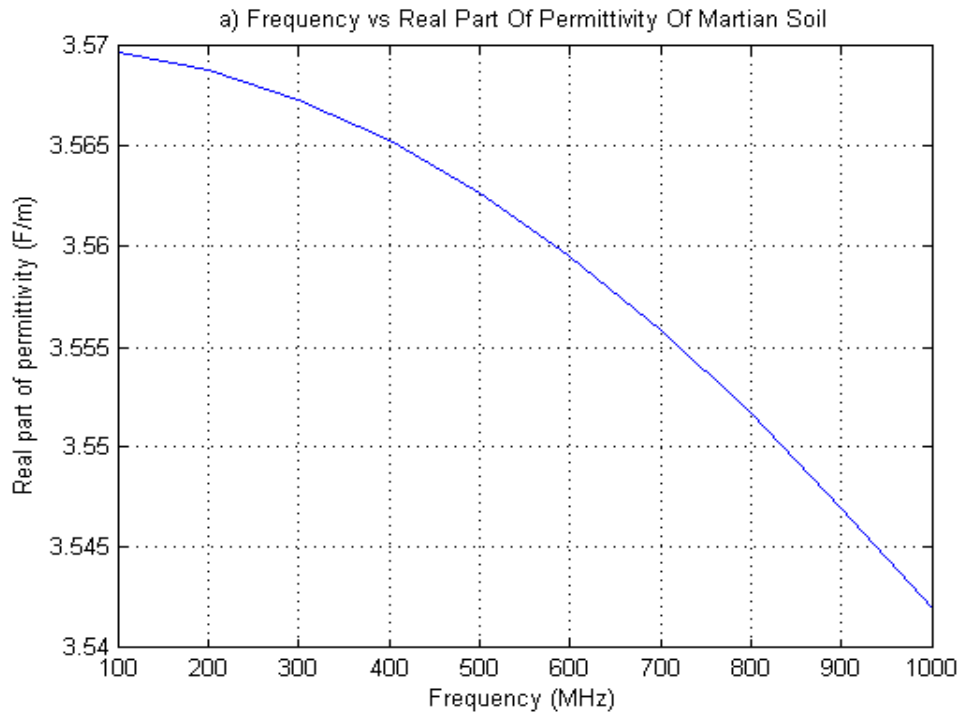


Figure 6.7: a) The graph shows frequency versus real part of permittivity of martian soil at a fixed depth of  $b = 20$  cm b) The graph shows frequency versus imaginary part of permittivity of martian soil at a fixed depth of  $b = 20$  cm

#### 6.4.1.2 The Attenuation of Wet Soil

As it is mentioned before, the attenuation appears little because of the Debye model of martian soil that is used during the study. If another soil model is used, more attenuation could be observed. An example of this is a wet soil that has values of  $\epsilon_{\infty} = 6$ ,  $\epsilon_s = 12$  and  $\tau_r = 1$  ns [40]. Using Equation 6.5 and Equation 6.6 again, the attenuation is determined for a wet soil.

By changing the depth of the cylinder ( $b$ ) from 10 cm to 100 cm, the attenuation is observed at  $f = 100$  MHz. The graph in Figure 6.8 shows the depth versus the attenuation of wet soil at  $f = 100$  MHz.

It is observed that as the depth of the cylinder increases, the attenuation also increases. From Equation 6.5 it can also be observed that as the depth increases, the attenuation increases too.

By changing the frequency of the system from 100 MHz to 1 GHz, the attenuation is observed at a fixed depth of  $b = 20$  cm. The graph in Figure 6.9 shows the frequency versus the attenuation of wet soil at  $b = 20$  cm. It is observed that as the frequency of the system increases, the attenuation also increases. From Equation 6.5 it can also be observed that as the frequency increases, the attenuation increases too.

If the attenuation values of the martian soil and the wet soil are compared, it can be observed that wet soil has much more attenuation. This is because martian soil is very dry. The attenuation is obtained using Equation 6.5 and Equation 6.6. They can be observed in Figures 6.4, 6.5, 6.8 and 6.9. In the study the Debye model of the martian soil is used. The attenuation is very little for the depth range between 10 cm and 100 cm. More attenuation is observed in this model when the depth is increased.

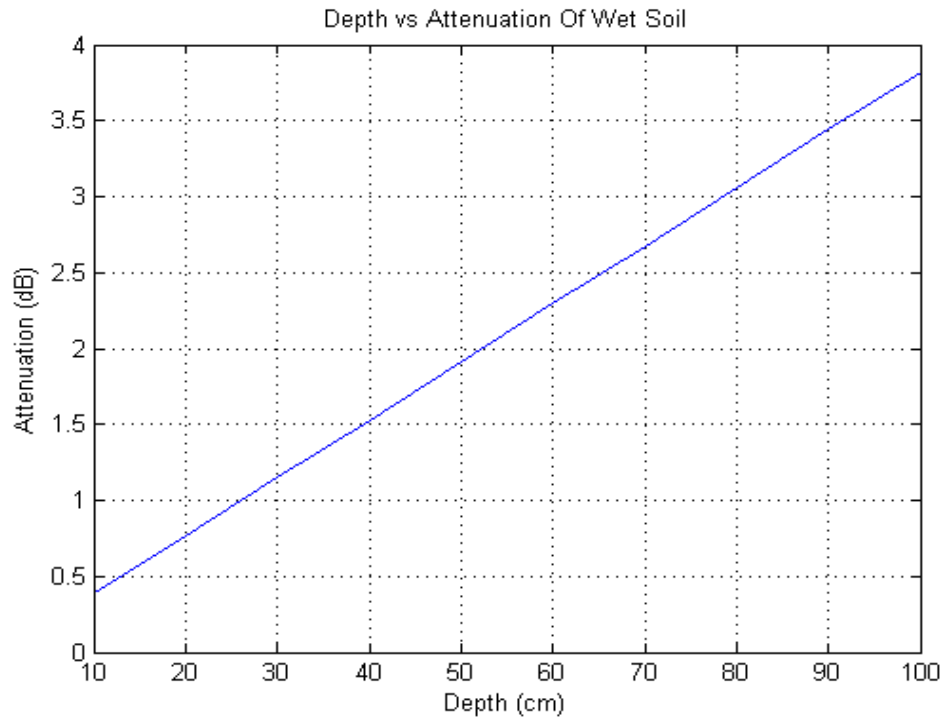


Figure 6.8: The graph shows depth versus attenuation of wet soil at  $f = 100$  MHz

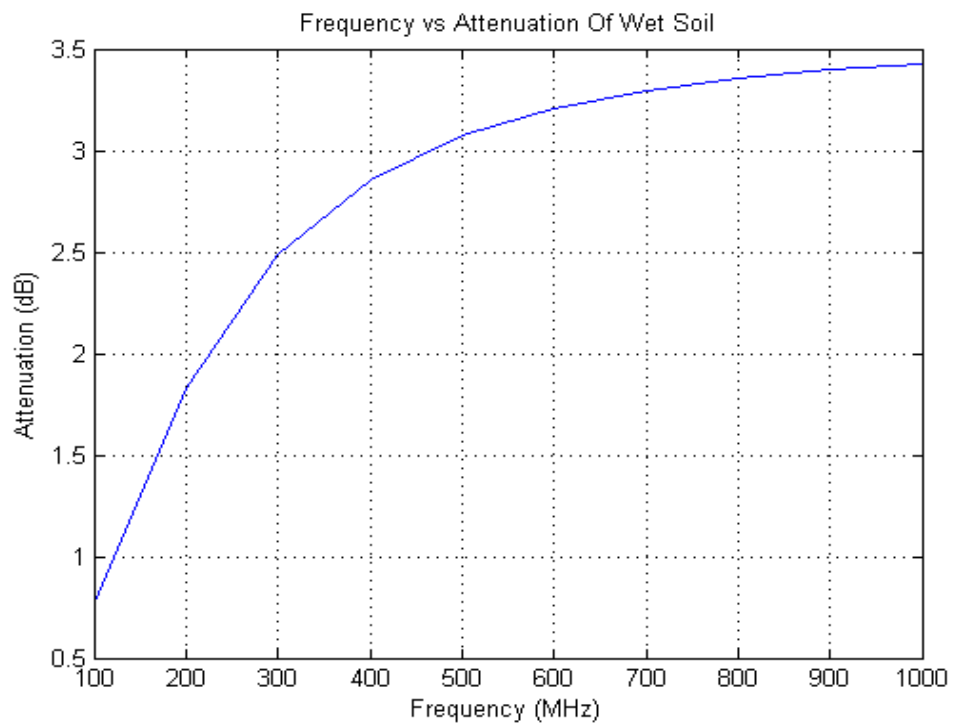


Figure 6.9: The graph shows frequency versus attenuation of wet soil at fixed depth of  $b = 20$  cm

## 6.4.2 MATLAB Analysis of Electric Field Distribution

In order to see the electric field distribution or strength, MATLAB package program is used. After finding the electric field mathematically in Equation 6.1, a two dimensional (2D) and a three dimensional (3D) plot of the electric field distribution are obtained by writing the total scattered electric field's MATLAB code.

After explaining the soil model that is used in the study, plots of the electric field distribution are obtained by writing the total scattered electric field's MATLAB code. This code is obtained by writing the MATLAB code of Equation 6.1. Before writing the code of Equation 6.1, the variables related to the equation are defined. First of all the values of the speed of light and permittivity of free space are defined. ( $c =$  the speed of light  $= 2.98 \times 10^8$   $m/s$  and  $\epsilon_o =$  permittivity of free space  $= 8.854 \times 10^{-12}$   $F/m$ ) The value of the frequency is also defined. During the study the frequency is often changed to see the effects of it. The values of the frequency vary from 100 MHz to 1 GHz. The operating frequency of the system is taken between 100 MHz to 1 GHz. The reason of this is as follows. When the frequency is lower than 100 MHz, the antenna cannot collect the signals. When the frequency is higher than 1 GHz, surface roughness will create scattering interference patterns.

In addition to the soil permittivity parameters due to Debye model, propagation constant of medium 1 ( $k_1$ ), propagation constant of medium 2 ( $k_2$ ), the index of refraction ( $n$ ) and the conductivity ( $\sigma$ ) are also defined in the code of the electric field distribution. The conductivity formula that is used is written as

$$\sigma = n^2 4\pi f \epsilon_o \quad (6.8)$$

The values of  $a$  and  $b$  are assigned. The radius of the cylinder ( $a$ ) is taken 5 cm fixed. The value of  $b$  is changed to observe the effect of the depth variation on the electric field distribution. The values of the depth of the cylinder ( $b$ ) vary from 10 cm to 100 cm.

After assigning some necessary values, the MATLAB code for the total scattered electric field above the dielectric interface is written using Equation 6.1. The scattered electric field from buried cylinder above the interface is named as scattered, the reflected electric field from the dielectric interface is named as surface\_ref and the total scattered electric field above the dielectric interface is named as etotal in the code. This code is shown in Appendix A. After writing the code, it is run and simulated in MATLAB package program.

#### 6.4.2.1 Simulation Results

The 2D and 3D plots of the total electric field distribution are obtained. The 3D plot of the total electric field distribution shows vertical displacement ( $x$ ) versus height ( $z$ ) versus electric field voltage values in dB. The 2D plot shows electric field distribution variation due to  $x$  axis versus  $z$  axis values. The interval of  $x$  axis is taken between -5 to 5 meters. The interval of  $z$  axis is taken between 0.1 to 1 meters. The axis resolution is 0.98 cm for 10 bits of measurement step resolution.

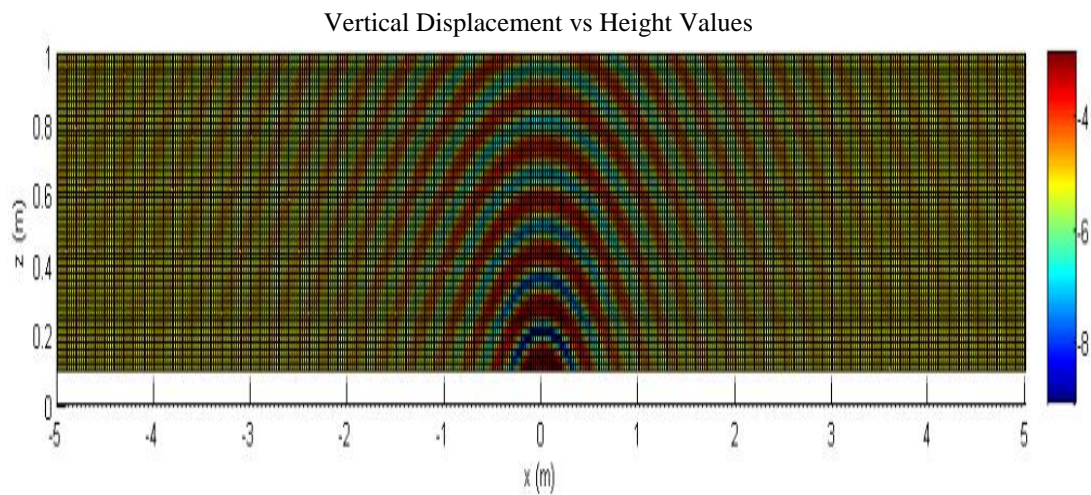


Figure 6.10: The 2D plot of electric field distribution variation due to vertical displacement versus height values for  $f = 1$  GHz and  $b = 10$  cm

Keeping the radius of the cylinder ( $a = 5$  cm) and the frequency of the system constant, depth values are changed between 10 cm to 100 cm. The graph in Figure 6.10 shows the 2D plot of electric field distribution variation due to vertical displacement versus height values. Those are obtained for  $f = 1$  GHz and  $b = 10$  cm.

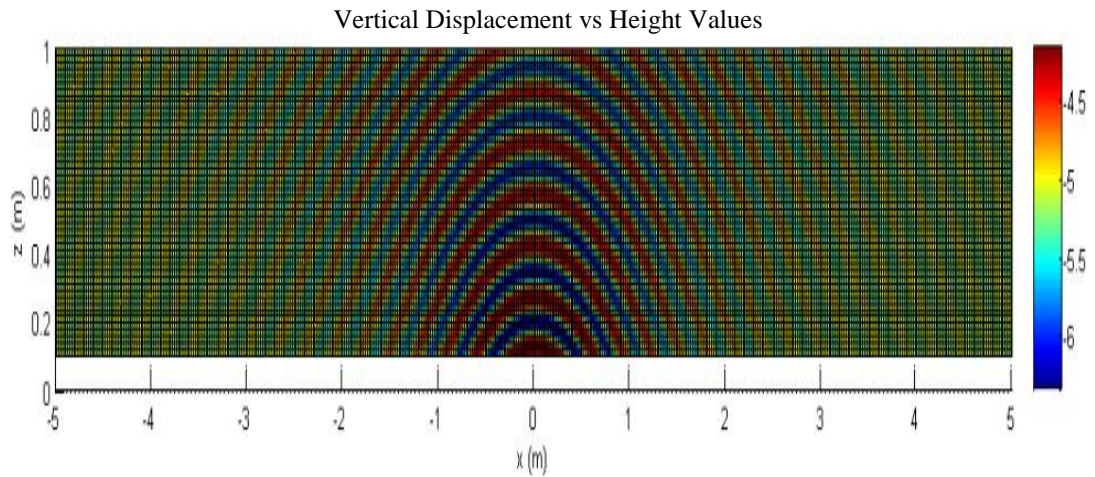


Figure 6.11: The 2D plot of electric field distribution variation due to vertical displacement versus height values for  $f = 1$  GHz and  $b = 50$  cm

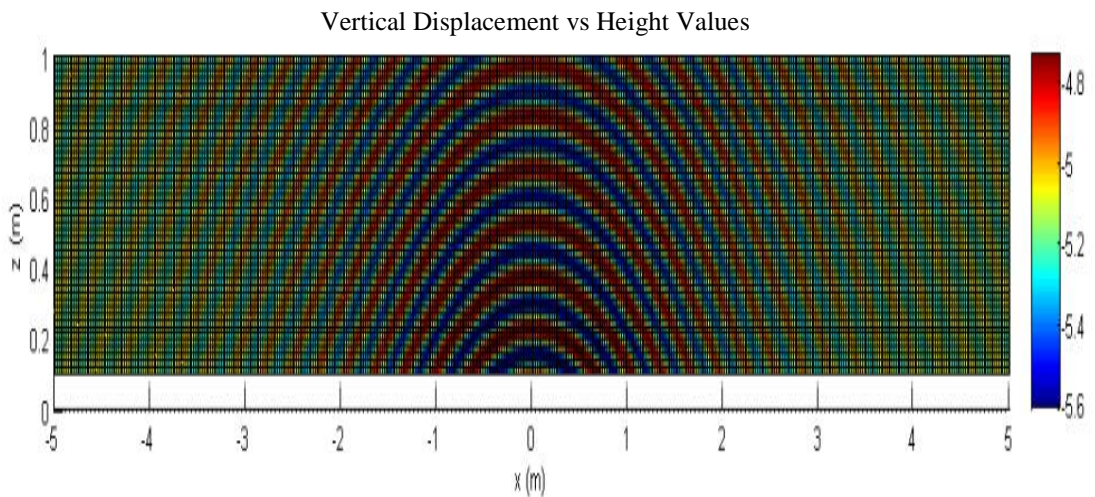


Figure 6.12: The 2D plot of electric field distribution variation due to vertical displacement versus height values for  $f = 1$  GHz and  $b = 100$  cm

The graph in Figure 6.11 shows the same 2D plot of electric field distribution for  $b = 50$  cm and the graph in Figure 6.12 also shows the same 2D plot of electric field distribution for  $b = 100$  cm. The graph in Figure 6.13 shows the 3D plot of vertical displacement versus height versus total electric field. It is obtained for  $f = 1$  GHz and  $b = 10$  cm. The graph in Figure 6.14 shows the same 3D plot for  $b = 50$  cm.

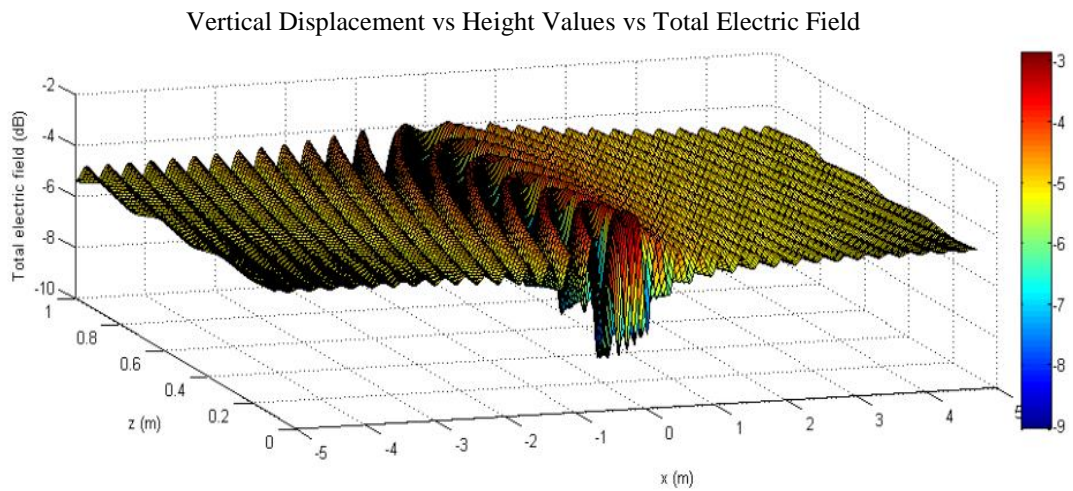


Figure 6.13: The 3D plot of vertical displacement versus height versus total electric field for  $f = 1$  GHz and  $b = 10$  cm

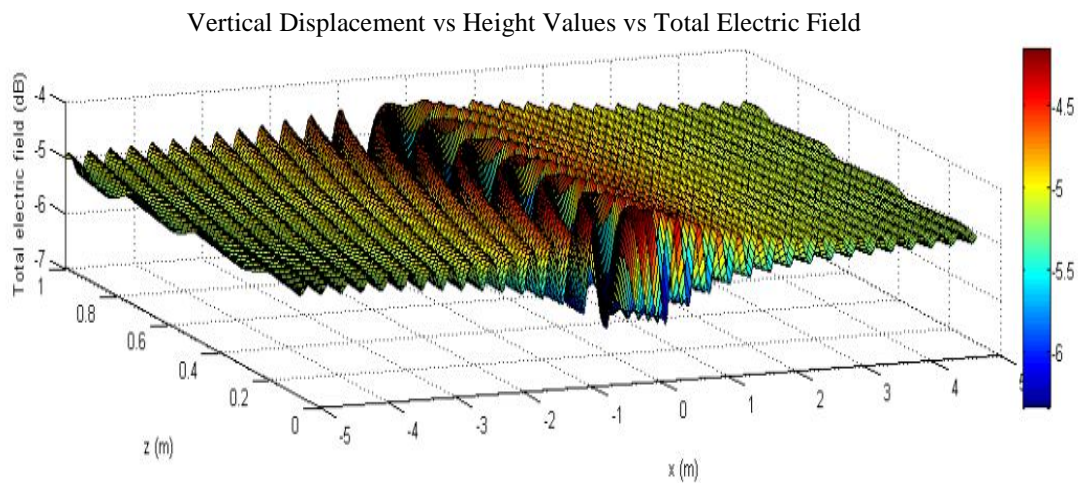


Figure 6.14: The 3D plot of vertical displacement versus height versus total electric field for  $f = 1$  GHz and  $b = 50$  cm

The graph in Figure 6.15 also shows the same 3D plot for  $b = 100$  cm.

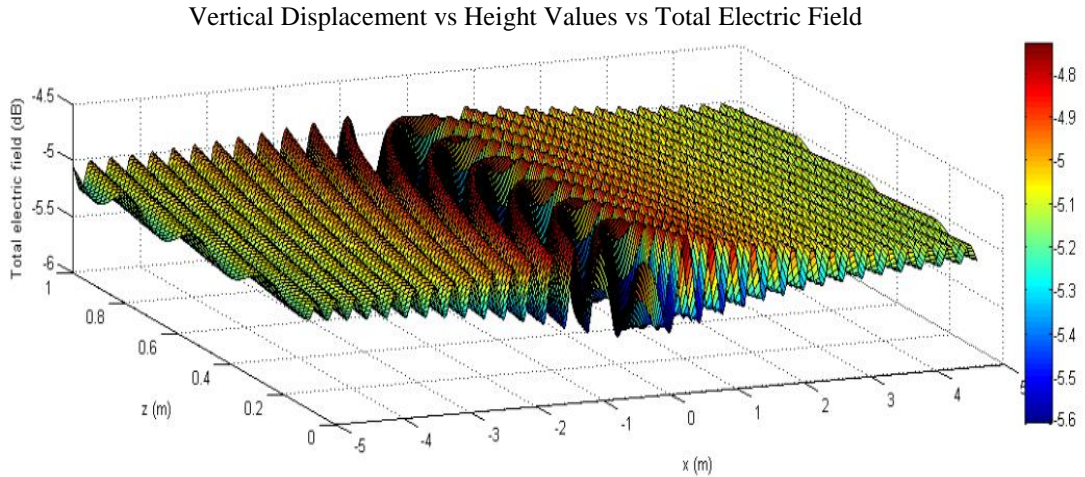


Figure 6.15: The 3D plot of vertical displacement versus height versus total electric field for  $f = 1$  GHz and  $b = 100$  cm

2D and 3D plots, which are obtained above, are compared. When the depth of the object increases, the contrasts around origin increase. This means that there are more dark blue and dark red colors. This indicates that the relative ratio between the maximum and the minimum electric field strength points of the wave increases.

It is also observed that when the depth increases, the antinode of the wave increases. The object is placed at the origin in which the shape of the antinode of the wave changes due to a change in depth. This supports the fact that as the depth of the object increases, the wave's shape goes from spherical to parabolic to plane wave like appearance. So at the infinity the object acts like a plane wave. As a result of the increase in antinode, it is harder to make sensitive measurements.

The oscillations around the origin are more frequent and the scattered wave due to target is more powerful at smaller depths. This is because of the fact that attenuation

increases with distance. When the target is placed at further points, attenuation increases and the power of the scattered wave decreases. When there is interference between reflected CW and scattered wave due to cylinder, the effect of the CW is observed more at further depths.

Keeping the radius of the cylinder ( $a = 5$  cm) and the depth of the cylinder constant, frequency values are changed between 100 MHz to 1 GHz. However, there is an example of frequency value of  $f = 1.5$  GHz. The graph in Figure 6.16 shows the 2D plot of electric field distribution variation due to vertical displacement versus height values. Those are obtained for  $b = 20$  cm and  $f = 500$  MHz.

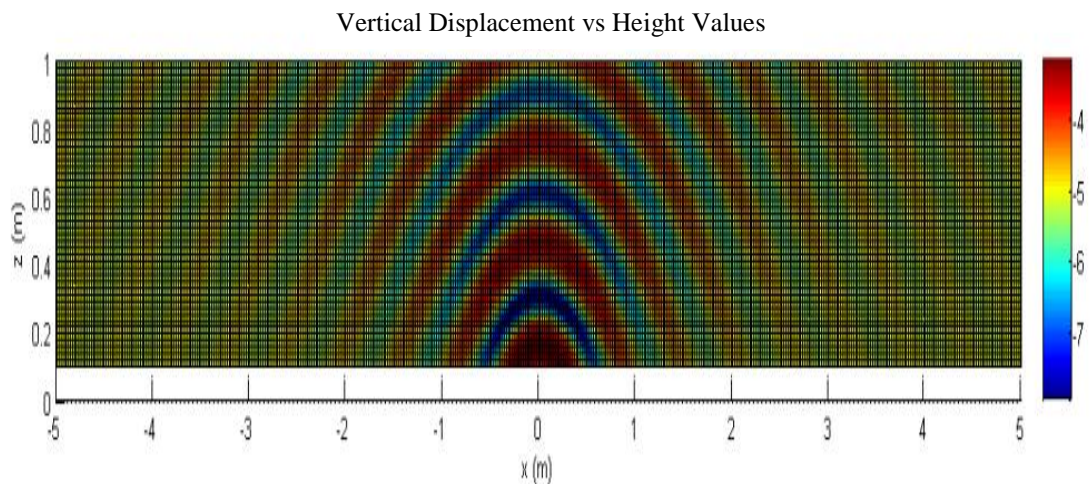


Figure 6.16: The 2D plot of electric field distribution variation due to vertical displacement versus height values for  $b = 20$  cm and  $f = 500$  MHz

The graph in Figure 6.17 shows the same 2D plot of electric field distribution for  $f = 1$  GHz and the graph in Figure 6.18 also shows the same 2D plot of electric field distribution for  $f = 1.5$  GHz.

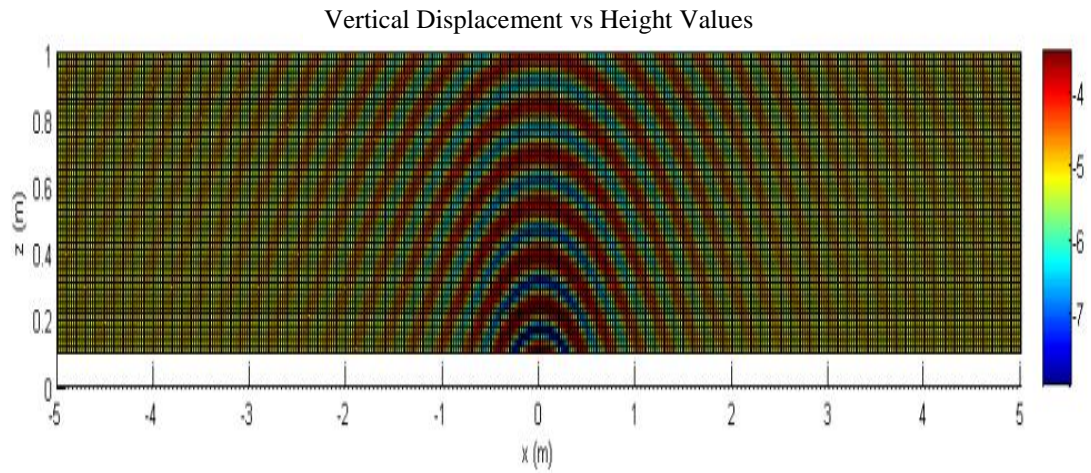


Figure 6.17: The 2D plot of electric field distribution variation due to vertical displacement versus height values for  $b = 20$  cm and  $f = 1$  GHz

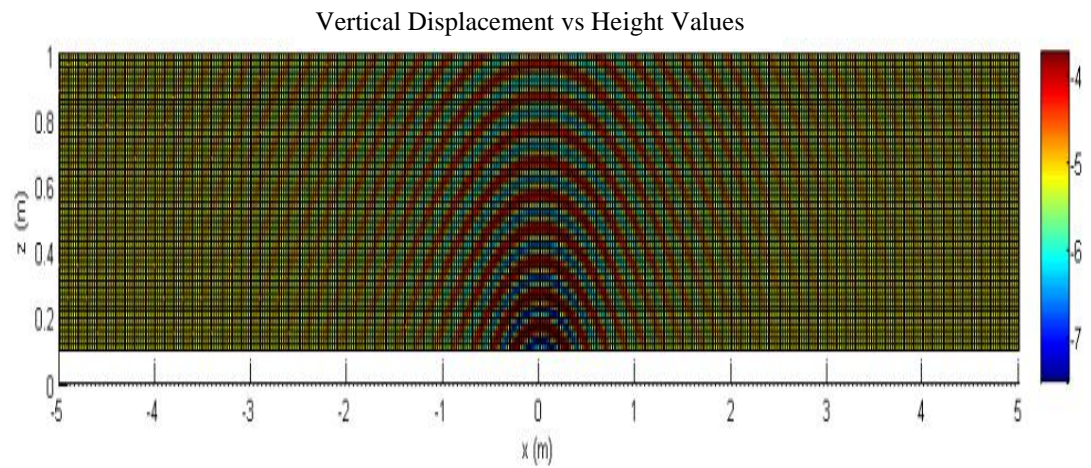


Figure 6.18: The 2D plot of electric field distribution variation due to vertical displacement versus height values for  $b = 20$  cm and  $f = 1.5$  GHz

The graph in Figure 6.19 shows the 3D plot of vertical displacement versus height versus total electric field. Those are obtained for  $b = 20$  cm and  $f = 500$  MHz. The graph in Figure 6.20 shows the same 3D plot for  $f = 1$  GHz.

Vertical Displacement vs Height Values vs Total Electric Field

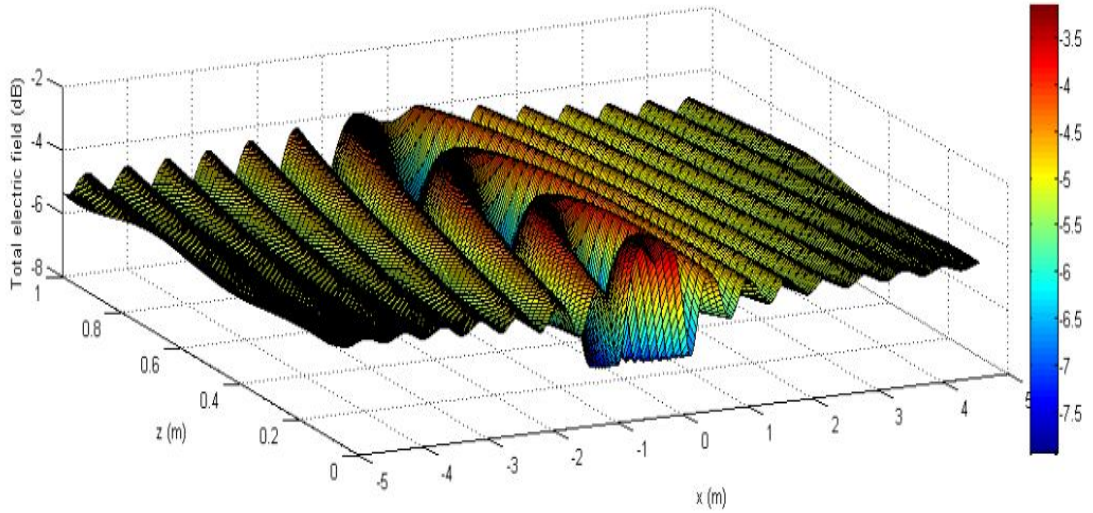


Figure 6.19: The 3D plot of vertical displacement versus height versus total electric field for  $b = 20$  cm and  $f = 500$  MHz

Vertical Displacement vs Height Values vs Total Electric Field

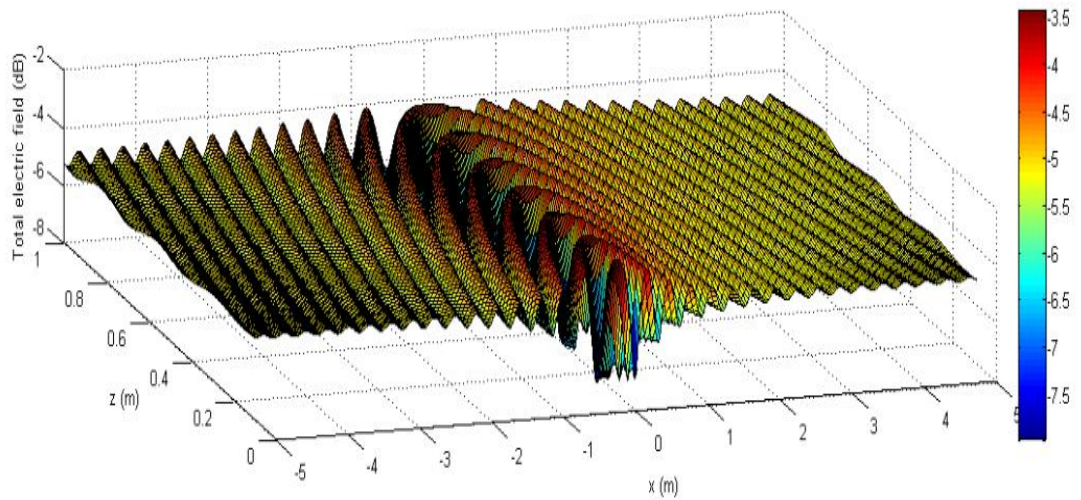


Figure 6.20: The 3D plot of vertical displacement versus height versus total electric field for  $b = 20$  cm and  $f = 1$  GHz

The graph in Figure 6.21 also shows the same 3D plot for  $f = 1.5$  GHz.

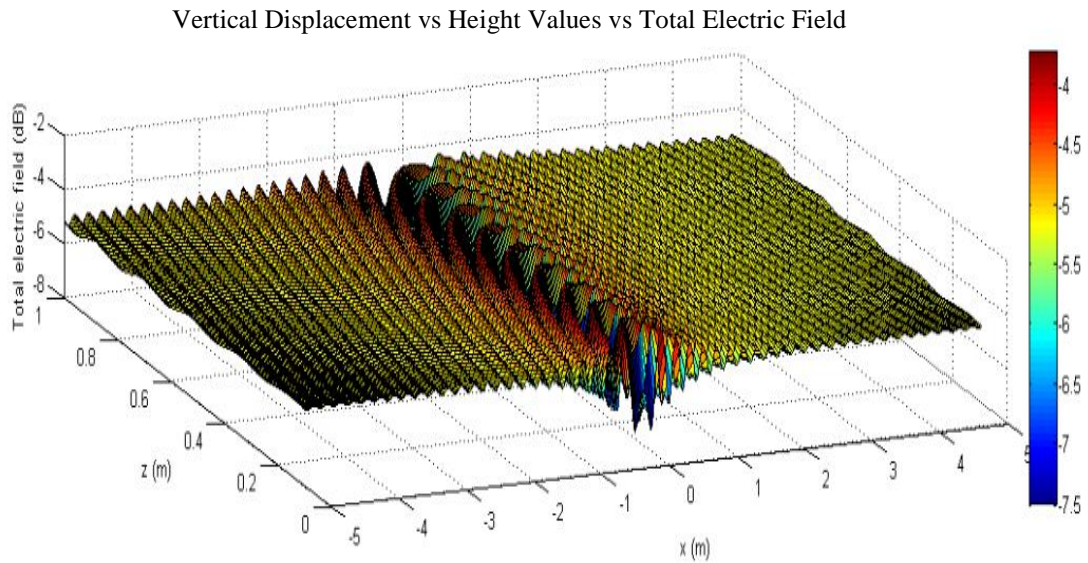


Figure 6.21: The 3D plot of vertical displacement versus height versus total electric field for  $b = 20$  cm and  $f = 1.5$  GHz

2D and 3D plots, which are obtained above, are compared. When the frequency of the system increases, the electric field patterns appear more frequently. This increases resolution and it helps to make more sensitive measurements. The contrast does not change with the depth variation.

When the frequency increases, attenuation increases. Then the power of the scattered wave decreases. When there is interference between reflected CW and scattered wave due to cylinder, the effect of the CW is observed more at further depths. This results in a decrease in the contrast of electric field power variation.

There is a trade off in terms of system performance. In high frequencies, there is an advantage with resolution. In low frequencies, more contrast of electric field power variation occurs. Higher frequencies need to be used if the place of the object is not deep. This is because of the fact that there is more power coupling and better resolution. However, lower frequencies need to be used if the position of the object is truly deep. This is because of the fact that there is less attenuation in low frequencies.

### 6.4.3 MATLAB Analysis of OFS

After obtaining the total electric field strength propagating through the OFS, the voltage at the electric field distribution needs to be measured. The voltages at the electric field distribution are collected by OFS.

In order to detect the cylinder's position and depth, first of all the voltages need to be measured. Those are performed by writing the MATLAB code of the sensor. As it is explained before, the transmitter is placed at 100 meters above the interface. A continuous plane wave is sent from the transmitter. The total scattered electric field above the dielectric interface is obtained before. OFS travels along x axis to measure the voltage induced due to the electric field strength variations. The voltage at the sensor is equal to the electric field difference. As a result of this difference, voltage difference occurs.

The MATLAB code of the total electric field strength is explained in Section 6.4.2 before. The MATLAB code for the sensor is written related to that code.

Some variables related to the OFS are defined. As it is mentioned before, OFS comprises of a  $50 \Omega$  optical modulator and an electric field probe. The electric field probe length is taken as 5 cm. The transmitter antenna is placed at 100 meters above the interface and it has 100 dB of antenna power.

In order to measure the voltage inside the electric field distribution, the electric field strength (received signal level or signal strength) is defined in the code. Signal strength is defined as the magnitude of the electric field at a reference point. The reference point is away from the transmitter.

The electric field strength at a point is related to the transmitting antenna power, radiation resistance and geometry. Radiation resistance is also named as receiver antenna series resistance. For shorted dipole ( $L_{probe} \ll \lambda/2$ ) the receiver antenna series resistance is defined as [41]

$$R_{series} = 20\pi^2 \left( \frac{L_{probe}}{\lambda} \right)^2 \quad (6.9)$$

where

$L_{probe}$  = electric field probe length and  $\lambda$  = wavelength.

The electric field strength shows the relationship between transmitting antenna power and produced electric field. The electric field strength can be written as

$$E_{strength} = \frac{9.48\sqrt{P_{avg}}}{r} \quad (6.10)$$

where

$r$  = transmitter distance to the interface and  $P_{avg}$  = transmitting antenna power.

The electric field strength or the electric field amplitude is adjusted due to transmitting antenna power and distance.

Antenna factor is also defined in the code. It is the ratio of the incident electric field strength to the voltage. The receiver antenna factor of a 3dB antenna is written as

$$R_x AF = \frac{9.73}{\lambda\sqrt{G}} \quad (6.11)$$

where  $G$  = gain (It is 1.64 for a short dipole)

There exists a power coupling as a result of the receiver antenna series resistance. Power couples on the antenna depending on the receiver antenna factor. The coupled power is equal to electric field multiplied by receiver antenna factor. OFS is assumed to have a 50  $\Omega$  impedance. Impedance matching is designed to maximize the power obtained and minimize the load reflections. The load needs to be matched exactly to source impedance to achieve the design purposes. If an impedance mismatch occurs, there exist losses [41]. Receiver responsivity shows the effect of the impedance

mismatch. When there is an impedance mismatch, the responsivity gets smaller for the OFS. Receiver responsivity is related to the receiver antenna factor and the impedance mismatch at the receiver. It is defined as

$$R_x Resp = R_x AF \left( \frac{50}{50 + R_{series}} \right)^2 \quad (6.12)$$

After the code of the sensor part, the probe voltage part of the code is executed. The sensor travels along x axis to measure the voltages inside the electric field distribution. The voltages change depending on the position of the sensor. The signal strength changes due to probe height variations. When the sensor travels along x axis, the amount of scattered signals inside the electric field distribution change.

The electric field probe angle or the orientation angle is 0. In general, the probe height is taken 10 cm. The incident electric field that OFS is propagating through is defined as  $E_{seen}$ . The effect of frequency and impedance matching is observed at the measured output voltage. The measured voltage at the OFS is obtained due to the effect of optical modulator. It is defined as

$$V_{seen} = E_{seen} \times R_x Resp \quad (6.13)$$

After writing the code, it is run and simulated in MATLAB package program. This code is shown in Appendix A.

#### **6.4.3.1 Simulation Results**

For 10 cm of probe height, the value of the system frequency is incremented by 100 MHz each time. It starts from 100 MHz and ends at 1 GHz. For each value of the frequency, the depth of the cylinder is changed from 10 cm to 100 cm. It is incremented by 10 cm each time. So the measured values are obtained by changing the values of frequency and depth of the cylinder in the code. The measured voltage values or the electrical field voltage occurring captured at the OFS are defined as  $V_{read}$ . 2D plots of x axis versus  $V_{read}$  values are obtained for different values of

frequency and depth of the cylinder. Those plots are related to the interference fringe patterns.

By changing the frequency of the system from 100 MHz to 1 GHz, the measured voltage values ( $V_{read}$ ) are observed at a fixed depth of  $b = 20$  cm, radius ( $a$ ) of 5 cm and probe height of 10 cm. The following graphs show the measured voltage values at different frequencies. The graph in Figure 6.22 shows  $x$  axis versus  $V_{read}$  at  $f = 100$  MHz.

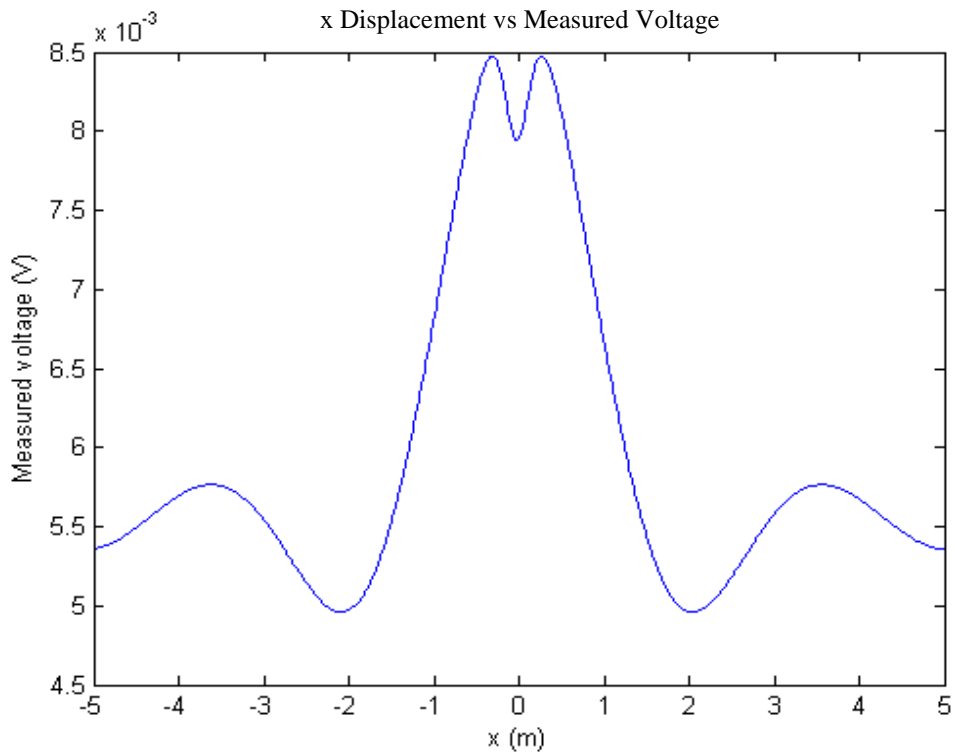


Figure 6.22: The graph shows  $x$  displacement versus the measured voltage for  $b = 20$  cm, probe height = 10 cm and  $f = 100$  MHz

The graph in Figure 6.23.a shows the same 2D plot for  $f = 500$  MHz. The graph in Figure 6.23.b also shows the same 2D plot for  $f = 1$  GHz.

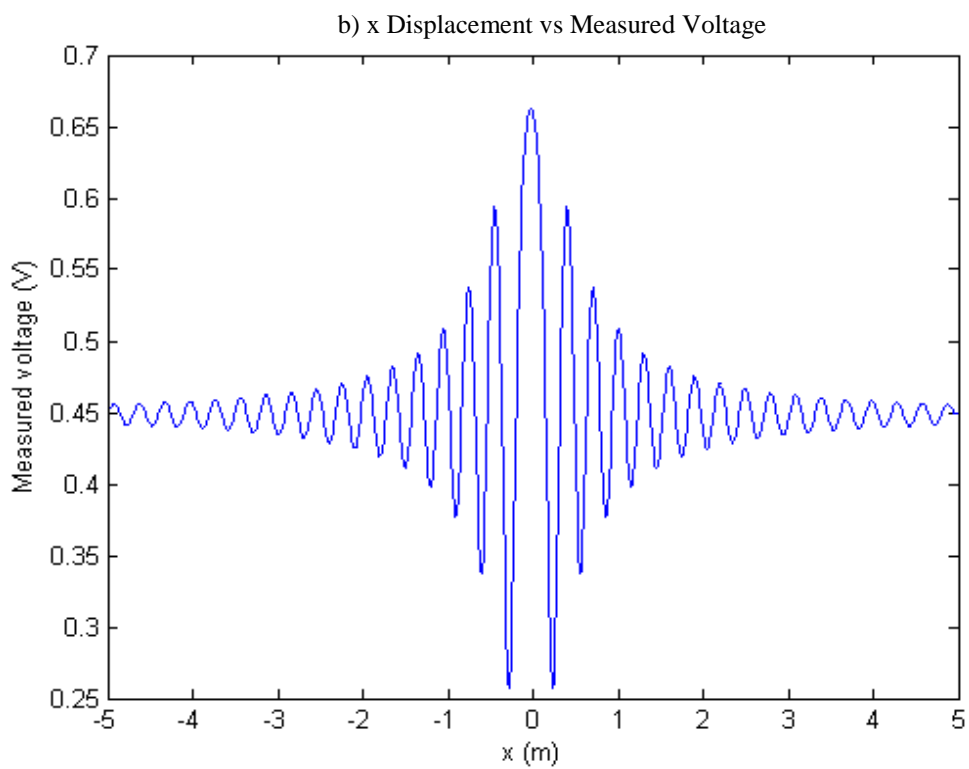
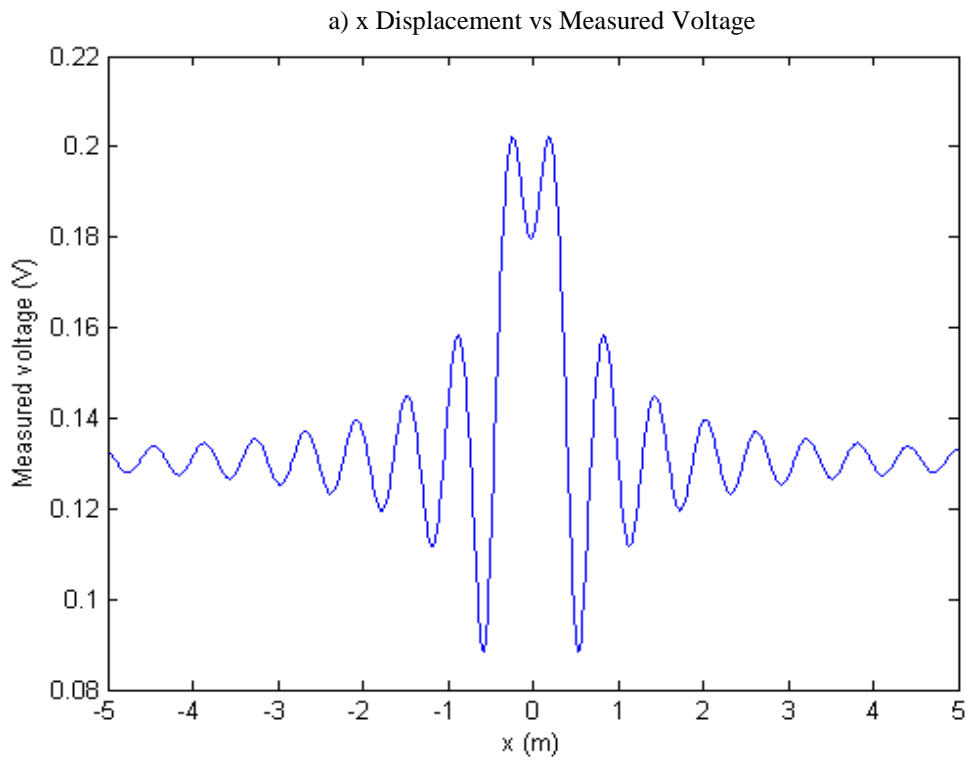


Figure 6.23: a) The graph shows x displacement versus the measured voltage for  $b = 20$  cm, probe height = 10 cm and  $f = 500$  MHz b) The graph shows x displacement versus the measured voltage for  $b = 20$  cm, probe height = 10 cm and  $f = 1$  GHz

2D plots, which are obtained above, are compared. When the frequency of the system increases, the wave pattern occurs more frequently, even though the electric field strength decreases slightly due to the increasing frequency; antenna responsivity increases with the frequency and the detected voltage increases. However, it has a better resolution. When the frequency is increased, more interference patterns are produced. Due to increase in frequency, the wavelength decreases. This results in generating more wavefronts. As a result the width of the antinode decreases.

Conversely, when the frequency of the system decreases, the wave pattern occurs less frequently, antenna responsivity decreases with the frequency and the detected voltage decreases. However, it has a worse resolution. When the frequency is decreased, less interference patterns are produced. Due to decrease in frequency, the wavelength increases. This results in generating fewer wavefronts. As a result the width of the antinode increases.

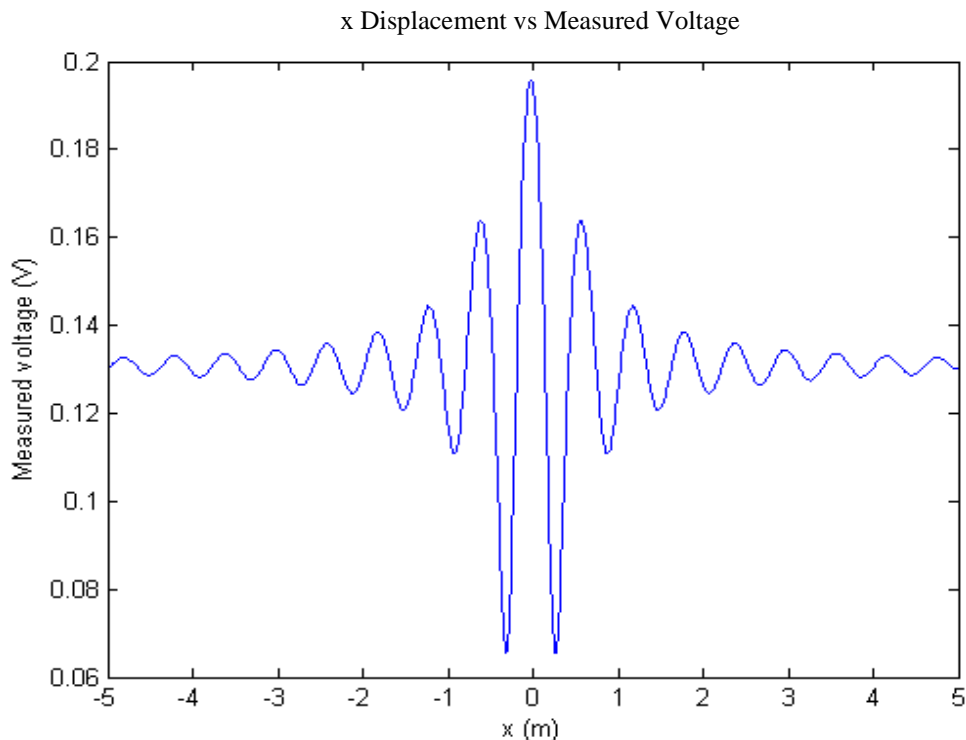


Figure 6.24: The graph shows  $x$  displacement versus the measured voltage for  $f = 500$  MHz, probe height = 10 cm and  $b = 10$  cm

By changing the depth of the cylinder from 10 cm to 100 cm, the measured voltage values ( $V_{read}$ ) are observed at a fixed frequency of  $f = 500$  MHz, radius ( $a$ ) of 5 cm and probe height of 10 cm. The following graphs show the measured voltage values at different depths. The graph in Figure 6.24 shows  $x$  axis versus  $V_{read}$  at  $b = 10$  cm. The graph in Figure 6.25 shows the same 2D plot for  $b = 50$  cm.

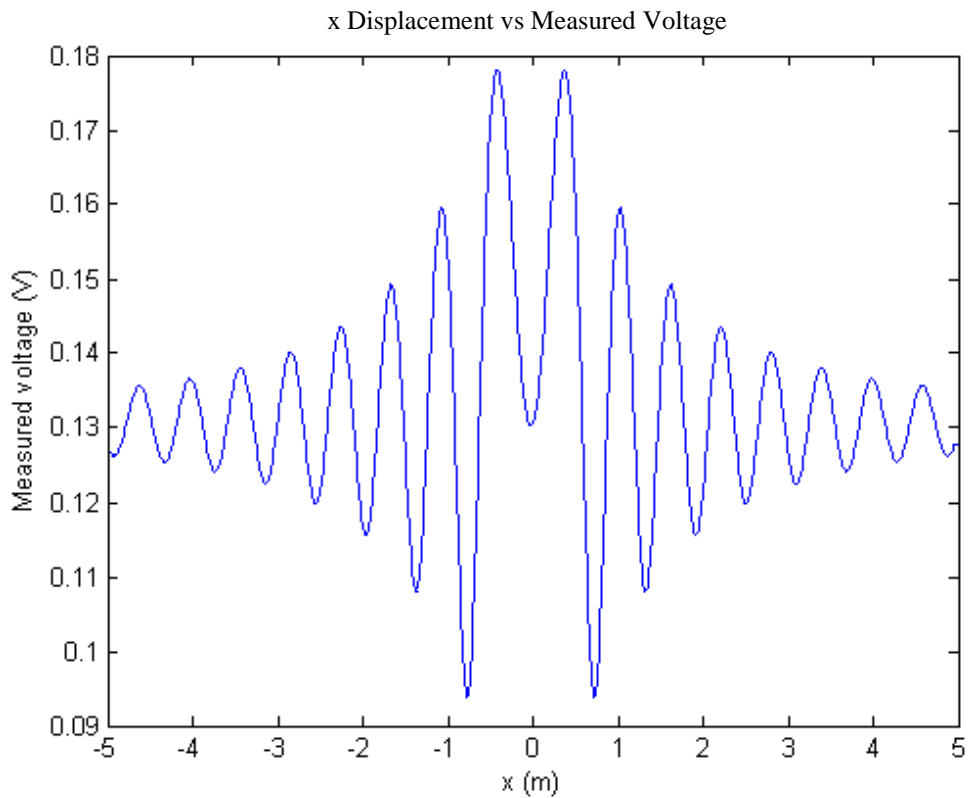


Figure 6.25: The graph shows  $x$  displacement versus the measured voltage for  $f = 500$  MHz, probe height = 10 cm and  $b = 50$  cm

The graph in Figure 6.26 also shows the same 2D plot for  $b = 100$  cm.

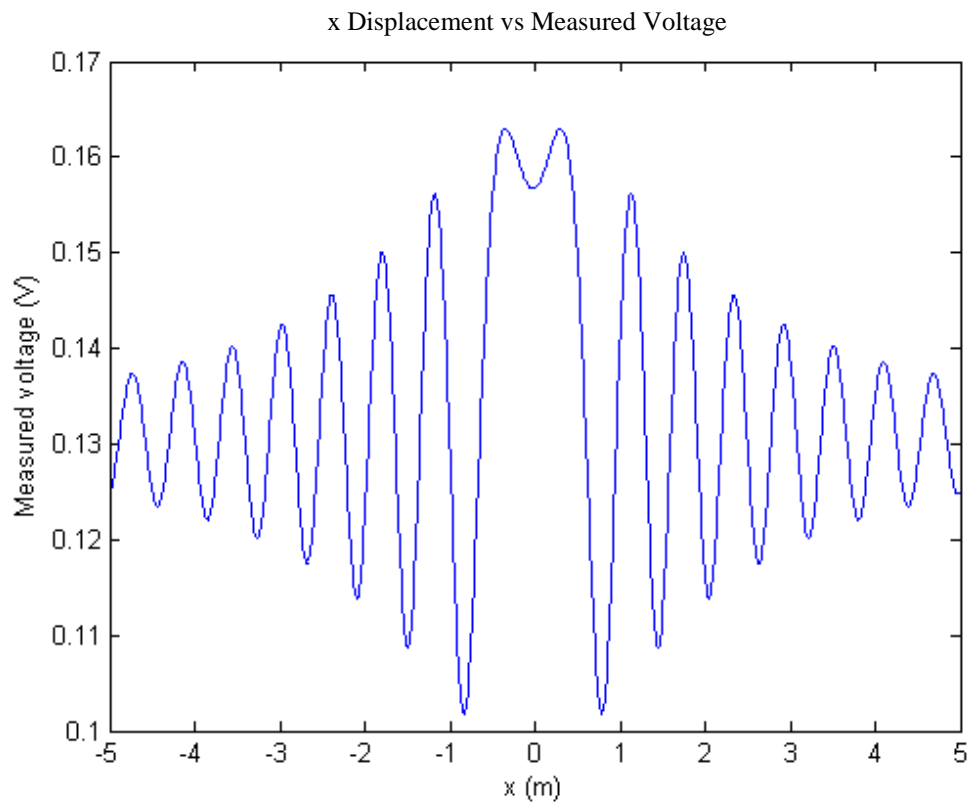


Figure 6.26: The graph shows  $x$  displacement versus the measured voltage for  $f = 500$  MHz, probe height = 10 cm and  $b = 100$  cm

2D plots, which are obtained above, are compared. The average power of the wave decreases when the depth of the target increases. The perceived voltage also decreases. Due to a decrease in interference, the width of the antinode increases. As the depth of the cylinder increases, voltage patterns' shape go from spherical to parabolic to plane wave like appearance. So at the infinity the object acts like a plane wave.

Conversely the average power of the wave increases when the depth of the target decreases. The perceived voltage also increases. Due to an increase in interference, the width of the antinode decreases.

By changing the radius ( $a$ ) of the cylinder, the measured voltage values ( $V_{read}$ ) are observed at a fixed depth of  $b = 100$  cm, frequency of  $f = 600$  MHz and probe height of 10 cm. The following graphs show the measured voltage values for different radius values. The graph in Figure 6.27 shows  $x$  axis versus  $V_{read}$  for  $b = 5$  cm.

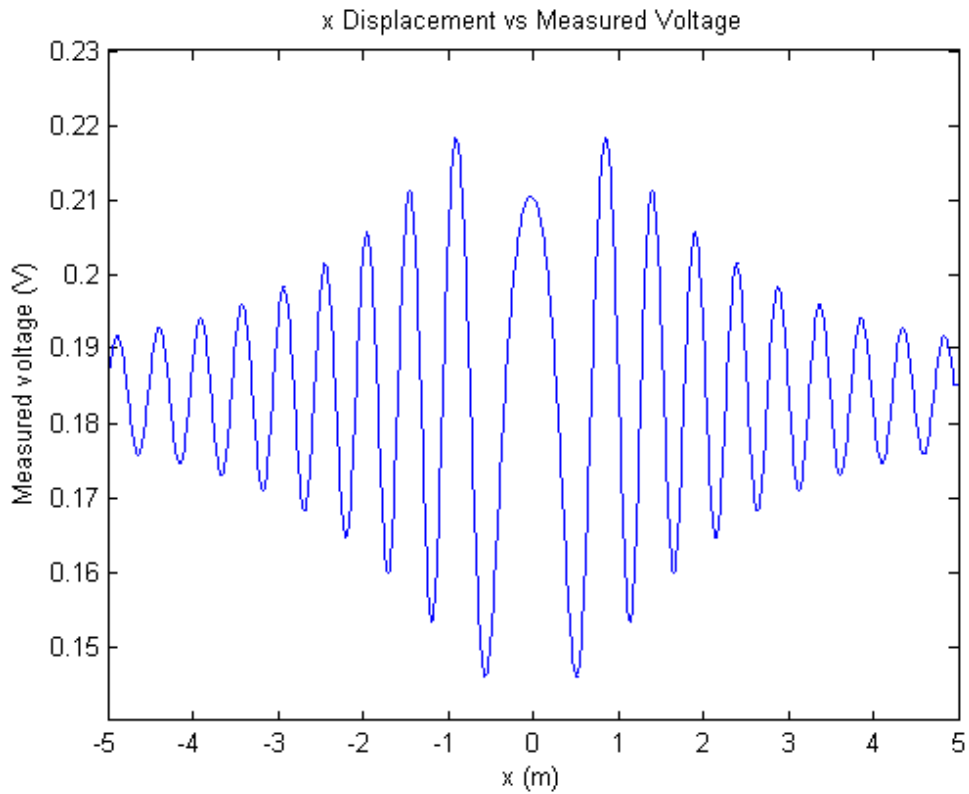


Figure 6.27: The graph shows  $x$  displacement versus the measured voltage for  $f = 600$  MHz, probe height = 10 cm,  $b = 100$  cm and  $a = 5$  cm

The graph in Figure 6.28 shows the same 2D plot for  $b = 55$  cm.

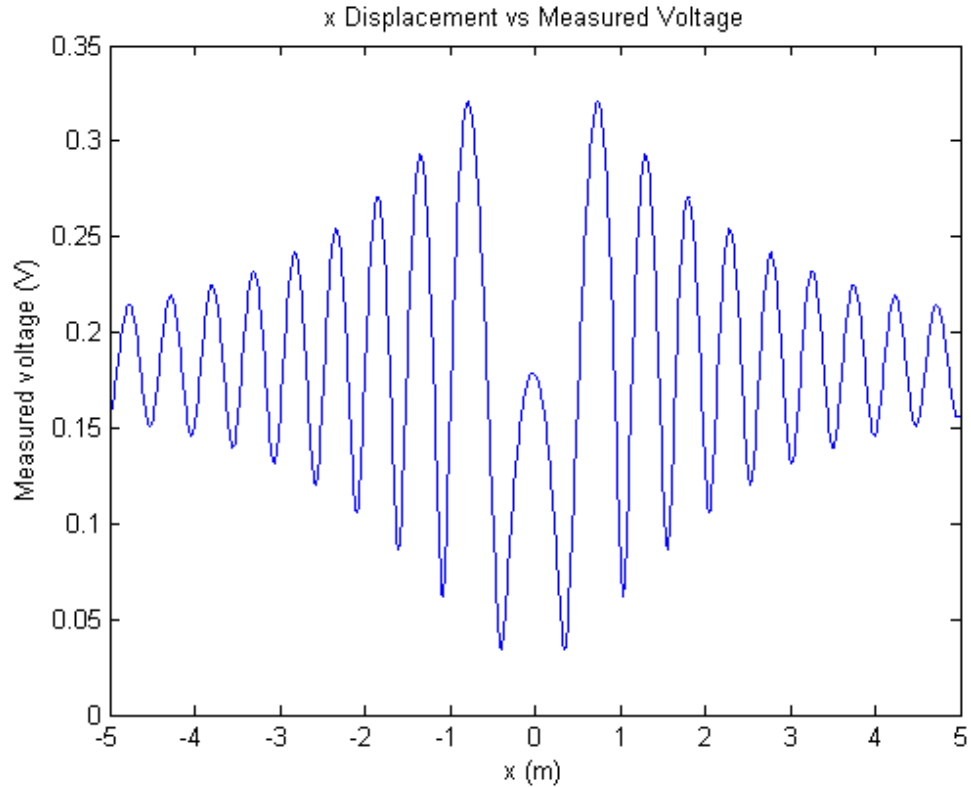


Figure 6.28: The graph shows  $x$  displacement versus the measured voltage for  $f = 600$  MHz, probe height = 10 cm,  $b = 100$  cm and  $a = 55$  cm

2D plots, which are obtained above, are compared. There exists more scattering due to target when the radius of the target increases. Due to an increase in interference, the width of the antinode decreases. As a result of this a target can be detected more easily and it is possible to make sensitive measurements. When the radius increases, there exists more attenuation. So the power of the scattered wave decreases.

Conversely, there exists less scattering due to target when the radius of the target decreases. Due to a decrease in interference, the width of the antinode increases. As a result of this a target can be detected less easily and it is harder to make sensitive measurements. When the radius decreases, there exists less attenuation. So the power of the scattered wave increases.

#### **6.4.4 Determining the Cylinder's Position**

After measuring the voltages at the electric field distribution, the cylinder's position needs to be determined. It is obtained using the 2D plots of x axis versus the measured voltage values ( $V_{read}$ ). Those plots are also related to the interference fringe patterns.

The interference fringe patterns are discovered by Young. By transmitting waves of coherent light towards the barrier, a series of interference fringe patterns are observed. The light has two slits and there is a difference between them. Those patterns help to determine whether a point in the interference fringe pattern falls into constructive (maximum or bright) zone or destructive (minimum or dark) zone.

In optics the interference fringe patterns are observed when the two light waves are superimposed. This results in higher or lower amplitude. Interference is defined as the superposition of the amplitudes of waves at any time and point. If the two waves are in phase, the amplitudes are added. This is called constructive interference. Or else if the two waves are out of phase, the amplitudes are cancelled. This is called destructive interference. Interference fringe patterns that remain stationary are coherent or correlated with each other because they either have a single frequency or come from the same source [42].

The interference fringe pattern properties are analyzed using diffraction gratings. In an interference fringe pattern, the intensity of the bright interference fringes is equal and bright. In a diffraction pattern, the intensity of the bright interference fringes is dimmer and unequal. The diffraction pattern forms the envelope of the interference fringe pattern. Both of them together define the intensity.

When the distance between the waves is small, there is less interference. Less interference means less sampled nodes and the width of the antinode increases. Conversely, when the distance between the waves is large, there is more interference. More interference means more sampled nodes and the width of the antinode decreases [42].

The purpose is to determine the cylinder's position. The voltages and the voltage variations are measured by OFS in Section 6.4.3. In order to detect the position, the interference fringe patterns are used. The position of the cylinder can be obtained by the same way from each interference fringe pattern.

The interference fringe pattern or 2D plot of x axis versus measured voltage values are obtained in Figure 6.29. It is obtained for probe height = 10 cm,  $f = 200$  MHz and  $b = 60$  cm. An example of how the position is obtained can be understood by looking at Figure 6.29. The position of the cylinder can be obtained from symmetry. The zero point is obtained from symmetry of the interference fringe patterns. This is where the cylinder is buried inside the soil.

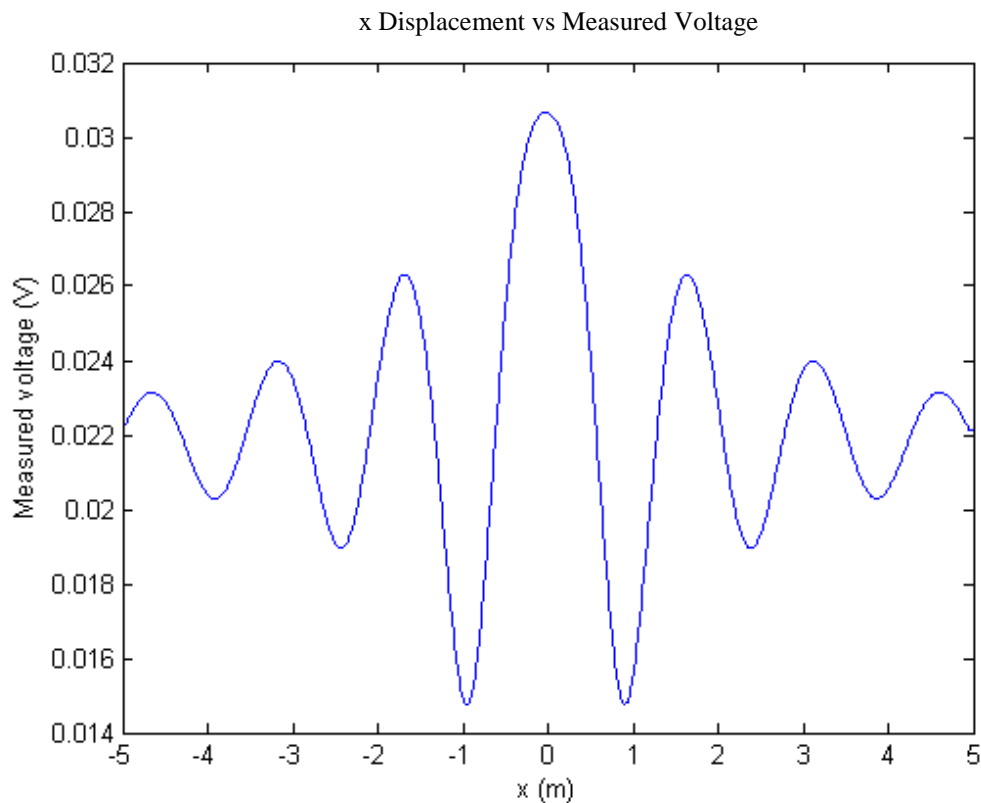


Figure 6.29: The interference fringe pattern for the values of probe height = 10 cm,  $f = 200$  MHz and  $b = 60$  cm

### 6.4.5 Determining the Cylinder's Depth

After determining the cylinder's position, the depth of the cylinder needs to be found. The voltages and the voltage variations are measured by OFS in Section 6.4.3. The depth needs to be determined using these voltage measurements. In order to detect the depth, the interference fringe patterns are used.

Due to the scattering from the interface and from the cylinder, there exists interference. This interference is related to the object's frequency, depth and antinode. Those are all related to the interference fringe patterns. Antinode is the width of the main lobe of the interference fringe pattern and it is closely related to the frequency.

As the depth of the cylinder increases, interference fringe patterns' shape go from spherical to parabolic to plane wave like appearance. So at the infinity the object acts like a plane wave. The phase at the measurement point is constant in the reflected electric field from the interface. However the phase at the measurement point in the scattered electric field from the cylinder varies as the depth changes. As the depth increases, the phase of the signal also increases. It is equal to the summation of the electric fields. The phase also changes due to frequency.

The depth of the cylinder is determined using relative amplitude, x displacement and depth relationship. When the interference fringe patterns are examined, it is observed that the relative electric field strength ratios or the relative amplitudes of the side interference fringe patterns increase as the depth of the cylinder increases. Relative amplitude is meant to be amplitude variations of side interference fringe patterns. So the side interference fringe patterns are stronger when the depth increases. This can be explained as follows. When the target is buried very near to surface, the wavefront scattered is narrower at the surface. But in deeper position, it is much wider when it reaches the surface. So that the interference fringe patterns can be observed at points further than origin. An example of this can be observed from Figure 6.30.a and Figure 6.30.b. The envelope or the change of the relative amplitudes of side interference fringe patterns is shown in black lines on the figures.

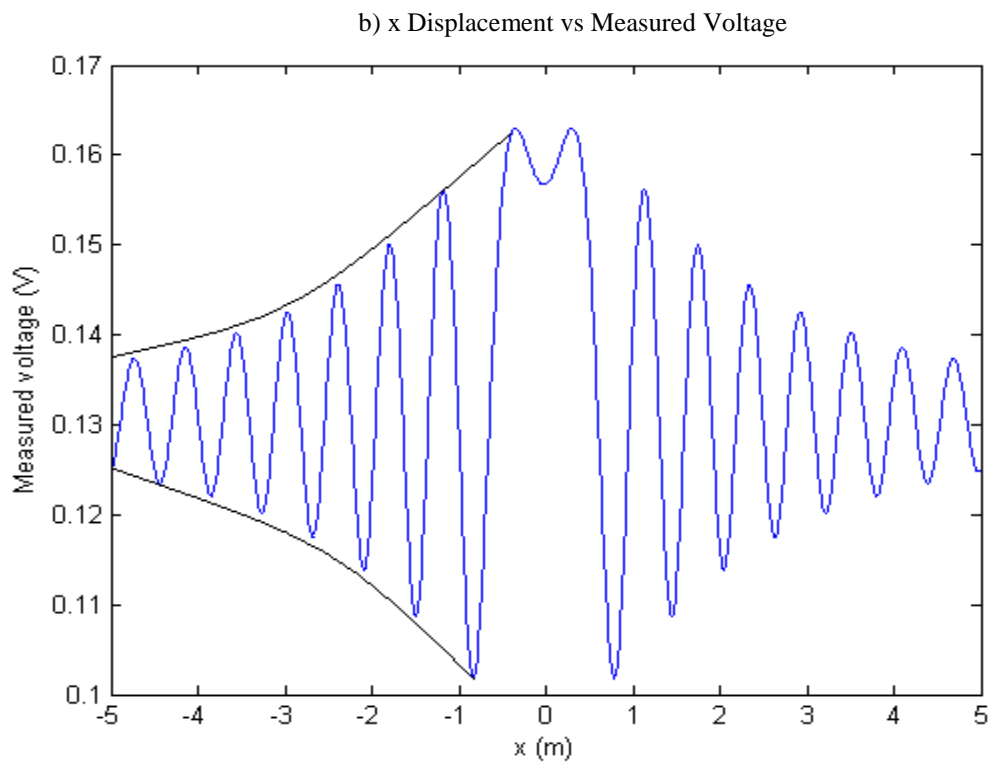
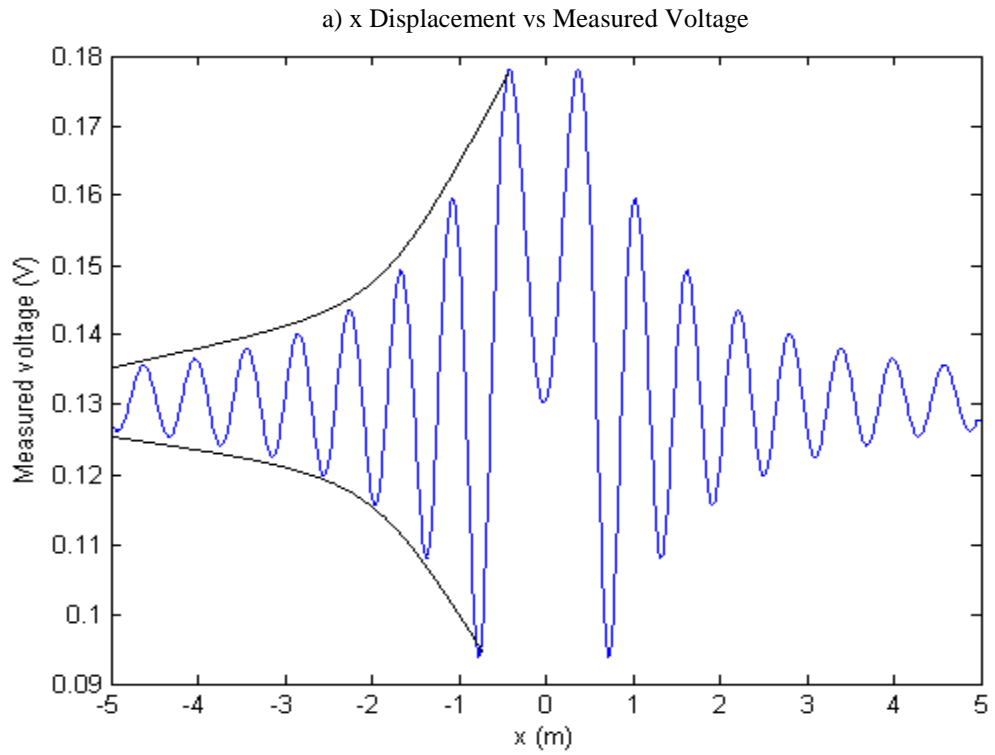


Figure 6.30: The graphs show the increase in relative amplitudes of side interference fringe patterns  
a) The interference fringe pattern for the values of probe height = 10 cm,  $f = 500$  MHz and  $b = 50$  cm  
b) The interference fringe pattern for the values of probe height = 10 cm,  $f = 500$  MHz and  $b = 100$  cm

It can be observed that as the depth increases, the relative amplitudes increase too. The plots in Figure 6.30 show x displacement versus the measured voltage values ( $V_{read}$ ) that are observed at a fixed frequency of  $f = 500$  MHz and probe height of 10 cm. The graph in Figure 6.30.a shows 2D plot for  $b = 50$  cm. The graph in Figure 6.30.b shows the same 2D plot for  $b = 100$  cm.

The relative amplitude values of the interference fringe patterns need to be obtained for each x displacement values. They are obtained by writing the MATLAB code.

The MATLAB code of the total electric field strength is explained in Section 6.4.2 and the MATLAB code of the OFS is explained in Section 6.4.3. The MATLAB code for measuring the relative amplitudes is written related to that code because the relative amplitude values are obtained from the existent interference fringe patterns.

The MATLAB code is written according to this principle. The code analyzes each of the interference fringe patterns. If the slope of the swing is positive, code continues to search for the relative amplitudes. However, if the slope of the swing is negative, code records the relative amplitude values for each x displacement values. In other words, it records the oscillation peaks of the relative amplitudes. After the relative amplitude and x displacement values are recorded, the 2D plots of x displacement versus relative amplitude (XDVRA) values are obtained for different values of frequency and depth.

After writing the code, it is executed and simulated in MATLAB package program. This code is shown in Appendix A.

#### **6.4.5.1 Simulation Results**

By changing the depth of the cylinder from 10 cm to 100 cm, the 2D plots of XDVRA values are observed at a fixed frequency, radius ( $a$ ) of 5 cm and probe height of 10 cm. Frequencies are changed from 100 MHz to 1 GHz. The obtained 2D plots are compared. As the depth of the cylinder increases, the shape of the 2D plots of XDVRA values approach to linear response. This is valid for all the frequencies.

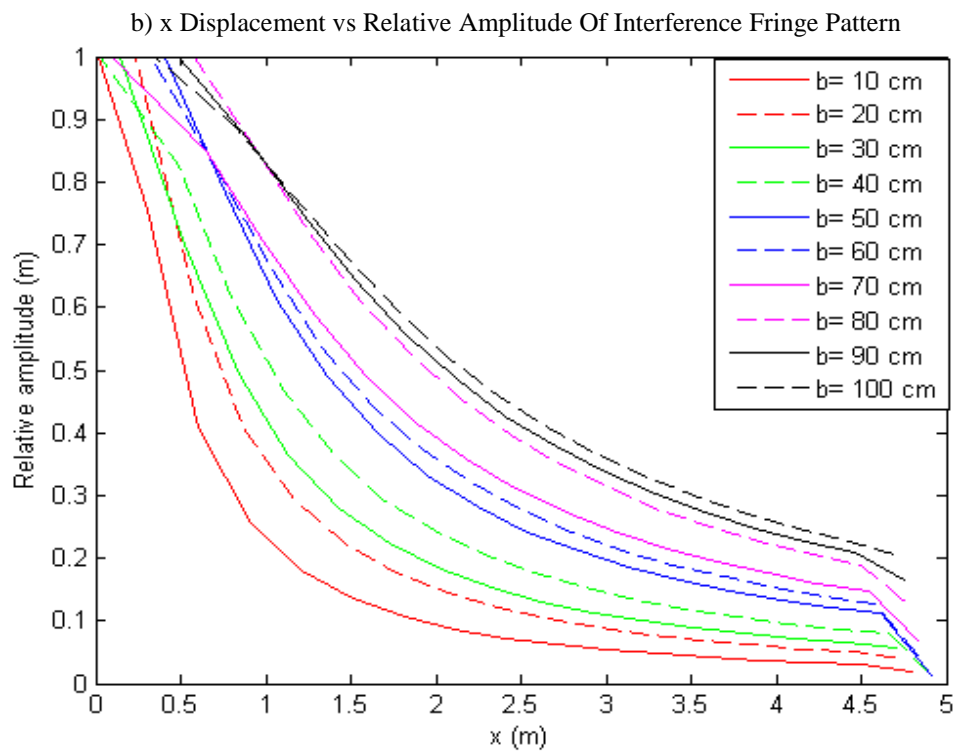
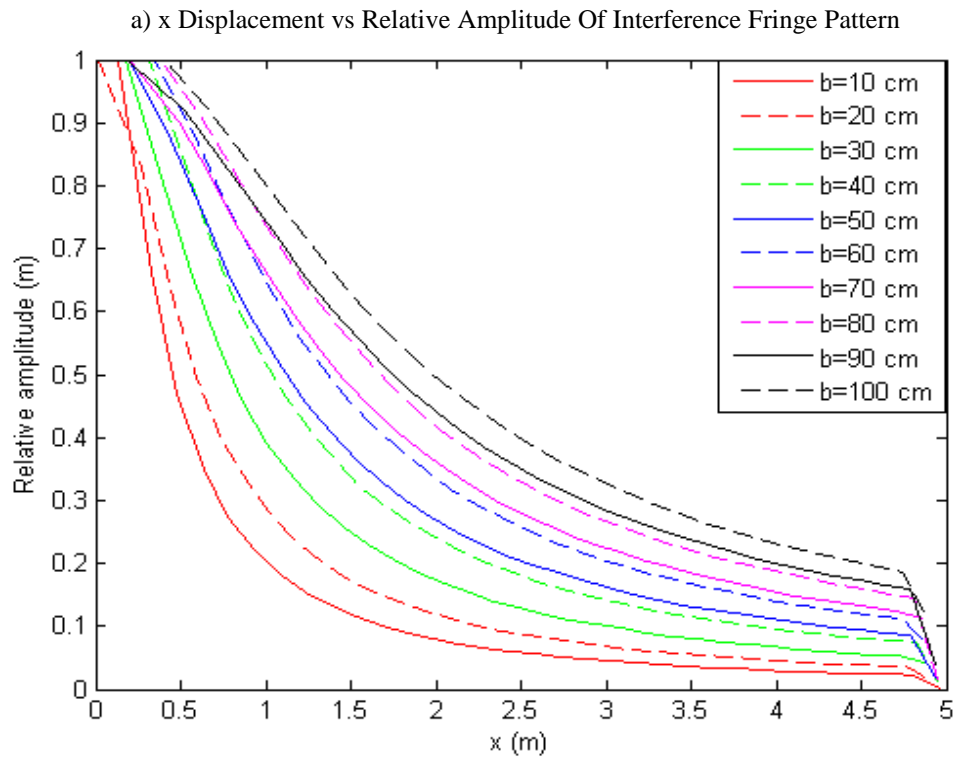


Figure 6.31: The graphs show XDVRA values for each depth from  $b = 10$  cm to  $b = 100$  cm and probe height of 10 cm a) The 2D plots are for  $f = 1$  GHz b) The 2D plots are for  $f = 500$  MHz

It can also be understood from Figure 6.31. Figure 6.31 shows 2D plots for different frequencies. The graph in Figure 6.31.a shows 2D plot for  $f = 1$  GHz. The graph in Figure 6.31.b shows the same 2D plot for  $f = 500$  MHz.

In order to detect the depth, 2D plots of XDVRA values are used. Those plots are obtained at the beginning of Section 6.4.5.1. For 10 cm of probe height and for each frequency from 100 MHz to 1 GHz, the depth is changed from 10 cm to 100 cm. For each depth, full width half maximum (FWHM) of relative amplitude's distance (x displacement) to the origin is measured from each 2D plot. How the measurement is performed is shown in Figure 6.32 below. FWHM of relative amplitude is found from the 2D plots and the x displacement to the origin that is related to that relative amplitude is recorded. Those are performed for each plot. The graph in Figure 6.32 shows XDVRA values for  $f = 1$  GHz and  $b = 10$  cm.

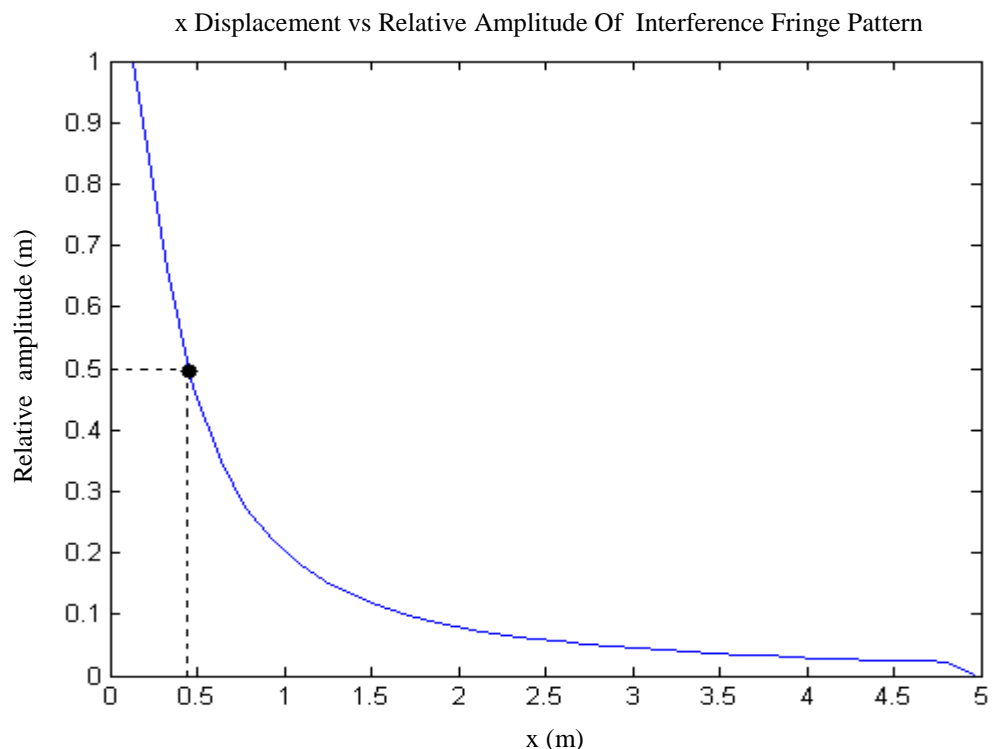


Figure 6.32: The graph shows how the measurement is performed in XDVRA graphs. It is for  $b = 10$  cm,  $f = 1$  GHz and probe height of 10 cm

The reason for considering FWHM of relative amplitude is as follows. Everything that is related to the study changes depending on the type of sensor or the type of the object. Those can include electric field strength, measured voltages and much more. Although most of the measurements are dependent, FWHM of relative amplitude does not depend on anything. The electric field strength of a signal increases at places that are near to target. FWHM of relative amplitude is not affected by type of sensor, power, sensitivity or anything.

Since those relative amplitudes are related to object's depth, depth can be determined from FWHM of relative amplitude's distance to the origin (FWHMX). Using the x displacement values that are recorded, the 2D plots of depth versus FWHMX are obtained. Those are obtained for each frequency. 2D plot for  $f = 500$  MHz is shown in Figure 6.33 and the same plot for  $f = 1$  GHz is shown in Figure 6.34.

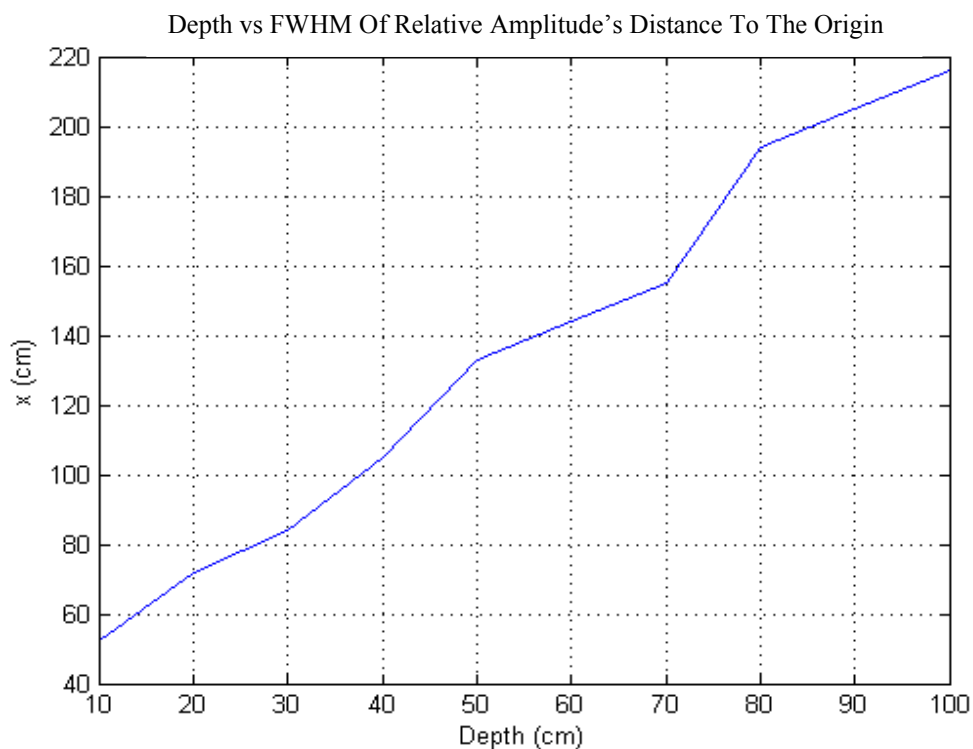


Figure 6.33: The graph shows depth versus FWHMX for probe height of 10 cm and  $f = 500$  MHz

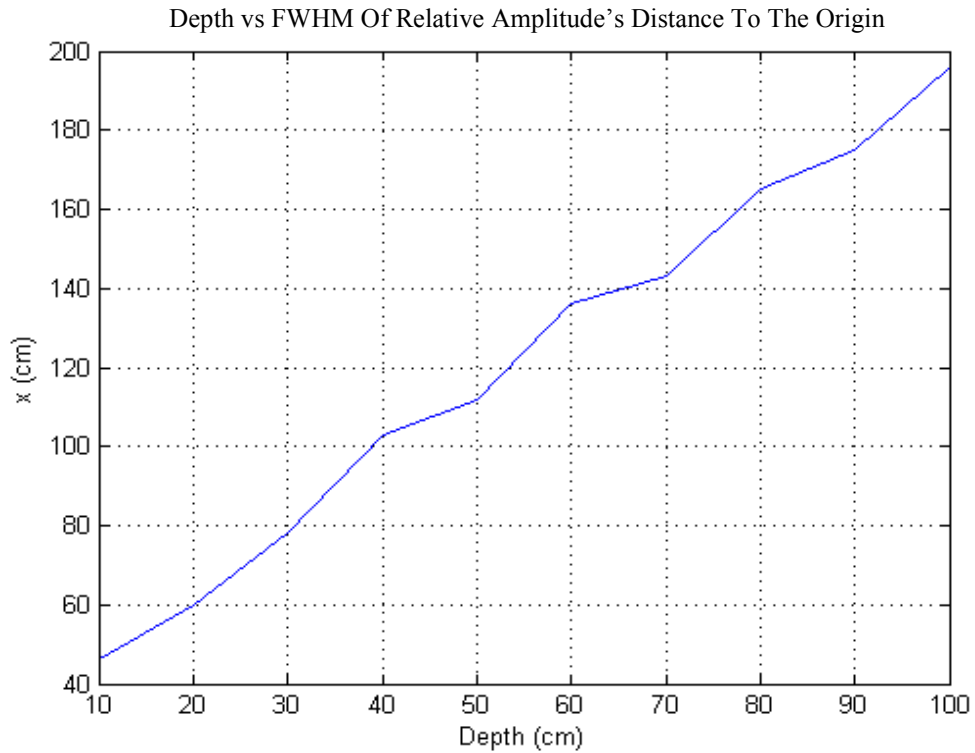


Figure 6.34: The graph shows depth versus FWHMX for probe height of 10 cm and  $f = 1$  GHz

After obtaining the 2D plots, basic linear fitting is performed in MATLAB program to obtain the equations for each 2D plot. The equation of Figure 6.33 is obtained as

$$FWHM_X = 0.52b - 16.2 \quad (6.14)$$

The equation of Figure 6.34 is obtained as

$$FWHM_X = 0.6b - 17.8 \quad (6.15)$$

So for  $f = 500$  MHz, the depth can be determined from Equation 6.14 if FWHMX is known. And for  $f = 1$  GHz, the depth can also be determined from Equation 6.15 if FWHMX is known. So knowing frequency and FWHMX values, the depth can be

determined. It is observed that as the depth of the target increases at a fixed frequency, FWHMX increases too.

The depth is proportional to FWHMX and frequency does not have a large effect on the depth. Combining Equation 6.14, Equation 6.15 and frequency relationship, a new equation is obtained. It is written as

$$Depth = b \cong \left(0.68 - \frac{0.08}{f_{GHz}}\right) \times FWHMX + \left(-19.4 + \frac{1.6}{f_{GHz}}\right) \quad (6.16)$$

The depth can be determined easily using Equation 6.16 if the frequency and the FWHMX values are known.

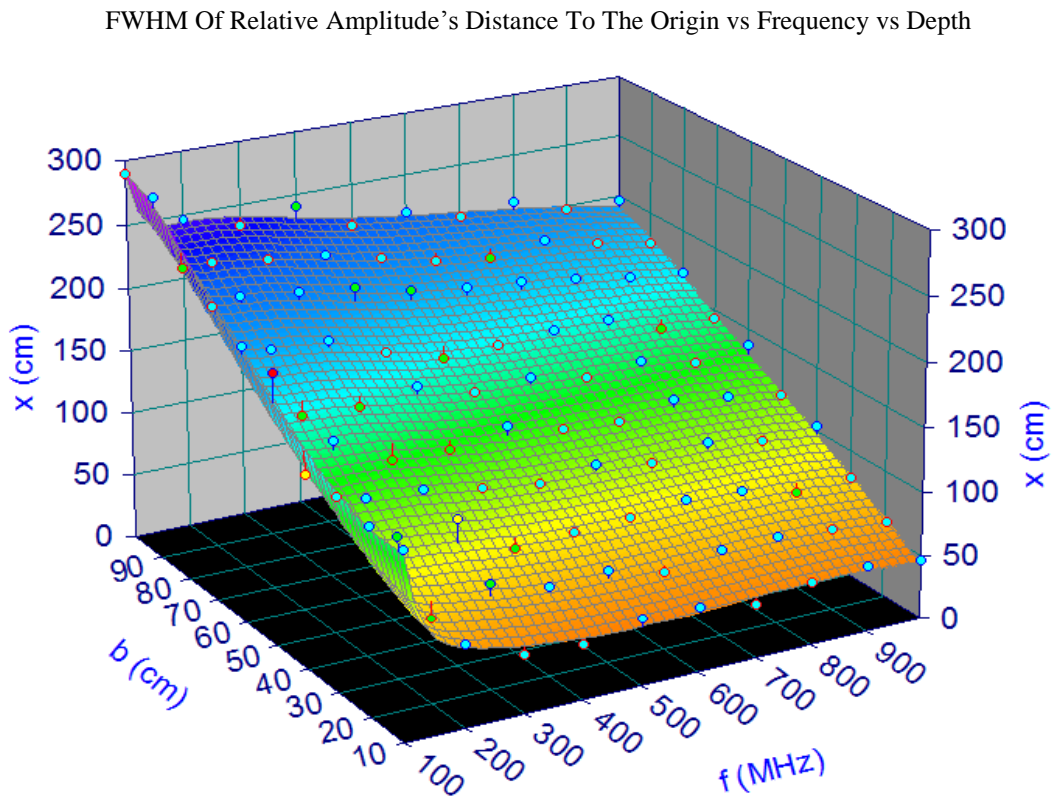


Figure 6.35: The graph shows frequency versus depth versus FWHMX for probe height of 10 cm and radius ( $a$ ) of 5 cm

Using all the x displacement values that are recorded, the 3D plot of frequency versus depth versus FWHMX is obtained. It is obtained for 10 cm of probe height and 5 cm of cylinder radius ( $a$ ). The 3D plot is obtained in MATLAB program. For obtaining smoother plots, basic fitting is performed using TableCurve 3D v4.0.01 program. TableCurve 3D v4.0.01 is a software application that is used to surface fit large amount of equations. It offers numerical and graphical assistance for choosing the appropriate model for the problem. The smoother basic fitted 3D plot is shown in Figure 6.35.

It is observed from the 3D basic fitting plot that as the depth increases at a fixed frequency, FWHMX increases. There is a relationship among frequency, depth and FWHMX.

After obtaining the 3D basic fitting plot, the equation for that is obtained using TableCurve 3D v4.0.01 program. This program gives equations that best fits to the 3D plots. So the simplest equation is Chebyshev LnX,Y Bivariate Polynomial Of Order 5. The expansion of this equation is written as

$$\begin{aligned}
 z = & a + bT_1(x') + cT_1(y') + dT_2(x') + eT_1(x')T_1(y') + fT_2(y') + gT_3(x') \\
 & + hT_2(x')T_1(y') + iT_1(x')T_2(y') + jT_3(y') + kT_4(x') \\
 & + lT_3(x')T_1(y') + mT_2(x')T_2(y') + nT_1(x')T_3(y') + oT_4(y') \\
 & + pT_5(x') + qT_4(x')T_1(y') + rT_3(x')T_2(y') + sT_2(x')T_3(y') \\
 & + tT_1(x')T_4(y') + uT_5(y')
 \end{aligned}
 \tag{6.17}$$

where

$$x' : \ln(x) \text{ scaled } -1 \text{ to } 1, y' : y \text{ scaled } -1 \text{ to } 1, T_n(x') = \cos(n \arccos(x'))$$

It has a regulation of 2 % or less. The coefficients of the equation are written as

$$\begin{aligned}
a = 151.1, b = -33.12, c = 85.99, d = 8.556, e = -4.468, f = 0.916, g = -7.464, \\
h = -8.657, i = -3.788, j = -2.278, k = 4.601, l = 0.949, m = 2.641, n = 3.117, \\
o = -0.696, p = -3.308, q = 0.694, r = -1.604, s = -1.558, t = 0.041, u = -0.764.
\end{aligned}
\tag{6.18}$$

So by obtaining the coefficients, the equation can be obtained by putting them into Equation 6.17. Then the depth can be easily obtained knowing the frequency and FWHMX.

## 6.5 Accounting for Noise in the System

In the GPR system that is used in the study, there is not any noise added to the system up to now. So noise should be added to some of the OFSIS elements. Before adding the noise to the system, the noise of the OFSIS needs to be determined.

### 6.5.1 Extracting Noise of the System from OPTIWAVE

OPTIWAVE program is used to determine the noise in the OFSIS or the receiving system. Noises mostly arise from the modulator and the photodiode in the system. Noise from laser does not affect the system. Optical receivers convert incident optical power into electric current by a photodiode. The conversion from light to electric current is cohabited with the addition of noise. The shot noise and the thermal noise are the main noise mechanisms which lead to current changes.

Shot noise takes its name from electric current that is made up of stream of discrete charges which are the electrons. Those electrons are generated at random times. Even if the incident optical power does not change, there exist current changes due to randomly generated electron-hole pairs. Shot noise depends on the incident power or the laser power. A good system must not be operated at shot noise [43], [44]. Mathematically, mean square of shot noise current in PIN photodiode is determined as

$$\langle i_{sn}^2 \rangle = 2qR_{res}P_{opt}B = 2qi_{signal}B \tag{6.19}$$

where

$q$  = electron charge unit,  $R_{res}$  = responsivity,  $P_{opt}$  = optical power,  $i_{signal}$  = the current detected and  $B$  = bandwidth.

The current detected is the summation of the average current generated by the detector and the dark current. Dark current cohabits with thermal generated carriers which do not have light illumination.

APD can be thought as a PIN photodiode with a gain. Also, mean square of shot noise current in APD is determined as

$$\langle i_{sn}^2 \rangle = 2qM^2FR_{res}P_{opt}B = 2qM^2Fi_{signal}B \quad (6.20)$$

where

$M$  = gain and  $F$  = excess noise factor.

Electrons move randomly at any finite temperature in any conductor. Even if there is no voltage applied, the currents fluctuate due to thermal motion of electrons. The load resistor adds those fluctuations to the current. Thermal noise (Johnson noise or Nyquist noise) arises in load resistor of photodiode circuit due to thermal motion of electrons. If there is not any special condition given, system must be operated at thermal noise. Thermal current noise has zero average value [43], [44]. Mathematically, mean square of thermal noise current in PIN photodiode is written as

$$\langle i_T^2 \rangle = \frac{4k_BTB}{R_L} \quad (6.21)$$

where

$k_B = 1.381 \times 10^{-23}$  J/K = Boltzmann constant,  $T$  = absolute temperature and  $R_L$  = resistance of loading resistor.

APD can be thought as a PIN photodiode with a gain but mean square of thermal noise current in APD is the same as mean square of thermal noise current in PIN photodiode.

### 6.5.1.1 Determining Noise of the System without Filtering

Shot or thermal noise deteriorates receivers or photodetectors performance. The system operates as thermal noise limited. Noise mostly arises from the PD in the system. Noise from laser does not affect the system.

First of all, the noise on the PD needs to be extracted. This is performed without filtering. After obtaining the noise, it needs to be added to the measured voltages at the OFS which is obtained due to the effect of optical modulator. How the measured voltages ( $V_{read}$  or  $V_{seen}$ ) are obtained is explained in Section 6.4.3 before.

The light coming out of the OFS is written as

$$Light_{out} = Intensity \times \left[ 1 + \sin\left(\frac{V_{seen}}{V_{\pi}}\right) \right] = Intensity \times \left[ 1 + \left(\frac{\pi V_{seen}}{V_{\pi}}\right) \right] \quad (6.22)$$

where  $V_{seen} < V_{\pi}$ .

Intensity shows the incoming light power to the OFS. If Equation 6.22 is observed, it is seen that voltage affects the intensity. The ratio of  $V_{seen}$  to  $V_{\pi}$  varies in different types of OFSs.

The noiseless output voltage of PD is written as

$$V_{PDout} = R_{res} \times Intensity \times \left[ 1 + \left(\frac{\pi V_{seen}}{V_{\pi}}\right) \right] \times R_L \quad (6.23)$$

The value of the responsivity of PD is taken as 1 A/W and the maximum value of it is 1. Intensity or laser output value is taken as 1mW [43], [44]. This value can be less

than the value of the responsivity. The terms in parenthesis show the effect of the coupled voltage of the OFS on modulation. The value of the resistance of the loading resistor is taken as 1 k $\Omega$  because there exists current and the voltage needs to be increased. After putting those values into Equation 6.23, the equation is obtained as

$$V_{PDout} \cong \frac{\pi V_{seen}}{V_{\pi}} \quad (6.24)$$

The thermal noise output voltage at PD can be obtained from Equation 6.21. After putting in the values into Equation 6.21 also, the equation is obtained as

$$V_{PDnoise} = 4k_B T B \quad (6.25)$$

The thermal noise output voltage at PD is measured using OPTIWAVE program. The amplitude of the noise is obtained as 30nV.

So for a good measurement to be performed, the value of the noiseless output voltage of PD must be greater than the value of the thermal noise output voltage at PD. This needs to be satisfied because the noiseless signal must not be lost inside the noise. The obtained values are achieved for the system without filtering. The noise is not added to the output voltages of the PD. This is performed when there is filtering. It is shown in Section 6.5.1.2 [43], [44].

### **6.5.1.2 Determining Noise of the System with Filtering**

Noise needs to be added to measured voltages at OFS. Before adding the noise to the system, the noise of the OFSIS needs to be extracted using OPTIWAVE program.

Noise mostly arises from the PD and the modulator in the system. Noise from laser does not affect the system. First of all, the effect of the modulator needs to be obtained using OPTIWAVE program. Then the noise on the PD needs to be determined. This is performed when there is filtering. After obtaining the noises, they need to be added to the measured voltages at the OFS which is obtained due to the

effect of optical modulator. How the measured voltages ( $V_{read}$  or  $V_{seen}$ ) are obtained is explained in Section 6.4.3 before.

The OFSIS is set up in OPTIWAVE program. The setting configuration or the screen capture of it is shown in Appendix B.

CW laser has power of 0 dBm, dynamic noise of 3 dB and noise threshold of -100 dB. Optical fibers have a length of 50 m. Mach-Zehnder modulator has an extinction loss of 30 dB and an average loss of 3 dB. APD's gain value is 3. It has responsivity of 1 A/W, ionization ratio of 0.9, dark current of 10 nA and thermal noise of  $10^{-22}$  W/Hz. PIN photodiode has responsivity of 1 A/W, dark current of 10 nA and thermal noise of  $10^{-22}$  W/Hz. Laser signal passes through the modulator. It is observed from the OPTIWAVE program that PIN photodiode has a noise of 20  $\mu$ W and APD has a noise of 100  $\mu$ W. The measured voltages at the OFS are saved as data files in MATLAB program. Those are named as  $V_{read}$ . They are saved into a file in order to make modulation. Those MATLAB datas are loaded in OPTIWAVE to obtain the incoming signals. The loaded incoming signals are modulated at the OFS. The modulated signals travel through optical fiber to the PD.

As it is mentioned many times before, noise mostly arises from the PD and the modulator in the system. Noise needs to be added to the measured voltage signals at OFS.

The measured voltage signals are named as  $V_{read}$  before. Those are the incoming electrical signals. The electrical signal needs to be multiplied by a factor so that the modulated signal is obtained. The incoming signals travel through optical fiber to the modulator. After modulation they again travel through optical fiber to the PD. Those signals are named as  $V_{readout}$ . This ratio gives the multiplication factor. So using the OPTIWAVE program, it is observed that the amplitude of  $V_{read}$  varies between 280 mV to 30 mV and it has peak to peak value of 250 mV. It is also observed that the amplitude of  $V_{readout}$  varies between 0  $\mu$ V to 380  $\mu$ V and it has peak to peak value of 380  $\mu$ V. So by dividing the peak to peak values, the multiplication factor is

obtained nearly 1.5 m. The effect of the modulation is the multiplication of the incoming electrical signal by 1.5 m.

After observing the effect of modulation, the noise of APD needs to be extracted. APD is used to determine the noise at the PD. Low pass Gaussian filter (LPGF) is used before APD. It has an order of 5, a depth of 40 dB and an insertion loss of 1. So the noise of the APD with filtering is determined using OPTIWAVE program. The noise is observed from the oscilloscope output of APD in OPTIWAVE. The amount of noise that APD contains changes with frequency. For each frequency between 100 MHz to 1 GHz, the noise values are obtained. The noise values of APD for different frequency values are shown in Table 6.1 below.

Table 6.1: The noise values of APD for different frequency values

| Frequency (f)    | 100 MHz     | 200 MHz     | 300 MHz     | 400 MHz     | 500 MHz   | 600 MHz     | 700 MHz     | 800 MHz     | 900 MHz     | 1 GHz     |
|------------------|-------------|-------------|-------------|-------------|-----------|-------------|-------------|-------------|-------------|-----------|
| Noise ( $\mu$ W) | 0.2 $\mu$ W | 0.4 $\mu$ W | 0.6 $\mu$ W | 0.8 $\mu$ W | 1 $\mu$ W | 1.2 $\mu$ W | 1.4 $\mu$ W | 1.6 $\mu$ W | 1.8 $\mu$ W | 2 $\mu$ W |

Using the obtained noises in OPTIWAVE program, the total noise can be added to the measured voltage signals as follows

$$V_{detect} = 1.5 m * V_{read} + Noise_{APD} (W) \quad (6.26)$$

where

$Noise_{APD}$  = Noise of APD.

The units of the measured voltages are in terms of Volts. However, the units of the noise values are in terms of Watts. This can be seen from Table 6.1. So the noise values need to be converted into units of Volts. Then Table 6.1 is modified and rewritten as Table 6.2. Then the modified noise values of APD for different

frequency values are obtained in Table 6.2 below. Table 6.2 also shows the receiver sensitivity values for each frequency. Receiver sensitivity is the lowest power that the receiver can achieve in order to realize the incoming signals. It is also equal to the transmitter's power in dBm.

Table 6.2: The modified noise and the receiver sensitivity values of APD for different frequencies

| Frequency (f)              | 100 MHz | 200 MHz | 300 MHz | 400 MHz | 500 MHz | 600 MHz | 700 MHz   | 800 MHz | 900 MHz   | 1 GHz   |
|----------------------------|---------|---------|---------|---------|---------|---------|-----------|---------|-----------|---------|
| Noise (mV)                 | 0.32 mV | 0.45 mV | 0.55 mV | 0.63 mV | 0.71 mV | 0.77 mV | 0.84 mV   | 0.89 mV | 0.95 mV   | 1 mV    |
| Receiver Sensitivity (dBm) | -87 dBm | -84 dBm | -82 dBm | -81 dBm | -80 dBm | -79 dBm | -78.5 dBm | -78 dBm | -77.4 dBm | -77 dBm |

OFSs are superior to radio receivers because they have much lower noise figures compared to RF systems [43]. Using the obtained noises in OPTIWAVE program, the total noise (in terms of Volts) can be added to the measured voltage signals as follows

$$V_{detect} = V_{read} + Noise_{APD} (V) \quad (6.27)$$

where

$Noise_{APD}$  = Noise of APD.

So the measured voltage signals or the electrical field voltages occurring sensed at OFS are named as  $V_{read}$ . After modulating and adding the noises to measured voltage signals, the obtained signals are equal to the photodetected sensor voltage signals. Those are named as  $V_{detect}$ . The first term in Equation 6.27 shows the modulated signal. The last term shows the noise of APD.  $Noise_{APD}$  depends on the frequency values. As the frequency changes, noise of APD also changes. The noise values are shown in Table 6.2.

## 6.5.2 Adding Noise to the System in MATLAB

After modulating and adding the noises to the measured voltage signals, the photodetected sensor voltage signals can be obtained. Those are explained in Section 6.5.1.2. More specifically they are obtained using Equation 6.27. The noise can be added to the measured voltage signals using Equation 6.27. MATLAB program is used to obtain  $V_{\text{detect}}$ .

The plots of  $x$  displacement versus measured voltage values are obtained in Section 6.4.3. Those are obtained by changing the values of frequency and depth. Using the plots in Section 6.4.3, the data is extracted from each MATLAB figure. Then the data is obtained for each  $V_{\text{read}}$ . After extracting the datas,  $V_{\text{detect}}$  is obtained using Equation 6.27. It is obtained for fixed probe height and different values of frequency and depth.

### 6.5.2.1 Simulation Results

By changing the depth of the cylinder from 10 cm to 100 cm, the 2D plots of photodetected sensor voltage signals are observed at a fixed frequency, radius ( $a$ ) of 5 cm and probe height of 10 cm. Frequencies are changed from 100 MHz to 1 GHz. The operating frequency of the system is taken between 100 MHz to 1 GHz. The reason of this is as follows. When the frequency is lower than 100 MHz, the antenna cannot collect the signals. When the frequency is higher than 1 GHz, surface roughness will create scattering interference patterns.

The following figures include two plots. First one shows  $x$  displacement versus measured voltage values. Second one shows  $x$  displacement versus photodetected voltage values. Figure 6.36 shows the 2D plots for  $f = 200$  MHz and  $b = 10$  cm. Figure 6.37 shows the same plots for  $f = 200$  MHz  $b = 100$  cm.

Figure 6.38 shows the same 2D plots for  $f = 1$  GHz and  $b = 10$  cm. Figure 6.39 also shows the same 2D plots for  $f = 1$  GHz and  $b = 100$  cm.

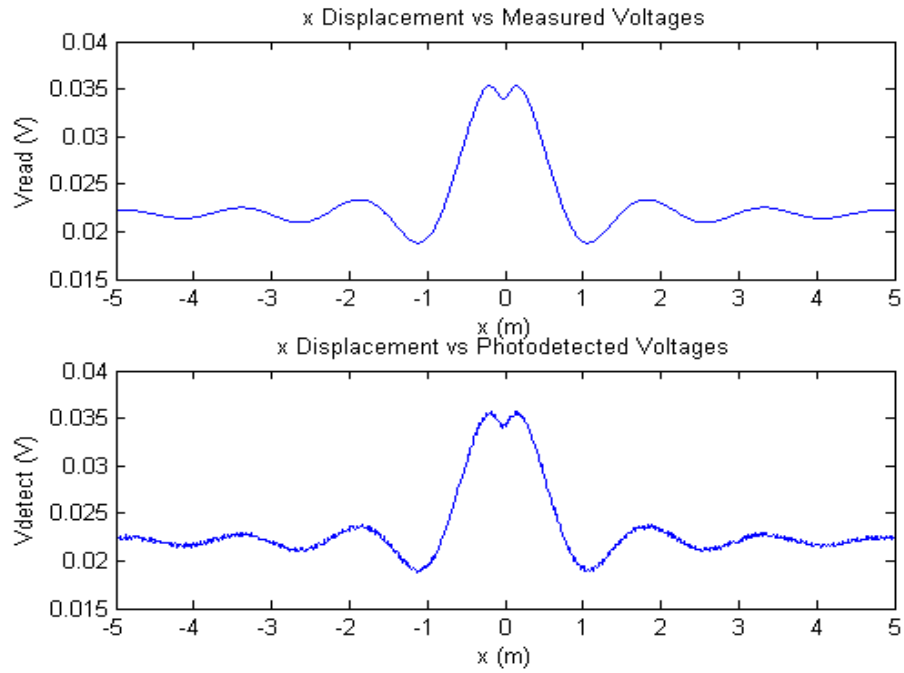


Figure 6.36: First graph shows  $x$  displacement versus measured voltage values and second graph shows  $x$  displacement versus photodetected voltage values for  $f = 200$  MHz and  $b = 10$  cm

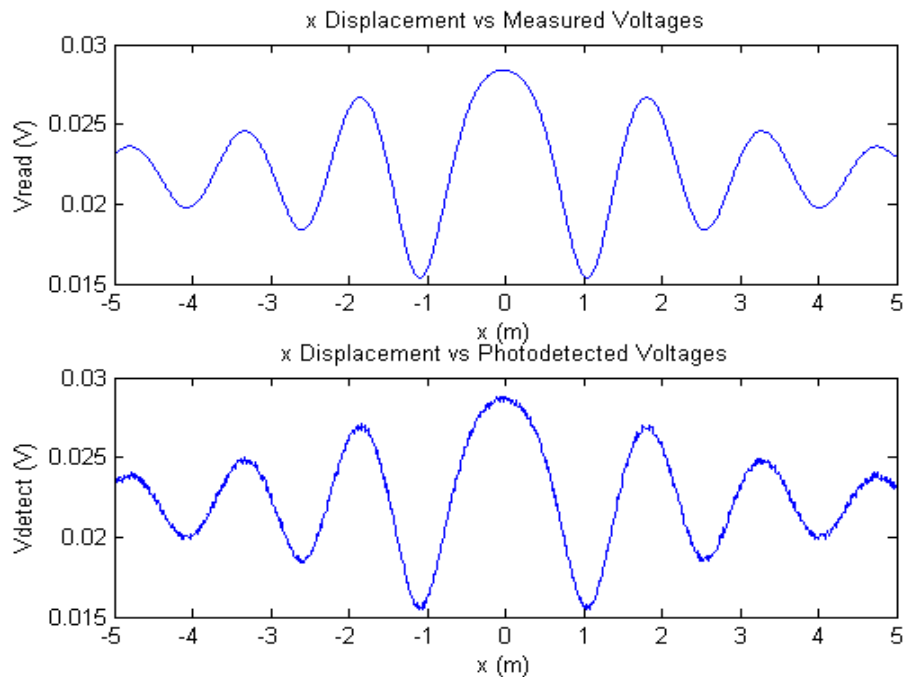


Figure 6.37: First graph shows  $x$  displacement versus measured voltage values and second graph shows  $x$  displacement versus photodetected voltage values for  $f = 200$  MHz and  $b = 100$  cm

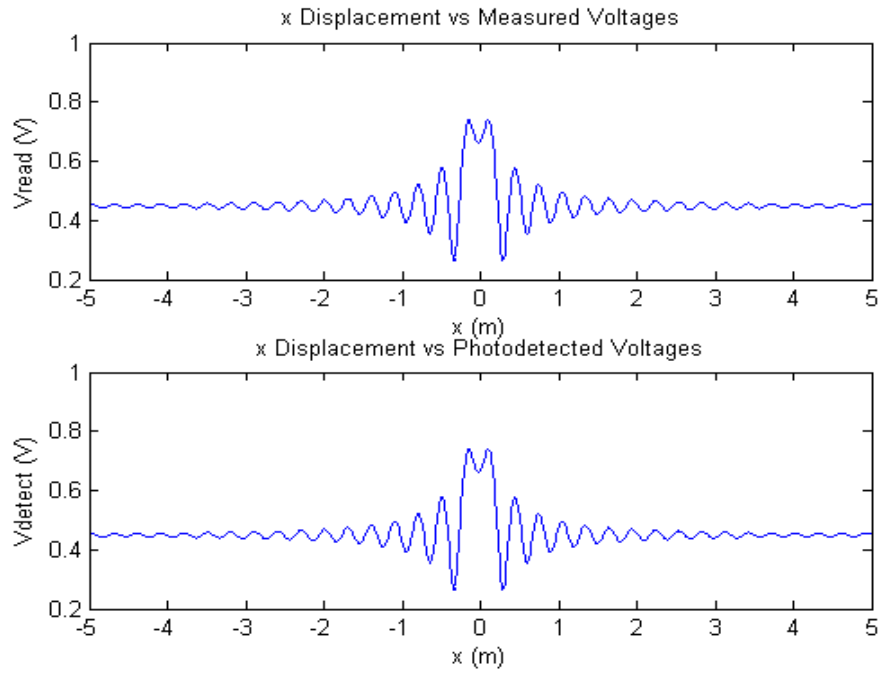


Figure 6.38: First graph shows  $x$  displacement versus measured voltage values and second graph shows  $x$  displacement versus photodetected voltage values for  $f = 1$  GHz and  $b = 10$  cm

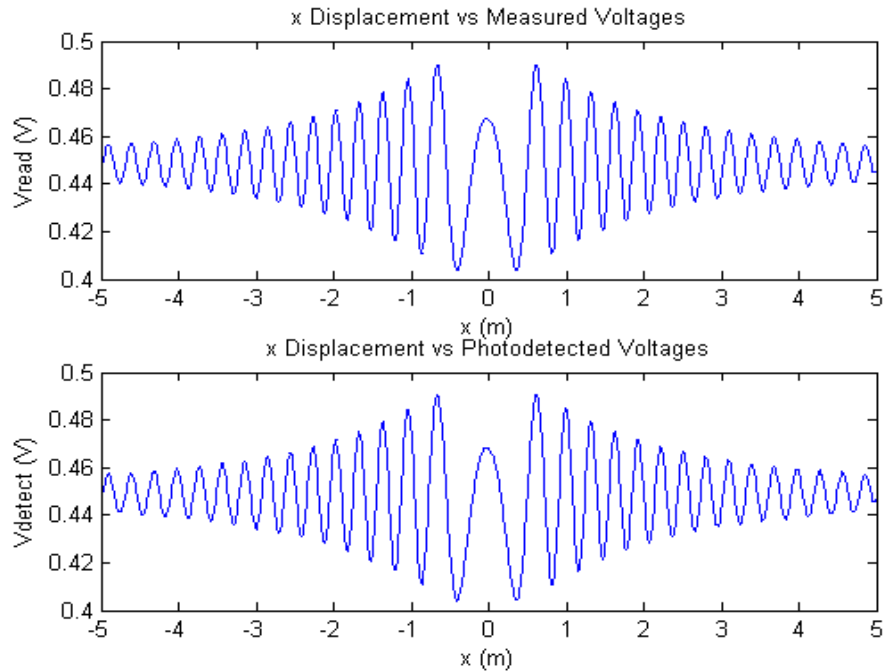


Figure 6.39: First graph shows  $x$  displacement versus measured voltage values and second graph shows  $x$  displacement versus photodetected voltage values for  $f = 1$  GHz and  $b = 100$  cm

Noise affects the transmitter's minimum power. This power needs to be greater than a limit. The limit that is used in the study is 3 dB. So noise limits the minimum power that is used and the effects of noise depend on frequency and depth values. It can be observed from Figure 6.36 to Figure 6.39, noise does not have an observable effect on the intervals of frequency and depth measurements that are performed in the study. OFSIS has a good noise performance that it works properly in all of the frequency and depth ranges that are used in the study. OFSIS has little noise when compared to the other systems. OFSIS is also superior to radio receivers because they have much lower noise figures compared to RF systems [43].

In order to determine the depth limit at a fixed frequency, the SNR (signal to noise ratio) values of the Figure 6.36 to Figure 6.39 need to be obtained. The depth limit shows how far the wave can propagate inside the martian soil at a fixed frequency. This needs to be performed for a limit of 3 dB. The maximum swing (distance between maximum and minimum) voltage variation is measured in each of the graph to determine the signal voltage part of the SNR. The SNR values are determined from

$$SNR = 20 \log_{10} \left( \frac{\text{signal voltage}}{\text{noise voltage}} \right) \quad (6.28)$$

The voltage variations are obtained as shown in Figure 6.40. The black dots show the maximum swing (distance between maximum and minimum) voltage variation.

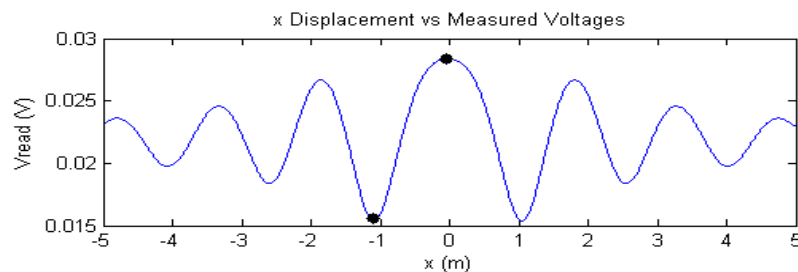


Figure 6.40: The graph shows an example of the smallest voltage variation

The noise values are obtained from Table 6.2. The amount of noise that APD contains changes with frequency. After knowing both signal and noise voltage values, SNR can be determined easily.

The SNR values for Figure 6.36 to Figure 6.39 are obtained using Equation 6.28. The frequency and the related SNR values are shown in Table 6.3.

Table 6.3: The SNR values for  $f= 200$  MHz and  $f= 1$  GHz

| Frequency( $f$ )    | 200 MHz | 1 GHz |
|---------------------|---------|-------|
| SNR (dB) $b=10$ cm  | 30.5 dB | 53 dB |
| SNR (dB) $b=100$ cm | 28.5 dB | 38 dB |

The difference between the signal and the noise needs to be 3 dB. A rough estimate for the measurable depth limit for martian soil is written related to this difference. It is obtained as

$$Depth\ Limit\ (m) = \frac{SNR - 3\ dB}{x\ dB/m} \quad (6.29)$$

where

$x$  = distance or depth.

The depth limits for frequencies 200 MHz and 1 GHz are obtained using Equation 6.29. This rough estimate is obtained from the relationship between depths and SNRs. The depth limit for 1 GHz is 2.1 m. This means that the wave can propagate an addition of 2.1 m after the depth of 100 m. So the wave can propagate up to 3 m at  $f = 1$  GHz. The depth limit for 200 MHz is 11.5 m. This means that the wave can propagate an addition of 11.5 m after the depth of 100 m. So the wave can propagate up to 12.5 m at  $f = 200$  MHz. The wave at lower frequencies has higher propagation limits because there is less attenuation in lower frequencies.

The depth limits are obtained for martian soil before. The same analysis is performed for wet soil to make a comparison. Wet soil analysis is performed using depth versus attenuation graphs and the martian soil results. The depth versus attenuation graphs are shown in Figure 6.41 and Figure 6.42.

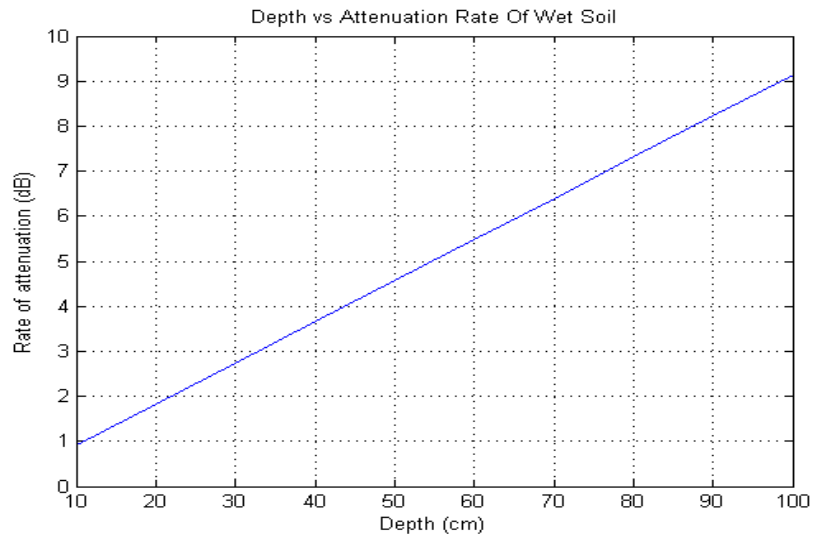


Figure 6.41: The graph shows depth versus attenuation of wet soil at  $f = 200$  MHz

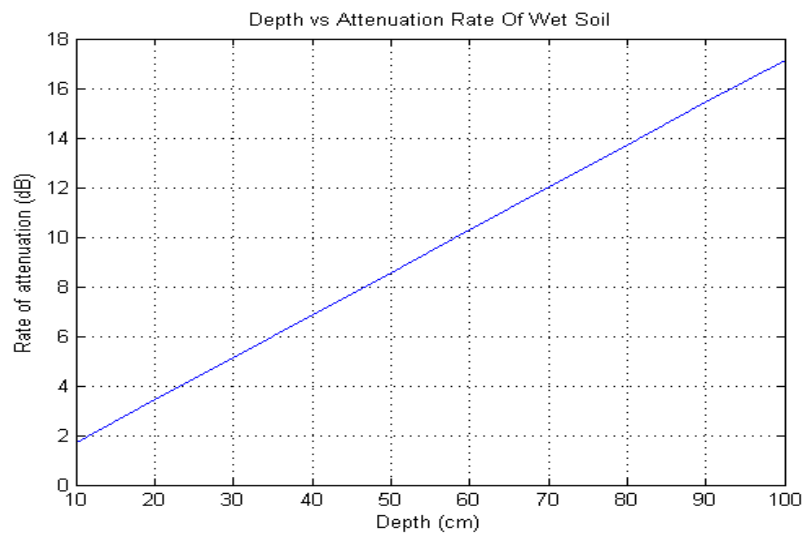


Figure 6.42: The graph shows depth versus attenuation of wet soil at  $f = 1$  GHz

Martian soil has 15 dB of attenuation for 1 m at  $f = 1$  GHz. Wet soil has an addition of 17 dB attenuation for 1 m which is equal to 32 dB. The depth limit for 1 GHz is 0.98 m. This means that the wave can propagate an addition of 1 m after the depth of 100 m. So the wave can propagate up to 2 m at  $f = 1$  GHz. Martian soil has 2 dB of attenuation for 1 m at  $f = 200$  MHz. Wet soil has an addition of 9 dB attenuation for 1 m which is equal to 11dB. The depth limit for 200 MHz is 2.09 m. This means that the wave can propagate an addition of 2 m after the depth of 100 m. So the wave can propagate up to 3 m at  $f = 200$  MHz.

When the depth limits are compared, it is observed that wet soil has lower depth limit. The reason of this is there is more attenuation in wet soil than martian soil that is used in the study.

When compared to other systems, OFSIS has little noise. It is also observed from the noise analysis that OFSIS has a good performance that works properly in all of the frequency and depth ranges that are used in the study.

## CHAPTER 7

### CONCLUSIONS AND FUTURE WORK

In this thesis, the position and the depth of the buried perfectly conducting circular cylinder are determined using a GPR system. This system comprises of a transmitter, a buried object and an OFSIS. The transmitter is placed 100 m above from the interface. The radius of the buried circular cylinder is  $a$  and the depth of the cylinder from the dielectric interface is  $b$ .

A sample of martian soil is used during the study. Martian soil is very dry. The Debye model is used to determine the permittivity value of martian soil. This model shows the relationship between dielectric constant (relative permittivity) of soils and water content of soils. The medium has a dielectric behaviour that is explained by Debye model.

The attenuation is very little due to the Debye model of martian soil that is used in the study. The attenuation of martian soil and wet soil are compared. It is observed that wet soil has much more attenuation than martian soil. Wet soil has 0.5 dB of attenuation at 100 MHz but martian soil has 0.5 dB of attenuation at 1 GHz.

In order to determine the position and the depth of the target, first of all the electric field distribution coming through OFS is determined mathematically by integrating the Green's function over the induced current distribution. Then the electric field distribution is observed by writing the MATLAB code of the mathematical expression. Various distributions are obtained. They are analyzed by changing the

frequency of the system and the depth of the cylinder. When the depth is increased at a fixed frequency, the wave pattern's shape is changed from spherical to parabolic to plane wave like appearance. As a result of this, it is observed that it is harder to make sensitive measurements.

When the frequency is changed at a fixed depth, trade off is observed. Higher frequencies are needed for nearer objects because there is more coupling and better resolution. Lower frequencies are needed for further objects because there is less attenuation.

After obtaining the distribution, the voltages inside the distribution are measured by OFS. The obtained voltages and x axis displacement values together are related to the interference fringe patterns. The interference fringe patterns are obtained from the 2D plots of x axis displacement versus measured voltages. Different interference fringe patterns are observed for various depth and frequency values.

The important thing about this study is that various algorithms are developed from the interference fringe patterns in order to detect the position and the depth of the cylinder. Those algorithms are as follows. In order to detect the position of the cylinder, the symmetry of the patterns is used. It is observed that the interference fringe patterns are symmetric around the origin. This is where the cylinder is buried.

In order to detect the depth of the cylinder; relative amplitude, x displacement and depth relationship of the interference fringe patterns are used. It is seen that when the depth is increased, the relative amplitudes of the side interference fringe patterns also increased. Since the relative amplitudes are related to object's depth, the depth is determined using FWHMX. The relative amplitude values are recorded for each of the x displacement values. Then the 2D plots of x displacement versus relative amplitude values are obtained. FWHMX is measured from those 2D plots. Using the measured FWHMX values, 2D plots of depth versus FWHMX are obtained.

After obtaining the 2D plots, basic linear fitting is performed in MATLAB. The equations for those plots are obtained. Then the equations and the frequency are combined to form a new equation. This equation helps to determine the depth by knowing the frequency and FWHMX values. Using the recorded values, 3D plot of frequency versus depth versus FWHMX are obtained. The equation related to this plot is also determined.

MATLAB program is used to perform all the works that are explained. The noise of the OFSIS is extracted using OPTIWAVE program. They mostly arose from OFSIS elements which are the modulator and the photodetector. The system is constructed in OPTIWAVE program and noise of the system is extracted. Noise is observed from photodetection with filtering and distortion exists due to modulator. After extracting the noises due to the modulator and the photodetector, they are added to the measured voltages. It is observed that OFSIS works properly in all of the frequency and depth ranges that are used. As a result of this, the operating frequencies of the system are observed. The frequency range that is used in the study is between 100 MHz to 1 GHz. The depth range that is used in the study is between 10 cm to 100 cm.

The receiver sensitivity values are determined for each frequency. It is the lowest power that the receiver can achieve in order to realize the incoming signals. The receiver sensitivity is obtained about -77 dBm for 1 GHz and it is obtained about -87 dBm for 100 MHz. Employing a photonic sensor instead of a standard RF receiver offers the advantage of preventing interference between the cable connection and other systems or nearby operating sources, and photonic systems have much lower amplification noise –typically ~1dB- compared to easily available radio frequency amplifiers.

It is known that noise affects transmitter's minimum power which needs to be greater than a limit. The limit that is used in the study is 3 dB above the noise. Depth limits for fixed frequency values are determined. In order to obtain the depth limit at a fixed frequency, first of all the SNR values are obtained. Then using the depth and

SNR value relationships, the distances that the wave propagates inside the soil are calculated. It is observed that the wave can propagate up to 12.5 m at 200 MHz and 3 m at 1 GHz. So the wave can propagate fairly up to certain distances inside the martian soil. Higher propagation limits are observed at lower frequencies because there is less attenuation.

The depth limits are also analyzed for wet soil. It is observed that the wave can propagate up to 3 m at 200 MHz and 2 m at 1 GHz. Wet soil has lower depth limits than martian soil because there exists more attenuation. Hence thanks to the relationship between the FWHMX and depth, a 2D knowledge of the buried object can be obtained for burial depths until 12.5 meters in dry and 3 meters in wet soils. This is similar to obtaining a 2D image of the below surface, which is the main purpose of the recently developed SAR-GPR techniques. In those techniques, moving transmitters and receivers create synthetic or virtual multiple transmitting and receiving aperture points, greatly increasing the measurement scope. SAR technique increases image resolution of GPR images and prevents undesired effects.

This study may be developed further in four other dimensions:

- 1) System operation will be tested experimentally, in a laboratory sandbox study, using an optical communication link, an antenna attached Mach-Zehnder electro-optic modulator, a 1 Watt transmitter located above the setup. The photodetector output will be observed on an RF spectrum analyzer. It is hoped that the experiment will prove the viability of this proposed system.
- 2) In simulation scenarios, the effect of the scattering object radius was not mentioned. Effect of radius size on the observed OFS output will be analyzed through further computer simulations. It is believed that this radius variation will add another dimension to the FWHMX versus depth and operation frequency relationship.

3) Also it is planned to check the effect of having dielectric objects instead of perfectly conducting metal ones in simulation studies and later in experiments. This is expected to reduce the scattering effect and make it harder to locate the object.

4) The system configuration may be developed further; instead of a single far away source that produces planar wave at the surface level, a SAR system like close moving transmitter may be introduced to the system for the purpose of increasing the received information.

In conclusion to all of this, the purpose of the study is achieved with the methods that are explained. The buried circular cylindrical objects depth and position are shown to be determined from the interference fringe pattern analyses.

## REFERENCES

- [1] D. J. Daniels, *Ground Penetrating Radar*, 2<sup>nd</sup> ed. United Kingdom: The Institution of Electrical Engineers, 2004.
- [2] G. S. Baker, H. M. Jol, *Stratigraphic Analyses Using GPR*. USA: The Geological Society of America (GSA), 2007.
- [3] J. M. Lopez-Higuera, *Handbook of Optical Fibre Sensing Technology*. London: John Wiley & Sons, 2002.
- [4] G. C. Righini, A. Tajani, A. Cutolo, *An Introduction to Optoelectronic Sensors*. Singapore: World Scientific Publishing, 2009.
- [5] S. Ebihara, M. Sato, "Application of an Optical Electric Field Sensor Array for Direction of Arrival Estimation in a Borehole", *Proc. of Geoscience and Remote Sensing Symposium (IGARSS'01)*, vol. 3, pp. 1530-1532, July 2001.
- [6] W. C. Gibson, *The Method of Moments in Electromagnetics*. USA: Chapman & Hall / CRC Taylor & Francis, 2008.
- [7] M. Sato, "A New Bistatic GPR System Using a Passive Optical Sensor for Land Mine Detection", *Proc. of 2<sup>nd</sup> International Workshop on Advanced Ground Penetrating Radar*, pp. 164-167, May 2003.
- [8] R. Tanaka, M. Sato, "A GPR System Using a Broadband Passive Optical Sensor for Land Mine Detection", *Proc. of 10<sup>th</sup> International Conference on GPR*, vol. 1, pp. 171-174, June 2004.

- [9] S. J. Cho, R. Tanaka, M. Sato, "Bistatic GPR By Using an Optical Electric Field Sensor", *Proc. of Geoscience and Remote Sensing Symposium (IGARSS'05)*, vol. 1, pp. 348-351, July 2005.
- [10] M. Sato, K. Yoshida, "Bistatic UWB Radar System", *Proc. of International Conference on Ultra-Wideband (ICUWB 2007)*, pp. 62-65, September 2007.
- [11] N. Hayashi, M. Sato, "A Fundamental Study of Bistatic UWB Radar for Detection of Buried Objects", *Proc. of International Conference on Ultra-Wideband (ICUWB 2008)*, vol. 2, pp. 125-128, September 2008.
- [12] T. Takayama, M. Sato, "Evaluation of an Array Type Directional Borehole Radar System", *Proc. of Geoscience and Remote Sensing Symposium (IGARSS'05)*, vol. 1, pp. 352-355, July 2005.
- [13] T. Takayama, M. Sato, "A Novel Direction-Finding Algorithm for Directional Borehole Radar", *IEEE Trans. on Geoscience and Remote Sensing*, vol. 45, pp. 2520-2528, August 2007.
- [14] T. Takayama, J. H. Kim, M. Sato, "Analysis of Directional Borehole Radar Measurement Data", *Proc. of 4<sup>th</sup> International Workshop on Advanced Ground Penetrating Radar*, pp. 32-35, June 2007.
- [15] M. Sato, T. Takayama, "A Novel Directional Borehole Radar System Using Optical Electric Field Sensors", *IEEE Trans. on Geoscience and Remote Sensing*, vol. 45, pp. 2529-2535, August 2007.
- [16] M. Sato, T. Takayama, "High Range Resolution Directional Borehole Radar for 3D Fracture Delineation", *Proc. of Geoscience and Remote Sensing Symposium (IGARSS'09)*, pp. I-132-I-135, July 2009.

- [17] H. M. Jol, *Ground Penetrating Radar Theory and Applications*. United Kingdom: Elsevier Science, 2009.
- [18] J. J. Daniels, “Ground Penetrating Radar Fundamentals”, *Appendix of U. S. EPA Region V Report*, pp. 1-21, November 2000.
- [19] D. J. Daniels, “Surface-penetrating Radar”, *Electronics & Communication Engineering Journal*, pp. 165-182, August 1996.
- [20] M. Sato, “GPR and Its Application to Environmental Study”, *Mongolian Technical University Seminar Paper*, pp. 1-17, January 2001.
- [21] G. R. Olhoeft, “Electrical, Magnetic and Geometric Properties that Determine Ground Penetrating Radar Performance”, *Proc. of 7<sup>th</sup> International Conference on GPR*, pp. 177-182, May 1998.
- [22] D. K. Cheng, *Field and Wave Electromagnetics*, 2<sup>nd</sup> ed. USA: Addison-Wesley, 1989.
- [23] S. Cardimona, “Subsurface Investigation Using Ground Penetrating Radar”, *Proc. of 2<sup>nd</sup> Annual Conference on the Application of Geophysical and NDT Methodologies to Transportation Facilities and Infrastructure (GEOPHYSICS 2002)*, pp. 1-15, July 2002.
- [24] “Ground Penetrating Radars. Principles, Applications and Design”, <http://www.eltesta.com/resources/application-notes/index.htm>, Last visited on 15.08.2011.
- [25] J. G. Proakis, M. Salehi, *Communication Systems Engineering*, 2<sup>nd</sup> ed. USA: Prentice-Hall, 2002.

- [26] R. M. Morey, *Ground Penetrating Radar for Evaluating Subsurface Conditions for Transportation Facilities*. Washington: National Academy, 1998.
- [27] D. Kinnon, "Land Mine Identification Using Microwave Resonance Signatures", *Ms Thesis*, University of Queensland, October 1999.
- [28] M. I. Skolnik, *Introduction to Radar Systems*, 3<sup>rd</sup> ed. Singapore: McGraw-Hill, 2001.
- [29] Q. A. Naqvi, A. A. Rizvi, Z. Yaqoob, "Scattering of Electromagnetic Waves from a Deeply Buried Circular Cylinder", *Progress in Electromagnetics Research (PIER 27)*, vol. 27, pp. 37-59, 2000.
- [30] P. Ripka, A. Tipek, *Modern Sensors Handbook*. Great Britain: ISTE, 2007.
- [31] "Photonics, Fiber Optic Sensors and Their Application in Smart Structures", <http://www.ntu.edu.sg/mpe/Research/programmes/Sensors/sensors/fos/fosass/photonics.HTML>, Last visited on 15.07.2011.
- [32] A. Grillet, "Optical Fibre Sensors: Principles and State of Art", *OFSETH D1.2-Specification Report on Optical Sensors*, pp. 1-45, 2006.
- [33] G. Keiser, *Optical Fiber Communications*, 2<sup>nd</sup> ed. New York: McGraw-Hill, 1991.
- [34] M. Cvijetic, *Optical Transmission Systems Engineering*. USA: Artech House, 2004.
- [35] R. Horak, *Telecommunications and Data Communications Handbook*. Canada: John Wiley & Sons, 2007.

- [36] J. Zheng, *Optical Frequency-Modulated Continuous Wave (FMCW) Interferometry*. USA: Springer Science & Business Media, 2005.
- [37] A. Ghatak, K. Thyagarajan, *Introduction to Fiber Optics*. London: Cambridge University, 1998.
- [38] P. Neveux, A. Chambarel, “Debye Modelisation for the Soil Moisture Measurement in TDR”, *Instrumentation and Measurement Technology Conference (IMTC 2006)*, pp. 187-190, April 2006.
- [39] C. Leuschen, “Analysis of the Complex Permittivity and Permeability of a Martian Soil Simulant from 10 MHz to 1 GHz”, *Proc. of Geoscience and Remote Sensing Symposium (IGARSS'99)*, vol. 4, pp. 2264-2266, July 1999.
- [40] M. S. Nakano, P. Savi, “Dielectric Permittivity Estimation via TDR Measurements”, *International Conference on Electromagnetics in Advanced Applications (ICEAA'09)*, pp. 921-924, September 2009.
- [41] S. J. Orfanidis, “Electromagnetic Waves and Antennas”, <http://www.ece.rutgers.edu/~orfanidi/ewa/>, Last visited on 25.09.2011.
- [42] “Resource Lesson, Physical Optics-Interference and Diffraction Patterns”, [http://dev.physicslab.org/Document.aspx?doctype=3&filename=PhysicalOptics\\_InterferenceDiffraction.xml](http://dev.physicslab.org/Document.aspx?doctype=3&filename=PhysicalOptics_InterferenceDiffraction.xml), Last visited on 25.08.2011.
- [43] G. P. Agrawal, *Fiber-Optic Communication Systems*, 3<sup>rd</sup> ed. New York: John Wiley & Sons, 2002.
- [44] F. T. S. Yu, S. Jutamulia, S. Yin, *Introduction to Information Optics*. USA: Academic Press, 2001.

## APPENDIX A

### MATLAB CODE

```
% plot in x and z
clear;
c=2.98e8; % speed of light
f=1e9; % frequency
E0=8.854e-12; % vacuum permittivity
lamda=c/f;
kone=2.*pi./lamda;
permione=1; % air
G=1.64;

% soil permittivity models and parameters of debye pellet
permi_inf=3.12;
permi_stat=3.57;
tau_relax=0.041e-9;
permitwo=permi_inf + (permi_stat - permi_inf)/(1+ 1i*2*pi*f*tau_relax);
n=real(sqrt(permitwo))+1i*abs(imag(sqrt(permitwo))); % index of refraction
ktwo=kone.*(n);
conductivity=real(n)*imag(n)*2*2*pi*f*E0;
a=5e-2; % cylinder radius
b=10e-2; % distance from surface to the cylinder center (depth)
m=-40:40; % summation window, instead of -inf to +inf
indexx=1;
xstart=-5;
```

```

xstop=5;
numbits=10; % measurement step resolution
axis_resolution=(-xstart+xstop)/(2^numbits); % measurement resolution for axes
zstart=0.1;
zstop=1;
xaxis=xstart:axis_resolution:xstop;
zaxis=zstart:axis_resolution:zstop;
scattered=zeros(length(xaxis),length(zaxis));
surface_ref=zeros(length(xaxis),length(zaxis));
position=zeros(length(xaxis),length(zaxis));

for xxaxis=xstart:axis_resolution:xstop; % +1m to -1m measurement range in x axis
    indexz=1;
    for zzaxis=zstart:axis_resolution:zstop; % upto from surface
        fi=atan(abs((zzaxis+b)/xxaxis));
        rho=(xxaxis^2+(zzaxis+b)^2)^0.5;
        scattered(indexx,indexz)=-8*kone^2/sqrt(2*pi)/(kone^2-
ktwo^2)/(kone+ktwo)*exp(1i*ktwo*b-1i*kone*b*sin(fi)+1i*b*sqrt(ktwo^2-
kone^2*(cos(fi))^2))*(kone*(sin(fi))^2-sin(fi)*sqrt(ktwo^2-sin(fi)*sqrt(ktwo^2-
kone^2*(cos(fi))^2))*exp(1i*kone*rho-
1i*pi/4/sqrt(kone*rho)*sum(1i.^m./besselh(m,(ktwo*a)).*besselj(m,(ktwo*a)).*exp(
1i*m*atan((ktwo/kone/cos(fi))^2-1)));
        surface_ref(indexx,indexz)=(real(n)-1)/(real(n)+1)*exp(-1i.*kone.*(zzaxis));
        position(indexx,indexz) = [xxaxis+1i*zzaxis];
        indexz=indexz+1;
    end
    indexx=indexx+1;
end
etotal=scattered+surface_ref; % total e field
figure;
subplot(3,1,1);surf(xaxis,zaxis,10*log10(abs(scattered)));
subplot(3,1,2);surf(xaxis,zaxis,10*log10(abs(etotal)));

```

```

% sensor part
p_length=axis_resolution*round(0.05/axis_resolution); % 5 cm probe length
AntenaDistance=100; % transmitting meter above
AntenaPower=100; % watt transmitting antenna power

Estrength=9.48/AntenaDistance*sqrt(AntenaPower); % relation between voltage to
the antenna and produced e field

etotal=Estrength*etotal; % e field amplitude adjusted wrt to the transmitter power
and distance
Res_Rx= 20 * pi^2* (p_length/lamda)^2; % receiver antenna series resistance
RxAF=9.73* /(lamda*sqrt(G)); % receiver antenna factor, 3dB antenna
RxResp = RxAF.*(50 ./ (50+Res_Rx) )^2; % 50 ohm impedance on EO sensor
assumed

h_count =0;
Vread=zeros(round((zstop-zstart)/0.1+1),length(etotal));
meas_end=round((2^numbits+1 -round(p_length/axis_resolution)));
for probe_height = zstart:0.1:zstop
    h_count =h_count +1;
    kx=1;

for xx=xstart:axis_resolution:xstop-p_length;

% probe voltage
p_angle=0/180*pi; % orientation angle, 0, 45, or 90 degrees
p_start=[xx;probe_height]; % probe starting point in x and z axis
p_finish=p_start+axis_resolution*round([p_length*cos(p_angle);p_length*sin(p_ang
le)]/axis_resolution);
indexp=1;
probe_pointsx=zeros(1,(p_length/axis_resolution));
probe_pointsz= zeros(1,(p_length/axis_resolution));

```

```

Eseen=0;
for kkk=0:(p_length/axis_resolution);
    pointx=p_start(1)+axis_resolution*round(kkk*cos(p_angle));
    pointz=p_start(2)+axis_resolution*round(kkk*sin(p_angle));
    probe_pointsx(indexp)=round((pointx-xstart)/axis_resolution)+1;
    probe_pointsz(indexp)=round((pointz-zstart)/axis_resolution)+1;
    Eseen=Eseen+etotal(probe_pointsx(indexp),probe_pointsz(indexp));
    indexp=indexp+1;
end

Eseen=abs((Eseen)/(indexp-1))/2; % for unitary e field, 1V/m.
Vseen=Eseen*RxResp;

Vread(h_count,kx)=Vseen;

kx=kx+1;
end
end

for heg = 1:10
for kx=meas_end+1:(2^numbits+1)
    Vread(heg,kx)= Vread(heg,meas_end)
end
end

for kount=1:length(etotal)

vr10cmm(kount)=((abs(Vread(1,kount))));
end

figure;
plot(xaxis,vr10cmm);

```

```

% amplitude part
vstart = Vread(1,2);
ampstart=0;
slope=sign(Vread(1,2)-Vread(1,1));
kk=1;
for kount=3:((length(etotal)-1)/2)
    if slope ==1
        if Vread(1,kount)> Vread(1,kount-1)

            slope=1;
        else
            slope = -1;
            if abs(vstart-Vread(1,kount-1))> ampstart
                amplitude(2,kk)= abs(vstart-Vread(1,kount-1));
                amplitude(1,kk)=(((length(etotal)-1)/2)-kount+1)/((length(etotal)-
1)/2)*xstop;
                ampstart = amplitude(2,kk)
                kk=kk+1;
                vstart=Vread(1,kount-1);

            end
        end
    else
        if Vread(1,kount)< Vread(1,kount-1)
            slope=-1;
        else
            if abs(vstart-Vread(1,kount-1))> ampstart
                slope = +1;
                amplitude(2,kk)= abs(vstart-Vread(1,kount-1));
                amplitude(1,kk)=(((length(etotal)-1)/2)-kount+1)/((length(etotal)-
1)/2)*xstop;
                ampstart = amplitude(2,kk)
            end
        end
    end
end

```

```
    kk=kk+1;
    vstart=Vread(1,kount-1);

    end

    end

    end
    amplitude(2,:)=amplitude(2,)/max(amplitude(2,));
    figure;
    plot(amplitude(1,:),amplitude(2,));
```

# APPENDIX B

## OPTIWAVE SCREEN CAPTURE

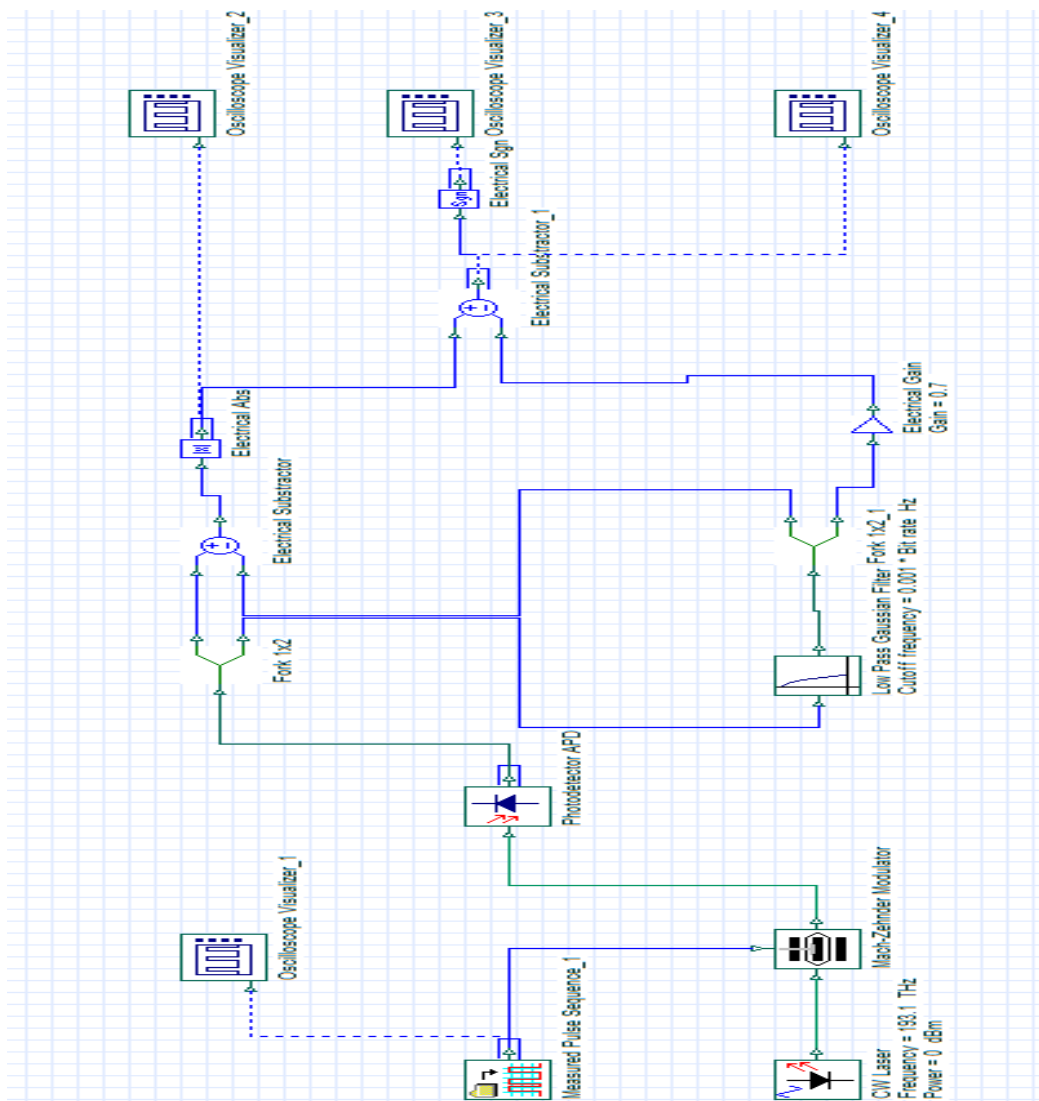


Figure A.1: The screen capture of the system in OPTIWAVE

